

Universität
Rostock



Traditio et Innovatio

Combining Experimental and Theoretical Approaches to Investigate Structure and Dynamics in Soft Condensed Matter

Cumulative Dissertation

to obtain the academic degree
doctor rerum naturalium (Dr. rer. nat.)
of the Faculty of Mathematics and Natural Sciences
at the University of Rostock

Submitted by

M.Sc. Joel Diaz Maier
born on June 20, 1996 in Pforzheim

Rostock, April 2024

Referees:

Prof. Dr. Joachim Wagner, Institut für Chemie, Universität Rostock

Prof. Dr. Christian Gutt, Institut für Physik, Universität Siegen

Prof. Dr. Hartmut Löwen, Institut für Theoretische Physik II – Soft Matter,
Heinrich-Heine-Universität Düsseldorf

Date of submission: April 12, 2024

Date of scientific colloquium: October 15, 2024

The research presented in this work was conducted from November 2020 to April 2024 at the Chair of Physical Chemistry in the Department of Chemistry at the University of Rostock, under the supervision of Prof. Dr. Joachim Wagner.

Table of Contents

Declaration of Authorship	v
Acknowledgments	vii
Abstract	ix
Publications for the Cumulative Dissertation	xi
Abbreviations	xiii
1 Introduction	1
1.1 Motivation and Aim	1
1.2 Fundamentals of the Employed Methods	3
1.2.1 Rheology	3
1.2.2 Scattering Methods	4
1.2.3 Photon Correlation Spectroscopy	8
1.2.4 Mode-Coupling Theory	10
2 Research Overview	13
2.1 Characterization of a Novel Model Hard-Sphere System	13
2.1.1 Preparation of Poly(dimethylsiloxane)-Stabilized Poly(methyl methacrylate) Particles	13
2.1.2 Particle Morphology	15
2.1.3 Measurable Structure Factors of Optically Inhomogeneous Particles	18
2.1.4 Collective Short-Time Diffusion	25
2.2 Mode-Coupling Theory for the Quantitative Analysis of Experiments	28
2.2.1 Collective Dynamics and Transport Properties of Model Hard-Sphere Suspensions	28
2.2.2 Schematic Mode-Coupling Model for the Characterization of Viscoelastic Properties of Poly(<i>N</i> -isopropylacrylamide) Hydrogels	33
3 Perspective	39
References	41
Publication I	49
Publication II	65
Publication III	79
Publication IV	93

Declaration of Authorship

I hereby declare under oath that I have completed the work submitted here independently and have composed it without outside assistance. Furthermore, I have not used anything other than the resources and sources stated. Where I have taken sections from these works in terms of content or text, I have identified this appropriately.

Joel Diaz Maier
Rostock, April 10, 2024

Acknowledgments

I would like to express my gratitude to Prof. Joachim Wagner for giving me the opportunity to conduct research on fascinating topics within his group. I am grateful for the many years of guidance and support that he has provided me with, while also encouraging me to work independently and develop my own ideas.

I am grateful to Prof. Hartmut Löwen and Prof. Christian Gutt for undertaking the review of my thesis. I would also like to thank Hartmut Löwen in particular for attending my oral defense in person.

A huge thank you to the entire Wagner team for making my time there so amazing. Thanks to Markus Kulossa and his keen eye for details, Daniel Weidig and his quick wit, Alexandra Bumann for always checking in on me and Paul Tümmeler for sharing so much knowledge, even though we could never realize our joint project. I also want to express my appreciation to Dr. Philipp Marienhagen for a great time while sharing an office and for always showing genuine interest in my work.

I want to express my deepest thanks to Katharina Gaus. Working and collaborating with you has been the highlight of my PhD experience. I sincerely hope that I was able to offer you something, and I want you to know that I learned so much from you as well. Not a single second spent with you was wasted time.

I am grateful to the whole physical chemistry department for creating such a great atmosphere and for fostering a sense of community. Special thanks to all the technical staff for keeping this place running smoothly. I especially want to thank Nele Leopold for all the help in the laboratory and Sabine Kindermann for help with administrative matters.

I would also like to thank the department for giving me the opportunity to teach and share my knowledge. To all the students I had the luck to meet along the way, I hope I could teach you one or two useful skills, and if not, at least you had a fun time with me.

Thank you to Eric Schneider, Iva Rosewig, Ole Tiemann and family, and to all my other friends for always cheering me on and for the many nights of sharing both our suffering and our success.

At last, I want to thank my mother for her endless support and for always believing in me.

Abstract

This work demonstrates the development of advanced quantitative techniques for the analysis of rheology and scattering experiments on correlated colloidal many-particle systems. The microscopic structure and dynamics of a novel hard-sphere model system consisting of poly(dimethylsiloxane)-stabilized poly(methyl methacrylate) particles is characterized by means of static and dynamic light scattering experiments. Topologically, the particles can be described by a core-shell model for the refractive-index distribution which takes into account an inhomogeneous swelling of the the polymer core caused by the penetration of suspension medium molecules into the entangled network. The self-organization of the particles at high volume fractions is analyzed by modeling the scattered intensity of dense, refractive-index-matched suspensions with a model based on a multi-component hard-sphere Percus-Yevick ansatz which explicitly takes the particle size distribution into account. From the quantitative match between experimental observations and hard-sphere theory, the hard sphere character of the investigated dispersions is confirmed. Furthermore, it is shown that measurable structure factors obtained from scattering experiments are decisively influenced by the detailed optical properties of the scatterers in systems with a size distribution. The collective short-time diffusion of suspensions containing PMMA-PDMS particles are besides the potential inter-particle interactions also influenced by hydrodynamic interactions mediated by the surrounding medium, which in these systems can be described quantitatively using an effective one-component approach involving the $\delta\gamma$ -expansion. The full collective dynamics of the suspensions is modeled quantitatively employing an empirically modified multi-component mode-coupling scheme which uses a rescaled-structure-factor approach. The volume-fraction-dependence of both the zero-shear viscosity and the average long-time self-diffusion coefficient as transport quantities are predicted quantitatively by the mode-coupling scheme. Mode-coupling theory is also used to model the viscoelastic response of a hydrogel consisting of network-forming poly(*N*-isopropylacrylamide) particles with an extended, schematic $F_{12}^{(\dot{\gamma})}$ -model, which enables linking a decrease in elasticity with an enhanced mobility of particles in nearest-neighbor cages.

Publications for the Cumulative Dissertation

This cumulative dissertation summarizes the content of the following publications:

Publication I

Viscoelastic properties of pNIPAM-hydrogels: A mode-coupling theory study¹

J. Diaz Maier and J. Wagner

J. Chem. Phys. **157**, 114901 (2022)

<https://doi.org/10.1063/5.0097841>

Publication II

Structure and short-time diffusion of concentrated suspensions consisting of silicone-stabilised PMMA particles: a quantitative analysis taking polydispersity effects into account²

J. Diaz Maier and J. Wagner

Soft Matter **20**, 1309–1319 (2024)

<https://doi.org/10.1039/D3SM01510F>

Publication III

Measurable structure factors of dense dispersions containing polydisperse, optically inhomogeneous particles³

J. Diaz Maier, K. Gaus and J. Wagner

J. Appl. Crystallogr. **57**, 1503–1513 (2024)

<https://doi.org/10.1107/S1600576724007957>

Publication IV

Rescaled mode-coupling scheme for the quantitative description of experimentally observed colloid dynamics⁴

J. Diaz Maier and J. Wagner

Phys. Rev. E **109**, 064605 (2024)

<https://doi.org/10.1103/PhysRevE.109.064605>

Abbreviations

ACF	auto-correlation function
DLS	dynamic light scattering
DDM	dynamic differential microscopy
HI	hydrodynamic interaction
ICF	intensity correlation function
ISF	intermediate scattering function
LCST	lower critical solution temperature
MCT	mode-coupling theory
PCS	photon correlation spectroscopy
RDF	radial distribution function
SANS	small-angle neutron scattering
SLD	scattering length density
SLS	static light scattering

Substances

AIBN	azobisisobutyronitrile
GA	glutaraldehyde
MMA	methyl methacrylate
PDMS	poly(dimethylsiloxane)
PDMS-MA	monomethacryloxypropyl-terminated poly(dimethylsiloxane)
PHSA	poly(12-hydroxystearic acid)
PMMA	poly(methyl methacrylate)
pNIPAM	poly(<i>N</i> -isopropylacrylamide)
pNIPAM- <i>c</i> -GA	poly(<i>N</i> -isopropylacrylamide) cross-linked with glutaraldehyde

1 Introduction

1.1 Motivation and Aim

Soft condensed matter science investigates materials such as colloids, gels, polymers, liquid crystals, foams, and biological tissues.⁵ These systems are composed of basic structural units formed through molecular self-organization. With relevant length scales being on the order of nanometers to micrometers, these units are significantly larger than individual atoms.⁶ Due to the interaction energy between building blocks being on the order of the thermal energy, soft materials are strongly affected by thermal fluctuations and can be easily deformed by external forces. On mesoscopic length scales, these systems display slow dynamics with much larger relaxation times compared to molecular liquids.⁷

A persistent goal in soft matter physics is to provide microscopic explanations for macroscopic phenomena with the obvious aim, besides a fundamental understanding of matter, enabling the targeted design of new materials with desired properties.⁸ This bottom-up approach involves developing rational design strategies to create mesoscopic building blocks from specifically architected molecules,^{9,10} being able to precisely tune interaction potentials between particles to realize desired structures,¹¹ gaining a quantitative understanding of the relationship between structure and microscopic dynamics,^{12,13} and, finally, relating all these properties to macroscopically observable features.¹⁴ This requires an interdisciplinary effort with the combination of experiments, theory, and computer simulations.

Colloidal suspensions, consisting of dispersed particles with very precisely tuneable inter-particle interactions, serve as academically highly relevant model systems for complex fluids.¹⁵ By combining suitable surface functionalities and volume properties, it is possible to replicate a wide range of fundamental interactions such as hard-core repulsive,¹⁶ soft short-range attractive,^{17,18} long-range repulsive electrostatic¹⁹ or dipolar^{20,21} forces. More advanced functionalizations may introduce direction-dependent features such as those found in shape-anisotropic,²²⁻²⁵ self-propelled,²⁶⁻²⁸ or Janus particles.²⁹⁻³¹ Colloidal dispersions enable the experimental study of fundamental phenomena in soft matter systems in a very isolated and controlled environment. These features also make colloidal systems comparatively easy to describe theoretically.

In addition to microscopy,³²⁻³⁷ scattering techniques are frequently used to study colloidal many-particle systems.³⁸ Methods such as laser light scattering, which can be realized in a laboratory setup,³⁹ or small-angle scattering (SAS) experiments⁴⁰ using neutrons or X-rays at large scale research facilities, provide access to the averaged structure of a large ensemble of particles. Dynamical properties can be investigated by analyzing ensemble-averaged time-correlation functions obtained,

for example, from dynamic light scattering (DLS)^{41,42} or X-ray photon correlation spectroscopy.⁴³

While the quantitative analysis of scattering experiments on simple colloidal systems is generally considered textbook knowledge,⁴⁴ many standard approaches rely heavily on restrictive assumptions about the systems under investigation. Conventional particle sizing with DLS expects assemblies of non-interacting Rayleigh scatterers, but can become unreliable for interacting systems and for large particles where detailed optical properties cannot be ignored.⁴⁵ Comprehensive form factor analysis from SAS data is typically limited to dilute, non-interacting suspensions, especially if systems display a size distribution.^{46,47} Quantitative structure analysis of correlated ensembles is seldom conducted for polydisperse systems, and even for uniform suspensions, such approaches are limited to the simplest interaction potentials and particle shapes.^{48,49}

From a theoretical perspective, establishing a quantitative link between structure and dynamics in correlated many-body systems is equally challenging. Theoretical methods such as Ornstein-Zernike integral equation theory,⁵⁰ classical density functional theory,^{51,52} mode-coupling theory,^{12,53,54} or the self-consistent, generalized Langevin equation framework⁵⁵⁻⁵⁷ amount to an extensive body of work but can still not be regarded as standard techniques used by a wide range of practitioners like, for example, computer simulations or quantum chemical methods.

The aim of this work is to demonstrate methods for the advanced quantitative analysis of structure-dynamics relations in correlated colloidal many-particle systems, with a focus on the evaluation of scattering experiments taking into account both size-dispersity effects and the inhomogeneous scattering capacities of particles. Hard-sphere suspensions are the model system of choice because they are theoretically well understood and exhibit comparatively low complexity.

Chronologically, the starting point of this work is a study in which the rheological response of a comparatively complex-to-describe, gel-forming particle network is investigated by means of schematic mode coupling theory, outlined in **Publication I**. Realizing the overwhelming complexity of this system, it became apparent that the goal of investigating general quantitative relationships between structure and rheology in complex soft materials is best targeted by systematically starting from simpler systems. Thus, **Publication II** deals with the validation of a novel hard-sphere system, which is gaining popularity due to its ease of preparation compared to well-established hard-sphere particles. **Publication III** demonstrates the impact of size-dispersity on the evaluation of measurable structure factors extracted from static scattering experiments for optically inhomogeneous particles, which is integral for understanding the scattering behavior of the here investigated experimental systems. Finally, **Publication IV** is a first attempt to use mode-coupling theory as a quantitative tool to describe the experimentally obtained collective dynamics of polydisperse hard-sphere systems. It is shown that this is feasible with knowledge of the detailed particle topology, accurate treatment

of size-dispersity, incorporation of hydrodynamic interactions, and slight modifications of the memory kernel of an established multi-component mode-coupling scheme.

1.2 Fundamentals of the Employed Methods

1.2.1 Rheology

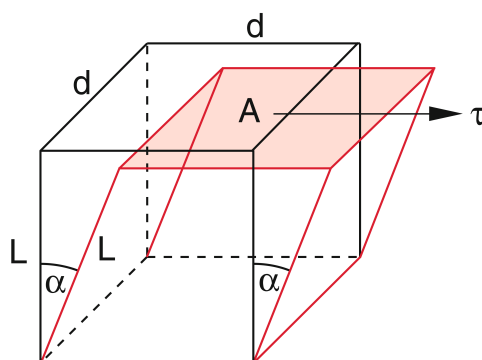


Figure 1.1: Schematic representation of a shear process, where an applied shear stress τ causes a body to tilt by the angle α . (Reproduced from Demtröder⁵⁸ with permission from Springer Nature.)

Rheological methods allow the characterization of the mechanical properties of materials using rotational or oscillatory shear experiments.⁵⁹ Shearing is the deformation of a body by a force acting tangentially on its surface.^{58,60} This is illustrated in Fig. 1.1 for an elastic cuboid. Due to the applied shear stress τ , which is defined as the shear force normalized to the surface area, the body is tilted by an angle α in the stress direction. For ideal elastic materials the stress magnitude $\tau = |\boldsymbol{\tau}|$ is connected to the strain $\gamma = \tan \alpha$ simply by Hooke’s law, $\tau = G\gamma$. The shear modulus G is equivalent to a force constant for shear processes.

Fig. 1.1 can equally represent shearing a viscous fluid enclosed between two parallel, thin plates, where the upper plate moves in the direction of the applied stress while the lower plate remains stationary. Under so-called “no-slip” conditions, if we assume that the liquid layers in the vicinity of the plates have the same velocity as the plates themselves, the local velocities vary linearly across the gap due to a transfer of momentum between adjacent fluid layers. The resulting velocity gradient perpendicular to the shear direction is then precisely equal to the strain rate $\dot{\gamma}$. The shear viscosity η connects stress and strain rate via Newton’s law, $\tau = \eta\dot{\gamma}$. Fluids such as water or glycerol, which display a constant viscosity, independent of the shear rate, are therefore called Newtonian fluids while any

deviating behavior is referred to as non-Newtonian. If the viscosity increases with increasing shear rate, the sample behaves in a dilatant (shear-thickening) manner whereas, if the viscosity decreases, this is referred to as pseudo-plastic (shear-thinning) behavior.

Soft materials seldom behave exclusively as either pure elastic solids or viscous liquids. Instead, they display both properties simultaneously, a behavior which is therefore called viscoelastic. Viscoelastic properties can be probed by oscillatory shear experiments, during which a system is exposed to a sinusoidal strain $\gamma(t) = \gamma_0 \sin(\omega t)$ with amplitude γ_0 and angular frequency ω . If the overall deformation is small, the time-dependent stress $\tau(t) = \tau_0 \sin(\omega t + \delta)$ is a linear response function of $\gamma(t)$. The stress oscillates with the same frequency ω but displays a distinctive amplitude τ_0 and additionally a phase shift δ in relation to the incoming signal. The limit $\delta \rightarrow 0$, with τ and γ oscillating in phase, corresponds to pure elastic behavior. Conversely, an out-of-phase oscillation with $\delta \rightarrow \pi/2$ indicates a purely viscous response. The relationship between stress and strain can be conveniently formulated using complex notation as $\tau^*(t) = G^* \gamma^*(t)$, with the complex shear modulus $G^* = G' + iG''$ as a proportionality constant in analogy to Hooke's law. For small strain amplitudes $\gamma_0 \ll 1$, in the so-called linear-viscoelastic regime, the frequency-dependent complex modulus $G^*(\omega)$ contains the entire viscoelastic information of such a mechanical linear response system. Its real part $G'(\omega)$ is related to the energy which can be elastically stored during an oscillation cycle and is therefore called storage modulus, while the imaginary part $G''(\omega)$ represents the amount of dissipated energy and is as such referred to as the loss modulus.⁶⁰

1.2.2 Scattering Methods

Scattering experiments are well-established methods for investigating the structure and dynamics of colloidal many-particle systems.³⁸ In addition to visible light with wavelengths ranging from 400 nm to 800 nm and X-rays at about 0.1 nm, neutrons can also be used as probes, with cold neutrons having a wavelength roughly five times larger than and thus still comparable to X-rays.⁴⁰

Scattering processes can be described starting from Maxwell's equations⁶¹ which form the basis of classical electromagnetism and by employing the Huygens-Fresnel principle of wave diffraction.⁶² When matter is hit by an electromagnetic wave, each scattering center forms the source of a new spherical wave. The wave front resulting from the superposition of all spherical waves can be recorded at a sufficient distance from the detector as a plane wave. Additionally, we employ the Born approximation⁶³ and thus assume that the waves generated by different scattering centers are not perturbed by each other. A visual representation of such a process is given in Fig. 1.2, where a scattered electromagnetic wave $\mathbf{E}_S(\mathbf{r}_S, t)$ is generated by a plane wave $\mathbf{E}_P(\mathbf{r}_P, t)$ interacting with a particle. The resulting diffraction pattern can be detected as the intensity $I(\mathbf{Q})$.

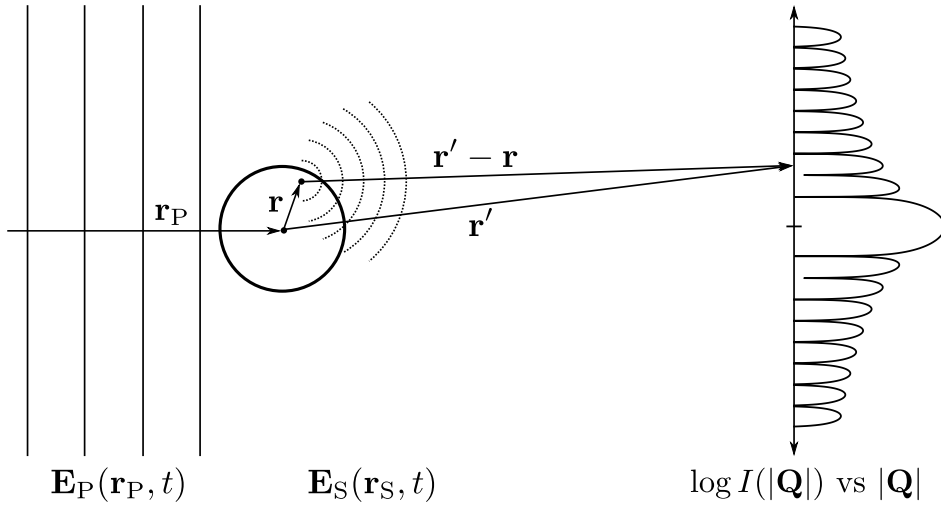


Figure 1.2: Schematic representation of a scattering process. An incoming plane wave is scattered by the infinitely many point-like scattering centers of a spherical particle. The resulting intensity pattern emerges from the interference of all scattered waves.

The scattering vector \mathbf{Q} is a central quantity for the description of scattering patterns and is defined as the difference between the wave vectors of the incoming beam \mathbf{k}_P and the scattered wave \mathbf{k}_S . A visual representation of this relationship is displayed in Fig. 1.3. Scattering processes can basically be divided into two categories: inelastic processes in which energy is transferred between probe and target and elastic processes where only momentum but no energy transfer occurs. In the case of elastic scattering with the incoming and outgoing wave vectors sharing the same magnitude $|\mathbf{k}_P| = |\mathbf{k}_S| = 2\pi n/\lambda$, the magnitude of the scattering vector $Q = 4\pi n/\lambda \sin(\gamma/2)$ can be expressed concisely by the vacuum wavelength of the radiation λ , the refractive index of the material n , and the scattering angle γ . The maximum attainable scattering vector is thus $Q_{\max} = 4\pi n/\lambda$ for backscattering at $\gamma = 180^\circ$. Since scattering methods probe length scales of the order $d \approx 2\pi/Q$, the spatial resolution of a scattering experiment is limited by $d_{\min} = \lambda/(2n)$, which is around 200 nm for light scattering and on the order of nanometers or less for X-ray and neutron scattering.⁴⁴

The scattered electric field of a single mesoscopic particle is proportional to the so-called scattering amplitude

$$b(\mathbf{Q}) = \int_V \rho(\mathbf{r}) e^{i\mathbf{Q}\cdot\mathbf{r}} d\mathbf{r}, \quad (1.1)$$

which is essentially the three-dimensional Fourier transform of the scattering contrast $\rho(\mathbf{r})$, i.e., the variation in scattering power between the particle and the surrounding medium. This difference varies depending on the type of probe used. Neutron scattering considers the scattering lengths of atomic nuclei, X-ray scatter-

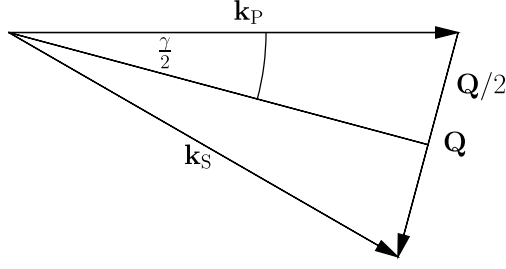


Figure 1.3: Visualization of the relationship between the incoming wave vector \mathbf{k}_P , the outgoing wave vector \mathbf{k}_S , the scattering vector \mathbf{Q} and the scattering angle γ .

ing considers the electron density of atoms, and visible light scattering considers the polarizability of the electron shell, which is linked to the refractive index. For spherically symmetric particles, the scattering amplitude only depends on the magnitude of the scattering vector and can thus be expressed via the one-dimensional Fourier-Bessel transform

$$b(Q) = 4\pi \int_0^\infty \rho(r) \frac{\sin(Qr)}{Qr} r^2 dr \quad (1.2)$$

of the radial contrast profile $\rho(r)$. The ensemble-averaged scattered intensity produced by an assembly of N spherical, possibly interacting particles is then apart from constant pre-factors given by⁶⁴

$$\langle I(Q) \rangle \propto \sum_{i,j=1}^N \langle b_i(Q) b_j(Q) \exp[i\mathbf{Q} \cdot (\mathbf{r}_i - \mathbf{r}_j)] \rangle, \quad (1.3)$$

where \mathbf{r}_i denotes the position of the particle with label i . The intensity of an ensemble of interacting particles is basically determined by two distinctive contributions: The correlations between scattering centers within each particle and the spatial correlations between different particles, which emerge from self-organization due to inter-particle forces. For monodisperse suspensions, with all scattering amplitudes being the same, these contributions can be rigorously separated according to

$$\langle I(Q) \rangle \propto N b^2(0) \underbrace{\frac{b^2(Q)}{b^2(0)}}_{P(Q)} \overbrace{\frac{1}{N} \sum_{i,j} \langle \exp[i\mathbf{Q} \cdot (\mathbf{r}_i - \mathbf{r}_j)] \rangle}_{S(Q)} \quad (1.4)$$

where we introduced the form factor $P(Q)$, which embodies the optical properties of the particles, and the structure factor $S(Q)$, which contains the structural information. A visual comparison between $P(Q)$, $S(Q)$ and the intensity as a

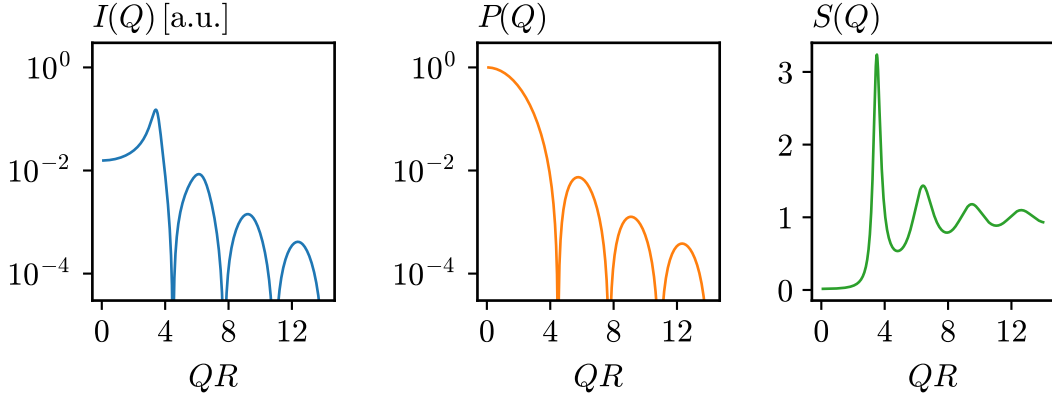


Figure 1.4: Comparison between the scattered intensity $I(Q) = P(Q)S(Q)$ and its two factors, the form factor $P(Q)$ and the structure factor $S(Q)$, for a monodisperse ensemble of optically homogeneous spheres with radius R , interacting via a hard-sphere potential.

product of both is exemplarily displayed in Fig. 1.4 for a model suspension consisting of monodisperse, optically homogeneous spheres interacting via a hard sphere potential.

From a statistical mechanics point of view, according to

$$S(Q) - 1 = 4\pi \int_0^{\infty} \rho [g(r) - 1] \frac{\sin(Qr)}{Qr} r^2 dr \quad (1.5)$$

the structure factor is related to the radial distribution function (RDF) $g(r)$ by a Fourier transform. $g(r)$ is associated with the probability of finding a particle at a distance r from another tagged particle relative to the ideal gas as a reference system with the same number density ρ . $S(Q)$ is as such simply a representation of $g(r)$ accessible from scattering experiments.⁶⁵ $g(r)$ or equivalently $S(Q)$ can be theoretically accessed by solving the Ornstein-Zernike integral equation⁶⁶

$$h(r_{12}) = c(r_{12}) + \rho \int c(r_{13})h(r_{23})d\mathbf{r}_3, \quad (1.6)$$

which relates the total correlation between particles 1 and 2, $h(r_{12}) = g(r_{12}) - 1$, to the direct correlations between these two particles, represented by the function $c(r_{12})$, and the indirect correlations mediated by a third particle. This recursive hierarchy provides an appealing physical picture of how the pair interaction between two particles is indirectly propagated through the entirety of a large many-body system. To solve Eq. (1.6), a physically motivated approximation which somehow relates either $c(r)$ or $h(r)$ to a given pair potential, a so-called closure relation, is needed. The only closure of interest for this work is the one given by Percus and Yevick⁶⁷, which allows the analytical calculation of structure factors of both single and multi-component hard sphere systems.⁶⁸⁻⁷¹

1.2.3 Photon Correlation Spectroscopy

Photon correlation spectroscopy (PCS), also referred to as dynamic light scattering (DLS), is a specialized scattering method for probing the dynamics of matter.⁴² In homodyne experiments, where only the photons scattered by the sample are detected, temporal correlations of the intensity $I(Q, t)$ are quantified by measuring the intensity correlation function (ICF)⁴¹

$$g_2(Q, t) = \frac{\langle I(Q, 0)I(Q, t) \rangle_t}{\langle I(Q, t) \rangle_t^2}. \quad (1.7)$$

Here, $\langle \dots \rangle_t$ denotes a time average. Such an auto-correlation function (ACF) basically represents the similarity of two time series after a certain delay time t between them. If the intensity fluctuations follow Gaussian statistics, ideally, the ICF starts at $\langle I^2 \rangle / \langle I \rangle^2 = 2$ for $t = 0$ and falls to $\langle I \rangle^2 / \langle I \rangle^2 = 1$ for $t \rightarrow \infty$ assuming all fluctuations decorrelate eventually.

The actual dynamics of the system are not directly encoded in the ICF, but rather in the auto-correlation function of the electric field,

$$g_1(Q, t) = \frac{\langle E^*(Q, 0)E(Q, t) \rangle_t}{\|\langle E(Q, t) \rangle_t\|^2}, \quad (1.8)$$

which for ergodic systems is connected to the ICF via the Siegert relation⁷²

$$g_2(Q, t) = 1 + \beta(Q)g_1^2(Q, t). \quad (1.9)$$

Here, additionally an instrument factor $\beta(Q)$ is introduced which depends on the optical alignment, the detector area and the coherence of the radiation but is relatively close to unity for optical fiber based single-photon detectors.⁷³

For monodisperse suspensions of identical particles $g_1(Q, t)$ is equivalent to the intermediate scattering function (ISF) $S(Q, t)$ normalized to the static structure factor $S(Q)$, i.e.,

$$g_1(Q, t) = \frac{S(Q, t)}{S(Q, 0)} = \frac{\frac{1}{N} \left\langle \sum_{ij} \exp[i\mathbf{Q} \cdot (\mathbf{r}_i(t) - \mathbf{r}_j(0))] \right\rangle}{\frac{1}{N} \left\langle \sum_{ij} \exp[i\mathbf{Q} \cdot (\mathbf{r}_i(0) - \mathbf{r}_j(0))] \right\rangle}. \quad (1.10)$$

The ISF $S(Q, t)$ describes the temporal evolution of the spatial inter-particle correlations and can thus be seen as the dynamical extension of the structure factor $S(Q)$.⁶⁵

In weakly interacting systems the particles show no spatial correlations, which means $S(Q) = 1$, and they essentially exhibit free Brownian motion in a viscous medium. In this case the ISF takes the familiar form⁴¹

$$S(Q, t) = e^{-D_0 Q^2 t} \quad (1.11)$$

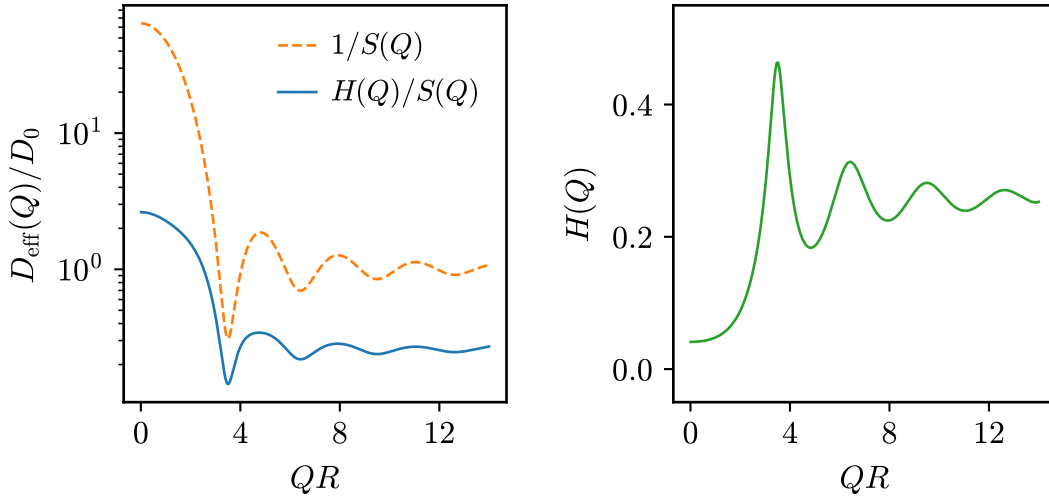


Figure 1.5: Left: Comparison between the reduced effective short-time diffusion coefficient $D_{\text{eff}}(Q)/D_0$ for a monodisperse ensemble of hard spheres with radius R , with HIs included [$H(Q)/S(Q)$] and with HIs neglected [$1/S(Q)$]. Right: Wave-vector dependence of the hydrodynamic function $H(Q)$ of the same system.

from the solution of the diffusion equation in Fourier space. $D_0 = k_B T / (6\pi\eta R_h)$ is the well-known Stokes-Einstein diffusion coefficient representing the ratio between the thermal energy $k_B T$ and the drag coefficient of a sphere with hydrodynamic radius R_h in a medium with viscosity η .

In strongly interacting systems that self-organize into ordered structures the dynamics of colloidal particles is determined not only by the self-diffusion of individual particles but also by collective motion. In the short-time regime, for correlation times larger than the momentum relaxation time but smaller than the structural relaxation time, the expansion⁶⁴

$$S(Q, t) = S(Q) \left[1 - D_0 \frac{H(Q)}{S(Q)} Q^2 t + \mathcal{O}(t^2) \right] \quad (1.12)$$

characterizes the initial decay of the ISF. Comparing this result to the power series expansion of the exponential in Eq. (1.11) we identify

$$D_{\text{eff}}(Q) = D_0 \frac{H(Q)}{S(Q)} \quad (1.13)$$

as an effective, wave-vector-dependent, short-time diffusion coefficient. As evident, in addition to $S(Q)$, a second factor, the hydrodynamic function $H(Q)$, contributes to the wave-vector dependence of the diffusivity. $H(Q)$, exclusive to colloidal systems, accounts for indirect, retarded interactions that are mediated by the dispersion medium.⁷⁴ These additional forces are absent in simple atomic

liquids, where the atoms move in a vacuum between collisions. Eq. (1.13) can be considered a colloid analog of the well-known de Gennes narrowing⁷⁵ observed in inelastic neutron scattering spectra of structured molecular liquids. De Gennes narrowing basically states the intuitive principle that collective motion is particularly slow on length scales where a system is highly ordered. $D_{\text{eff}}(Q)$ thus shows a minimum at the location of the structure factor peak. This is exemplified in Fig. 1.5 which displays the wave-vector dependence of $D_{\text{eff}}(Q)$ of a concentrated hard-sphere suspension with hydrodynamic interactions (HIs) included. For comparison, the expected result without HIs, i.e. $H(Q) = 1$, is also shown along with the wave-vector dependence of the isolated hydrodynamic function. $H(Q)$ and $S(Q)$ share the same oscillating features and display local maxima at roughly the same locations, stressing that both quantities are highly connected.

1.2.4 Mode-Coupling Theory

Mode-coupling theory (MCT) is a well-established approach for theoretically calculating time-dependent correlation functions based solely on static, time-independent inputs.^{12,76} The theory aims to predict the time dependence of the ISF $S(Q, t)$ for a given material starting from the exact dynamics of a particle diffusing in a potential. By using the projection-operator formalism by Mori and Zwanzig, the equations of motion can be simplified by eliminating fast, randomly fluctuating degrees of freedom from the system, leaving only the time evolution of the slowly varying observables.^{53,54}

For illustrative purposes, here, the equations for the time evolution of $S(Q, t)$ for a monodisperse ensemble of overdamped Brownian particles without HIs are presented. They are given by^{77,78}

$$\frac{\partial}{\partial t} S(Q, t) + \frac{D_0 Q^2}{S(Q)} S(Q, t) + \int_0^t M(Q, t - t') \frac{\partial}{\partial t'} S(Q, t') dt' = 0. \quad (1.14)$$

According to this formalism, the time dependence of $S(Q, t)$ is governed, beyond the initial decay $D_0 Q^2/S(Q)$, by the memory kernel $M(Q, t)$ which is formally defined as the auto-correlation function of the fluctuating force. From a phenomenological perspective, the memory function can be seen as a generalized friction coefficient that mediates time-retarded memory effects. These effects accumulate as particles move through the energy landscape of the system.

The core idea of MCT is now precisely that this memory function can be approximated by a term of the form

$$M(Q, t) = \frac{\rho D_0}{2(2\pi)^3} \int V^2(\mathbf{Q}, \mathbf{k}) S(k, t) S(|\mathbf{Q} - \mathbf{k}|, t) d\mathbf{k}, \quad (1.15)$$

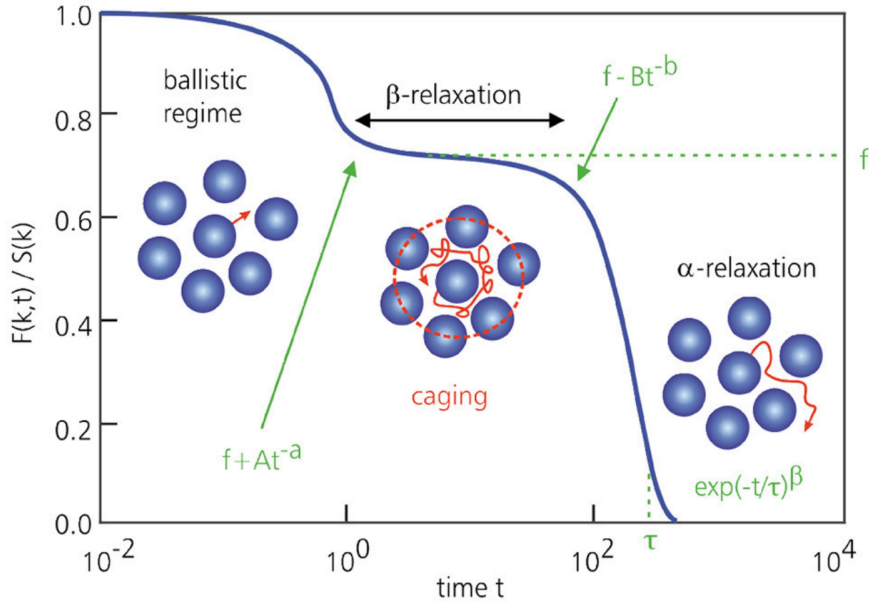


Figure 1.6: Schematic illustration of the phenomenology of supercooled glass-forming liquids as predicted by MCT. Note that here, the wave vector is denoted by k and the intermediate scattering function is denoted by $F(k, t)$. (Reproduced from Janssen¹² under the terms of the Creative Commons Attribution License (CC BY).)

where the integrand consists of products of the ISF $S(Q, t)$ and of the so-called vertex amplitude $V(\mathbf{Q}, \mathbf{k})$ which can be calculated solely from the static structure factor $S(Q)$ and the number density ρ . As such, the memory function given within MCT provides a self-consistent closure for solving Eq. (1.14).

MCT is considered a very successful theory in a sense that it captures the most important aspects of the phenomenology of glass-forming liquids.^{12,79} This is schematically illustrated in Fig 1.6: Weakly interacting, ergodic systems are characterized by free Brownian motion of the particles. In contrast, in strongly interacting systems the diffusion of a central particle in the coordination cage of its nearest neighbors is restricted. For short times, diffusion is therefore only possible within this coordination cage, which is also referred to as the β -process. The movement of a particle over long distances is only possible if the neighboring particles participate cooperatively or if the central particle can overcome its coordination cage. These escape processes, known as the α -process, occur with lower probability and are characterized by significantly longer relaxation times than those of the β -process. In deeply supercooled liquids, both regimes are clearly separated by an intermediate plateau in $S(Q, t)$. The height of this plateau $f(Q)$ is called non-ergodicity parameter or Debye-Waller factor. The region around the plateau is characterized by two universal power-laws, $f + At^{-a}$ and $f - Bt^{-b}$, which respectively describe

the approach and the departure from the plateau. Remarkably, both power-law exponents are connected by a consistent scaling relation⁸⁰ given by

$$\lambda = \frac{\Gamma(1-a)^2}{\Gamma(1-2a)} = \frac{\Gamma(1+b)^2}{\Gamma(1+2b)} \quad (1.16)$$

where $\Gamma(x)$ denotes the Gamma function. λ is called the exponent parameter. At very long times, the α -relaxation can be well described by a stretched exponential decay according to $S(Q, t) \propto \exp[-(t/\tau_\alpha)^\beta]$.⁸¹

For even stronger correlated systems, the interactions are so strong that a central particle cannot escape its coordination cage in a finite time and $S(Q, t)$ simply decays to the Debye-Waller factor $f(Q)$ with a diverging α -relaxation time. This is MCT's celebrated prediction of a glass transition.⁸²

A very attractive approach to MCT is the reduction of the full wave-vector-dependent theory to schematic, wave-vector-independent models⁸³ which provide the freedom to describe arbitrary relaxation processes, not just those directly coupled to density correlations. These simplified models do not rely on any static inputs and instead resort to adjustable parameters. Consequently, they are widely popular for the characterization of rheological⁸⁴⁻⁸⁶ and dielectric relaxation⁸⁷ experiments, particularly when non-linear properties are probed. An established, very basic schematic model is the F_{12} -model proposed by Götze,⁵³ which describes the time evolution of a generalized correlation function $\Phi(t)$ by

$$\frac{1}{\Gamma} \frac{\partial}{\partial t} \Phi(t) + \Phi(t) + \int_0^t m(t-t') \frac{\partial}{\partial t'} \Phi(t') dt' = 0, \quad (1.17)$$

where the memory function $m(t) = v_1 \Phi(t) + v_2 \Phi^2(t)$ is a simple quadratic expansion in $\Phi(t)$. The coefficients v_i act as substitutes for the wave-vector-dependent vertex amplitudes. At the non-ergodicity transition, within this model, the critical vertices $v_1^c = (2\lambda - 1)/\lambda^2$ and $v_2^c = 1/\lambda^2$ and the critical Debye-Waller factor $f_c = 1 - \lambda$ show an intriguing connection to the exponent parameter λ from Eq. (1.16).⁸⁸

This introductory description portrays only a small subset of the full capabilities of mode-coupling theory. The systems and phenomena investigated in this thesis show an increased complexity and require advanced mode-coupling schemes for the treatment of multi-component systems,⁷⁸ for the evaluation of transport coefficients like diffusion constants⁸⁹ or shear viscosities⁹⁰ and for the application to linear and non-linear rheology.^{91,92}

2 Research Overview

2.1 Characterization of a Novel Model Hard-Sphere System

Sterically stabilized poly(methyl methacrylate) (PMMA) particles suspended in non-polar media are among the most commonly used colloidal model systems for the experimental study of hard spheres.¹⁶ Since the preparation of hard sphere model suspensions was not an established method within our group, the first part of this work focuses on the preparation, characterization and validation of such a system, which will serve as a starting point for future investigations. The dispersion in question has to meet several target properties: It should be easy to prepare in a reproducible way, suitable for light scattering experiments and, of course, exhibit the structure and dynamics expected for a hard sphere system.

2.1.1 Preparation of Poly(dimethylsiloxane)-Stabilized Poly(methyl methacrylate) Particles

PMMA-based suspensions in non-polar media are commonly prepared by employing dispersion polymerization in presence of a stabilizing agent, which results in particles with a solid PMMA core surrounded by a shell of grafted polymer chains whose steric hindrance prevents the aggregation of individual particles.⁹³ The most established stabilizer is a poly(12-hydroxystearic acid) (PHSA) comb polymer whose synthesis is well studied⁹⁴ but is considered laborious and requires a lot of experience. Despite its proven suitability as a hard sphere system, multiple groups pointed out reproducibility problems when trying to synthesize particles from different PHSA batches, even when identical protocols were followed.^{94–96} In search of a more controllable system, it was decided to explore a promising alternative, namely, stabilizers based on monomethacryloxypropyl-terminated poly(dimethylsiloxane) (PDMS-MA).^{97,98} In contrast to their PHSA counterparts, these poly(dimethylsiloxane) (PDMS) stabilizers are commercially available and, due to their reactive end-group functionalization, can be directly copolymerized with methyl methacrylate (MMA), which greatly simplifies the preparation. The synthesis and the influence of varying reaction conditions on particle size and polydispersity is well documented in the literature,⁹⁹ where a potential use in electrophoretic display applications is suggested.¹⁰⁰ For this work, a batch of PMMA-PDMS particles was synthesized based on recipes provided by Richez et al.¹⁰⁰ and Hallett et al.⁹⁶, as described in-depth in **Publication II**. In short, as typical for a free-radical dispersion polymerization,¹⁰¹ a monomer mixture consisting of MMA and PDMS-MA is dissolved in an appropriate solvent,

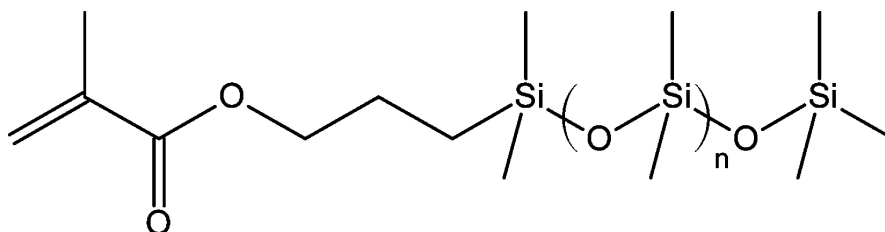


Figure 2.1: Structure of monomethacryloxypropyl-terminated poly(dimethylsiloxane) used as steric stabilizer for the described PMMA-PDMS particles, with $n \approx 130$. (Reproduced from Hallett et al.⁹⁶ under the terms of the ACS AuthorChoice License.)

in this case n -dodecane. In presence of 1-octanethiol as a chain transfer agent and azobisisobutyronitrile (AIBN) as a radical initiator a stable colloidal suspension consisting of spherical polymer particles sterically stabilized by the grafted PDMS chains is formed. To produce suspensions suitable for light scattering experiments, the particles were transferred to a refractive index matching mixture of decahydronaphthalene (decalin) and 1,2,3,4-tetrahydronaphthalene (tetralin) with $n_D^{20} = 1.496$. Refractive index matching eliminates multiple scattering making samples appear optically transparent to the human eye. This procedure also suppresses residual van der Waals attractions between the mesoscopic spheres,¹⁰² leaving only excluded volume interactions, which are the defining forces for hard particles.^{103,104} This study partly builds upon the work of Hallett et al.⁹⁶, who investigated diluted suspensions of very similar particles via small-angle neutron scattering (SANS). Their results essentially confirm the picture of a spherical particle with a dense core of mainly PMMA surrounded by a layer of grafted PDMS chains extending radially into the suspending medium. The particles prepared in this work differ from Hallett's particles in terms of their detailed chemical structure with regard to the end groups: In this work, only one side of the stabilizer chain is functionalized with a reactive end group (see Fig. 2.1), resulting in a chain grafted onto a single anchor point on the core's surface. In contrast, Hallett used PDMS with both terminal ends esterified, causing the grafted chains to instead form loop-like structures, which however still provide an adequate steric stabilization. Additionally, different to the suspensions used in this work, n -dodecane is used as the dispersion medium in Hallett's study, since there is no direct need to employ optical index-matching solvents for neutrons as a probe. Since decalin and tetralin are both hydrocarbons with comparable chemical and physical properties, a solvent mixture of those two compounds is expected to provide a chemical environment similar to dodecane. Apart from tetralin and decalin, halogenated hydrocarbons such as bromocyclohexane, bromocycloheptane, tetrachloroethene or tetrachloromethane¹⁶ constitute popular choices as suspension media with larger mass density, especially for colloids suitable for confocal microscopy, which requires larger particles for the efficient tracking of particle positions in real space.³⁶ In addition to refractive

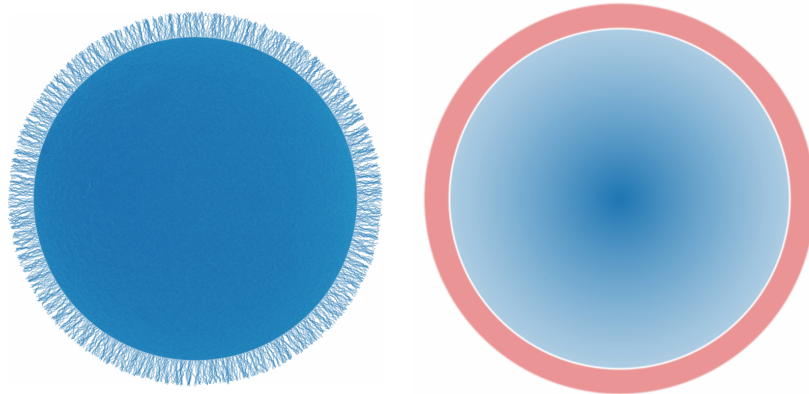


Figure 2.2: Left: Schematic illustration of the PMMA-PDMS particles investigated in this work, with a realistic ratio between the size of the PMMA core and the grafted PDMS chains. Right: Two dimensional representation of the scattering contrast based on the core-shell model described in the text.

index matching, this application needs solvent mixtures to also match the mass density of the particles to prevent sedimentation. As an undesired side effect, often, particles in halogenated media acquire surface charges, which is particularly harmful in such low dielectric constant solvents ($\epsilon_r \approx 10$), where unscreened electrostatic interactions become very long-ranged and even the addition of salts such as tetrabutylammonium bromide results in Debye-Hückel screening lengths of the order $\lambda_D \approx 100$ nm, clearly not suitable to emulate hard-sphere systems with particles on a nanometer scale.^{16,20,105} Surprisingly however, Kale et al.¹⁰⁶ recently showed that a mixture of decalin and tetrachloroethene indeed yields suspensions of PMMA-PHSA particles suitable for confocal microscopy which quantitatively conform to a hard-sphere fluid structure. Nevertheless, since there is no need to employ density-matching solvents for scattering studies of submicron-sized particles, it was decided to settle for decalin-tetralin mixtures, which are a well studied system. It is well known that tetralin, which is a somewhat good solvent for PMMA, displays a tendency to slightly swell suspended particles due to the diffusion of a fraction of the solvent molecules into the core.^{107,108} It is believed that this does not affect the interaction potential between particles if the suspensions are given enough time to equilibrate, although the effect will be noticeable when analyzing the distribution of the scattering length density (SLD) inside the core.

2.1.2 Particle Morphology

To understand the optical properties of the synthesized PMMA-PDMS colloids on an individual particle level which will turn out to be essential for describing the structure and dynamics of concentrated suspensions, in **Publication II**, the

particle topology is investigated by means of static light scattering (SLS) experiments. It is found that the scattering properties of the individual particles can be well described by a coarse-grained core-shell model with a constant scattering contrast of the shell, combined with a gradient of the SLD inside the core, which is caused by the penetration by tetralin. Fig. 2.2 shows an illustrative comparison between a schematic, though proportionally realistic, depiction of what such a particle might look like based on our current knowledge and the coarse-grained representation of the SLD employed for the following form factor analysis. Within this model, the scattering contrast profile $\rho(r)$ as a function of the distance r from the core center is represented by

$$\rho(r) = \begin{cases} \rho_0 + (\rho_R - \rho_0) \frac{r}{R_c}, & \text{for } R_c \geq r, \\ \rho_\Delta, & \text{for } R_c + \Delta \geq r > R_c, \\ 0, & \text{for } r > R_c + \Delta. \end{cases} \quad (2.1)$$

Here, R_c denotes core radius, Δ is the shell thickness, and ρ_0 , ρ_R and ρ_Δ respectively refer to the contrast at the core center, at the core-shell boundary and inside the shell. The single-particle scattering amplitude $b(Q)$ can be inferred from this contrast profile via the Fourier-Bessel transform defined in Eq. (1.2).

It is further assumed that the size distribution of the suspensions can be modeled after the Schulz-Flory distribution^{109,110} with probability density function

$$c(R) = \frac{1}{\Gamma(Z+1)} \left(\frac{Z+1}{\langle R \rangle} \right)^{Z+1} R^Z \exp \left(- \frac{Z+1}{\langle R \rangle} R \right), \quad (2.2)$$

which is commonly employed to describe the molecular mass distribution of synthetically prepared polymers. $\langle R \rangle$ denotes the average total radius of a particle and the shape parameter Z is connected with the size dispersity, defined as the standard deviation relative to the size average, via $(\langle R^2 \rangle - \langle R \rangle^2)^{1/2} / \langle R \rangle = (Z+1)^{-1/2}$.

The form factor $P(Q)$ of such a polydisperse system is then given by an average of the squared scattering amplitude $b^2(Q)$ over the size distribution.^{44,64} Following Bartlett and Ottewill,¹¹¹ the shell thickness is assumed to be constant such that only the core size is distributed according to Eq. (2.2). This is reasonable because the shell thickness is essentially predetermined by the average chain length of the stabilizer. A representative form factor $P(Q)$ obtained from a least-squares fit of the described model to the experimentally obtained intensity of a dilute suspension is depicted in Fig. 2.3, together with the corresponding radial contrast profile $\rho(r)$. Inspecting $P(Q)$ in detail, the portrayed form factor shows a somewhat unusual shape compared to form factors of particles with a homogeneous SLD, like in Fig. 1.4. Form factors of optically homogeneous particles are characteristically bounded from above by the low-wave-vector limit $P(0) = 1$. In contrast, the form factor in Fig. 2.3 locally exceeds $P(Q) = 1$ and peaks at the finite wave

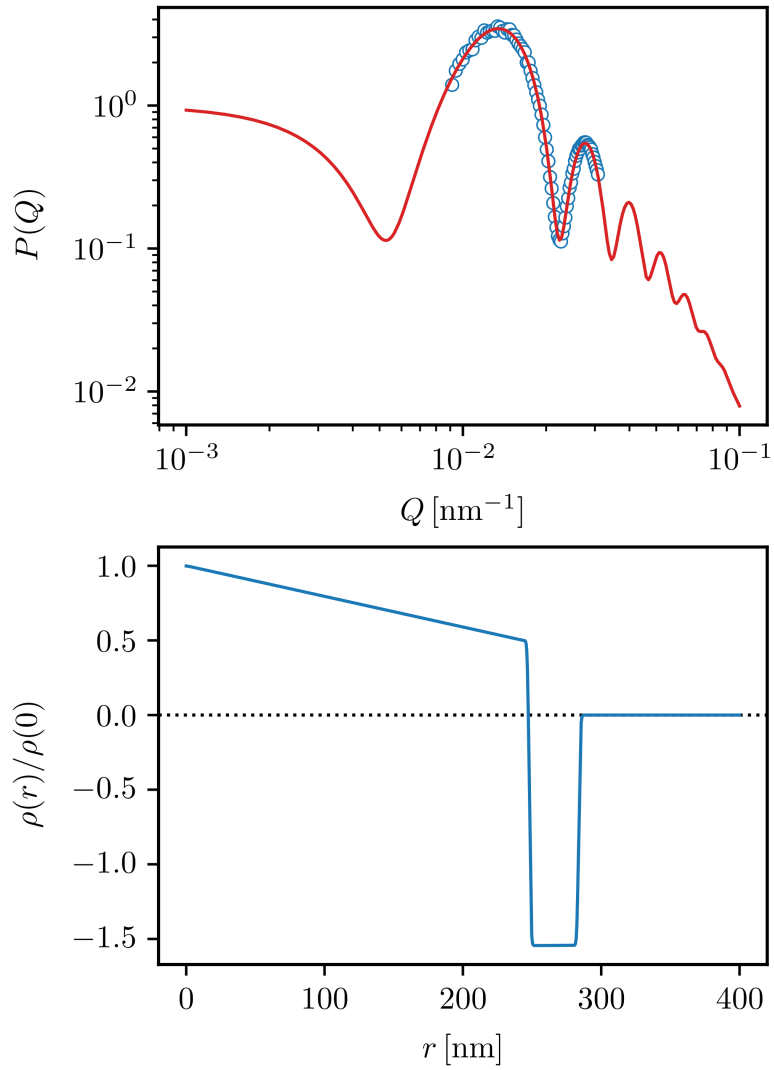


Figure 2.3: Top: Experimentally obtained form factor $P(Q)$ of a dilute suspension of the investigated PMMA-PDMS particles. The solid line is the best fit of the polydisperse core-shell model described in the text. Bottom: Corresponding radial contrast profile $\rho(r)$, normalized to $\rho(0)$. The dotted line is a guide to the eye for $\rho = 0$.

vector $Q \approx 0.01 \text{ nm}^{-1}$. This is the result of the contrast matching procedure, in which the refractive index of the decalin-tetralin solvent mixture is selected to minimize the total scattering cross-section. As a consequence, the core-shell particles have a refractive index of the surrounding medium between that of the PDMS shell and the PMMA core, with the forward scattering contribution significantly reduced. The form factors of such index-matched particles with inhomogeneous SLD distributions are explored in detail in **Publication III**, where it is shown that a detailed knowledge of the optical properties of scatterers is essential to correctly interpret scattering experiments of dense, correlated hard-sphere suspensions.

The topological analysis is extended to particles in more concentrated suspensions by adopting an enhanced model which also takes the hard-sphere structure of correlated multi-component systems into account. Surprisingly, the shell thickness is not independent of the effective hard-sphere volume fraction φ_{eff} . Instead, the shell is observed to shrink for increasing number density. This is illustrated in Fig. 2.4, which also shows two-dimensional representations of the scattering contrast distribution of a dilute and a concentrated suspension to visualize the magnitude of the shrinkage effect relative to the overall particle size. At low volume fractions, the thickness of the shell exhibits a plateau value of 37 nm, which remains nearly constant regardless of the volume fraction until a critical value of $\varphi_{\text{eff}} \approx 0.5$ is reached. Beyond this point, the shell begins to shrink. In a highly concentrated suspension at $\varphi_{\text{eff}} = 0.59$, the thickness decreases to only 25 nm. This effect is not investigated in more detail, but it is suspected that the crowded environment in a dense particle suspension may favor a more coiled conformation of the PDMS polymer chains, thus reducing the overall thickness of the stabilizer layer.

2.1.3 Measurable Structure Factors of Optically Inhomogeneous Particles

As stated in section 1.2.2, the average scattered intensity of a many particle system,

$$\langle I(Q) \rangle \propto \sum_{i,j=1}^N \langle b_i(Q) b_j(Q) \exp[i\mathbf{Q} \cdot (\mathbf{r}_i - \mathbf{r}_j)] \rangle, \quad (2.3)$$

is given by what is essentially the sum of a product of single-particle scattering amplitudes $b(Q)$ weighted by a phase factor $\exp[i\mathbf{Q} \cdot (\mathbf{r}_i - \mathbf{r}_j)]$, which depends on the position of two particles i and j . This general expression is now specified by considering a multi-component system consisting of n distinct classes of particles, where the constituents of each class are indistinguishable. The composition of the system is specified by the number fractions $x_\alpha = N_\alpha/N$, which relate the number of particles N_α belonging to species α to the total particle count N . In such a

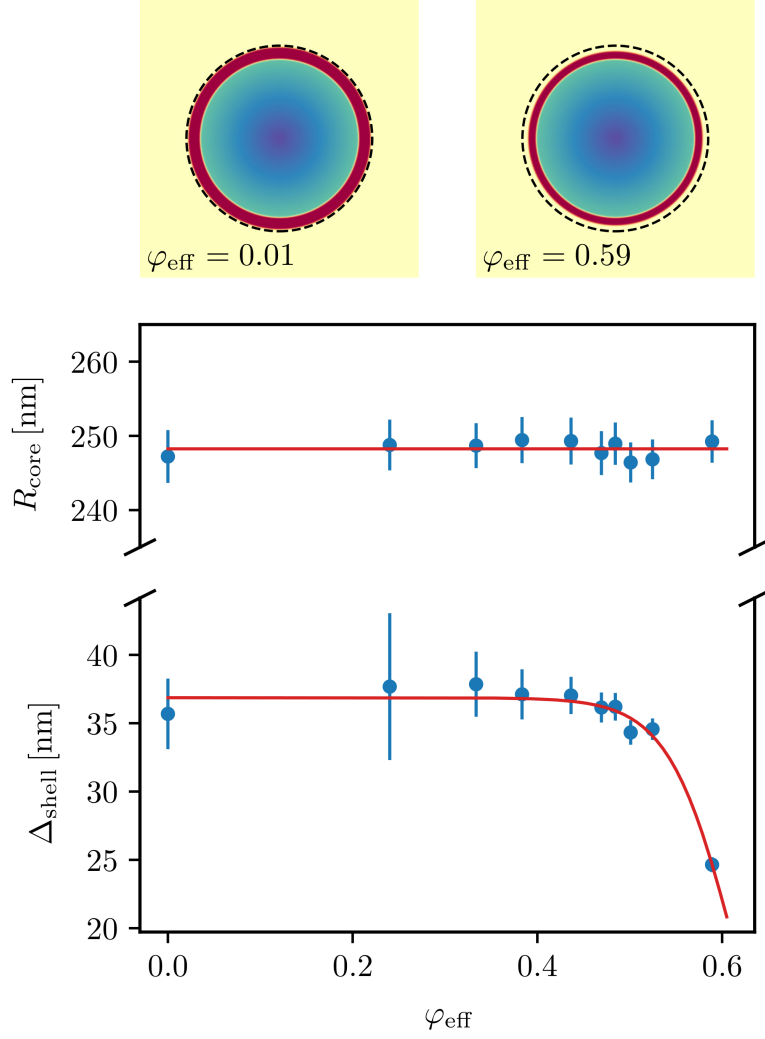


Figure 2.4: Top: False-color representation of the scattering contrast of the particles under investigation to provide insight into the ratio of core size to shell thickness in both dilute (left) and concentrated (right) samples. Bottom: The mean radius of the particle cores R_{core} and the shell thickness Δ_{shell} as a function of the effective hard-sphere volume fraction φ_{eff} , with the solid lines being a guide to the eye.

case, Eq. (2.3) can be reformulated as

$$\langle I(Q) \rangle \propto \sum_{\alpha, \beta=1}^n (x_\alpha x_\beta)^{1/2} b_\alpha(Q) b_\beta(Q) S_{\alpha\beta}(Q), \quad (2.4)$$

by introducing the partial structure factors⁶⁵

$$S_{\alpha\beta}(Q) = \frac{1}{(N_\alpha N_\beta)^{1/2}} \left\langle \sum_{i=1}^{N_\alpha} \sum_{j=1}^{N_\beta} \exp [i\mathbf{Q} \cdot (\mathbf{r}_i - \mathbf{r}_j)] \right\rangle. \quad (2.5)$$

As this formalism assumes mixtures with a finite number of species, continuous size distributions like the Schulz-Flory distribution from Eq. (2.2) must be discretized with an appropriate method. For this particular distribution, this is achieved very conveniently by employing a technique by D'Aguanno and Klein,¹¹² which exploits the connection between the Schulz-Flory function and the generalized Gauss-Laguerre quadrature rule.¹¹³ With this method, a discrete mixture of n species is guaranteed to match the first $2n - 1$ moments $\langle R^n \rangle$ of the continuous distribution.

In **Publication II**, the experimentally obtained intensities of concentrated suspensions of PMMA-PDMS particles are modeled quantitatively by using Eq. (2.4) in conjunction with the previously described core-shell model for the single-particle scattering properties and partial structure factors $S_{\alpha\beta}(Q)$ obtained from the analytical solution of the multi-component Ornstein-Zernike equation for hard spheres within the Percus-Yevick-closure. Because of this quantitative agreement in the whole range of investigated volume fractions, from diluted dispersions all the way up to the glass transition at $\varphi_{\text{eff}} = 0.59$, it is concluded that the prepared suspensions can be structurally regarded as effective hard-sphere systems, thus proving the applicability of PMMA-PDMS particles as a legitimate hard-sphere model system.

Direct fitting of experimentally obtained intensities with such a comparatively complex model is not necessarily the most commonly employed analysis method. An often used approach, which is motivated by the factorization property $I(Q) \propto P(Q)S(Q)$ [see Eq. (1.4)] of monodisperse suspensions, is simply dividing the intensity of an ordered sample by the intensity of a diluted, disordered dispersion while simultaneously accounting for the difference in number densities. This gives access to the so-called measurable structure factor $S_M(Q)$, which is then analyzed to obtain information on the ordering of particles. It is important to recognize that this approach would not have been suitable for investigating our particular samples: As can be deduced from the evolution of the shell thickness with changing volume fraction in Fig. 2.4, the form factor of a dilute suspension is in our case not the same as in a concentrated sample. Since however, from our advanced model, form factors for any given concentration, not just in the diluted case, can be readily

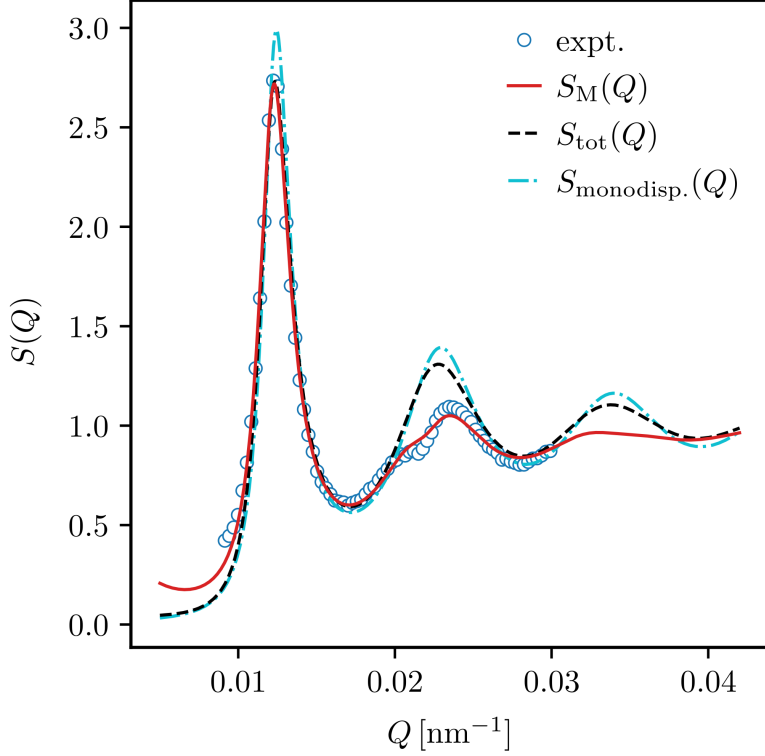


Figure 2.5: Measurable structure factor $S_M(Q)$ of a suspension of PMMA-PDMS particles with an effective hard-sphere volume fraction of $\varphi_{\text{eff}} = 0.50$ and a mean radius of $\langle R \rangle = 282 \text{ nm}$ compared to the total structure factor $S_{\text{tot}}(Q)$ and a monodisperse structure factor corresponding to the same system parameters.

accessed, $S_M(Q)$ can nevertheless be theoretically acquired from Eq. (2.4), which results in

$$S_M(Q) = \frac{1}{\langle b^2(Q) \rangle} \sum_{\alpha, \beta=1}^n (x_\alpha x_\beta)^{1/2} b_\alpha(Q) b_\beta(Q) S_{\alpha\beta}(Q), \quad (2.6)$$

where $\langle b^2(Q) \rangle = \sum_\alpha x_\alpha b_\alpha^2$ is short for the size average of the squared scattering amplitude. In Fig. 2.5, the measurable structure factor for a sample of PMMA-PDMS particles with $\varphi_{\text{eff}} = 0.50$ is exemplarily visualized. Therein, $S_M(Q)$ is compared to two other structure factors: the average of the partial structure factors (also termed total structure factor)

$$S_{\text{tot}}(Q) \equiv \langle S(Q) \rangle = \sum_{\alpha, \beta=1}^n (x_\alpha x_\beta)^{1/2} S_{\alpha\beta}(Q) \quad (2.7)$$

and the structure factor of a monodisperse suspension with the same volume fraction. It is evident that neither of these two structure factors accurately describes the experimental data over the entire accessible wave-vector range.

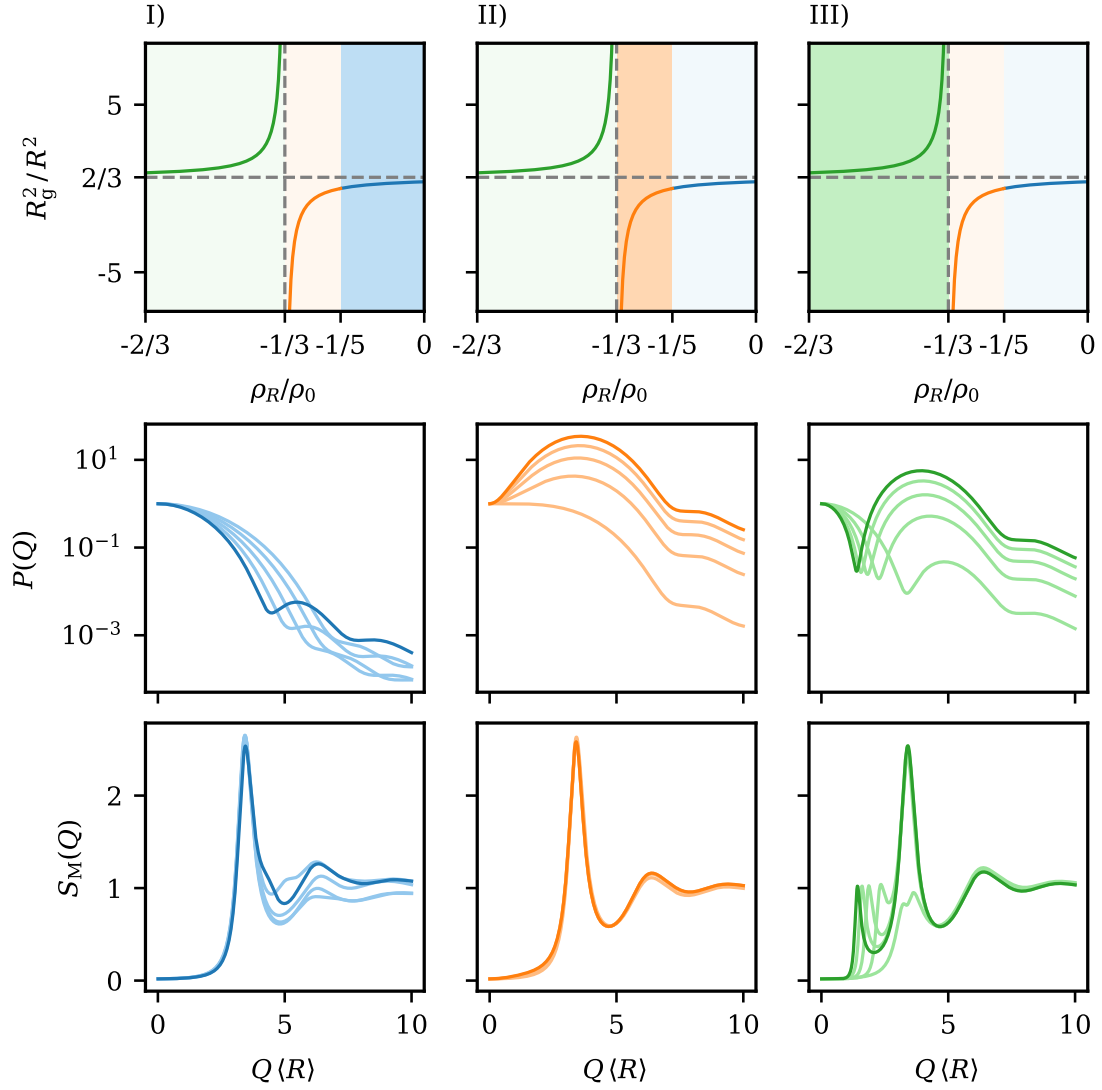


Figure 2.6: Breakdown of the classification of the scattering functions of spheres with a linear contrast gradient into the three regimes introduced in the text. Each column corresponds to a unique region. The top row depicts the reduced, squared radius of gyration R_G^2/R^2 in dependence on the contrast ratio ρ_R/ρ_0 . The darker shaded area indicates the location of the respective region labeled I), II) or III). $P(Q)$ and $S_M(Q)$ are shown in the middle and lower row, respectively, to indicate the variation of shapes, depending on the contrast.

Necessarily, the question arises to what extent the deviation between the measurable structure factor $S_M(Q)$, which is influenced by optical properties, and the average structure factor $\langle S(Q) \rangle$, which contains only structural information, depends on the specific particle model and on the polydispersity of the sample. An in-depth analysis of the influence of optical properties of individual particles on measurable structure factors of dense hard-sphere suspensions is conducted in **Publication III**. Therein, two simplified, prototypical optically inhomogeneous model particles are systematically investigated: Spheres with a linear profile of the SLD as a model for particles with continuous contrast gradients and core-shell systems as a prototype for layered particles. Based on the findings of this study it can be concluded that the behavior of measurable structural factors in dense hard-sphere suspensions is highly dependent on the optical properties of the individual particles. However, this dependence is more general than expected and is not tied to a particular particle model. Measurable structure factors can be categorized into three different classes of shared qualitative behavior, which is visualized in Fig. 2.6 for a model particle with a linear contrast gradient. The classification is based on the behavior of the form factor $P(Q)$ for small wave vectors, in the so-called Guinier region. This regime is characterized by the low-wave-vector expansion

$$P(Q) = 1 - \frac{R_G^2}{3}Q^2 + \mathcal{O}(Q^4), \quad (2.8)$$

which illustrates the dependence of the initial slope of $P(Q)$ on the radius of gyration R_G . For optically homogeneous particles, R_G is a characteristic quantity related to the specific geometry of the body. As an example, the radius of gyration of an optically homogeneous sphere is trivially related to the particle radius R by $R_G^2 = 3R^2/5$. For optically inhomogeneous particles, R_G is contrarily not solely determined by the particle geometry and should therefore be viewed in a more abstract sense. Consider for example a sphere characterized by a linear gradient of the SLD, with a one-dimensional contrast profile given by

$$\rho(r) = \begin{cases} \rho_0 + (\rho_R - \rho_0)\frac{r}{R}, & \text{if } 0 \leq r \leq R, \\ 0, & \text{otherwise,} \end{cases} \quad (2.9)$$

where R denotes the radius, ρ_0 is the scattering contrast in the center and ρ_R is the contrast at the surface of the particle. From the resulting scattering amplitude

$$b(Q) = 4\pi \left[\rho_0 \frac{\sin(QR) - QR \cos(QR)}{Q^3} + \frac{\rho_R - \rho_0}{R} \times \frac{2QR \sin(QR) - [(QR)^2 - 2] \cos(QR) - 2}{Q^4} \right], \quad (2.10)$$

with

$$b(0) = \pi R^3 \left(\frac{\rho_0}{3} + \rho_R \right), \quad (2.11)$$

formally, the following expression for the radius of gyration can be derived:

$$R_G^2 = \frac{2}{5} \frac{\rho_0 + 5\rho_R}{\rho_0 + 3\rho_R} R^2. \quad (2.12)$$

Clearly, R_G not only depends on the radius R , but additionally on the ratio between the two contrasts, ρ_R/ρ_0 . Plotting R_G^2/R^2 as a function of ρ_R/ρ_0 results in hyperbola-like curves (see the top row of Fig. 2.6), which can be divided into three characteristic regions:

- I) For $\rho_R/\rho_0 > -1/5$, R_G^2 is positive and thus, the form factors $P(Q)$ have a negative initial slope. The form factors in this regime show a qualitative behavior known from optically homogeneous spheres, which are included in the model as the special case $\rho_R/\rho_0 = 1$. Around its principal peak and for lower wave vectors, $S_M(Q)$ is almost unaffected by contrast variation, contrary to larger wave vectors, where the measurable structure factor shows shoulder-like artifacts roughly corresponding to the locations of the form factor minima.
- II) For the contrast ratios $-1/3 < \rho_R/\rho_0 < -1/5$, R_G^2 is negative, which technically implies that the radius of gyration R_G itself becomes imaginary. The initial decay of $P(Q)$ is then positive and the form factors exhibit a maximum at a finite wave vector. Interestingly, in this regime, $S_M(Q)$ shows almost no dependence on the contrast ratio.
- III) For $\rho_R/\rho_0 < -1/3$, R_G^2 is again positive. $\rho_R/\rho_0 = -1/3$ is, as evident from Eq. (2.11), exactly the condition for which a suspension shows almost no forward scattering and appears optically transparent. In this regime, $P(Q)$ is characterized by a prominent, comparatively sharp minimum at low wave vectors, which results in the appearance of an additional low- Q maximum in $S_M(Q)$, very reminiscent of cluster peaks found in model systems with competing short-range attractive - long-range repulsive interactions.^{114,115} It is important to recall that this effect here is caused solely by the optical properties of the system. This stresses that an uninformed inspection of measurable structure factors without detailed knowledge of the scattering properties of the particles can result in severe misinterpretations of structural changes and the underlying interactions.

Although this model for particles with linear SLD gradients is a simplification of the more complex core-shell model from Eq. (2.1) which realistically describes the PMMA-PDMS particles, with this knowledge, the form factor from Fig. 2.3 and $S_M(Q)$ from Fig. 2.5 can be qualitatively assessed. Furthermore, it is demonstrated in **Publication III** that the height of the principal peak of $S_M(Q)$ can only be considered as a representative order parameter within a limited range of contrasts,

particularly for broad size distributions. Therefore, the fact that the amplitude of the main peak of the measurable structure factor in Fig. 2.5 coincides with the peak amplitude of the total structure factor, which truly represents the average structure, is purely caused by a fortuitous combination of the SLDs of the core and the shell, and is not a given general fact.

2.1.4 Collective Short-Time Diffusion

For polydisperse systems, the field correlation function

$$g_1(Q, t) = \frac{S_M(Q, t)}{S_M(Q, 0)} \quad (2.13)$$

accessed in photon correlation spectroscopy experiments, is connected to the measurable intermediate scattering function

$$S_M(Q, t) = \frac{1}{\langle b^2(Q) \rangle} \sum_{\alpha, \beta=1}^n (x_\alpha x_\beta)^{1/2} b_\alpha(Q) b_\beta(Q) S_{\alpha\beta}(Q, t), \quad (2.14)$$

which acts as the dynamical extension of the measurable static structure factor $S_M(Q)$. The experimentally observable short-time behavior of $S_M(Q, t)$ is still characterized by the expansion $S_M(Q, t) = S_M(Q)[1 - D_{\text{eff}}(Q)Q^2t + \mathcal{O}(t^2)]$, however, with a slightly different definition of the effective short-time diffusion coefficient

$$D_{\text{eff}}(Q) = \overline{D_0}(Q) \frac{H_M(Q)}{S_M(Q)} \quad (2.15)$$

where $H_M(Q)$ denotes the measurable hydrodynamic function and

$$\overline{D_0}(Q) = \frac{1}{\langle b^2(Q) \rangle} \sum_{\alpha=1}^n x_\alpha b_\alpha^2(Q) D_{0,\alpha} \quad (2.16)$$

is the Stokes-Einstein diffusion coefficient weighted by the scattering amplitude and averaged over the size distribution. Thus, contrary to the monodisperse case, this apparent diffusion coefficient is a wave-vector-dependent quantity.

In **Publication II**, the effective short-time diffusion coefficient $D_{\text{eff}}(Q)$ is extracted from experimentally obtained field correlation functions. Since both $S_M(Q)$ and $\overline{D_0}(Q)$ can be computed from the parameterized hard-sphere core-shell model introduced previously, this makes the measurable hydrodynamic function $H_M(Q)$ accessible from $D_{\text{eff}}(Q)$. Theoretically, $H_M(Q)$ is, analog to $S_M(Q)$, computable when all partial hydrodynamic functions $H_{\alpha\beta}(Q)$ of a multi-component system are known. Practically however, this turns out to be a highly challenging task and to the present day, no comprehensive theory for hydrodynamic interactions in dense, polydisperse systems has been developed. To avoid a true multi-component

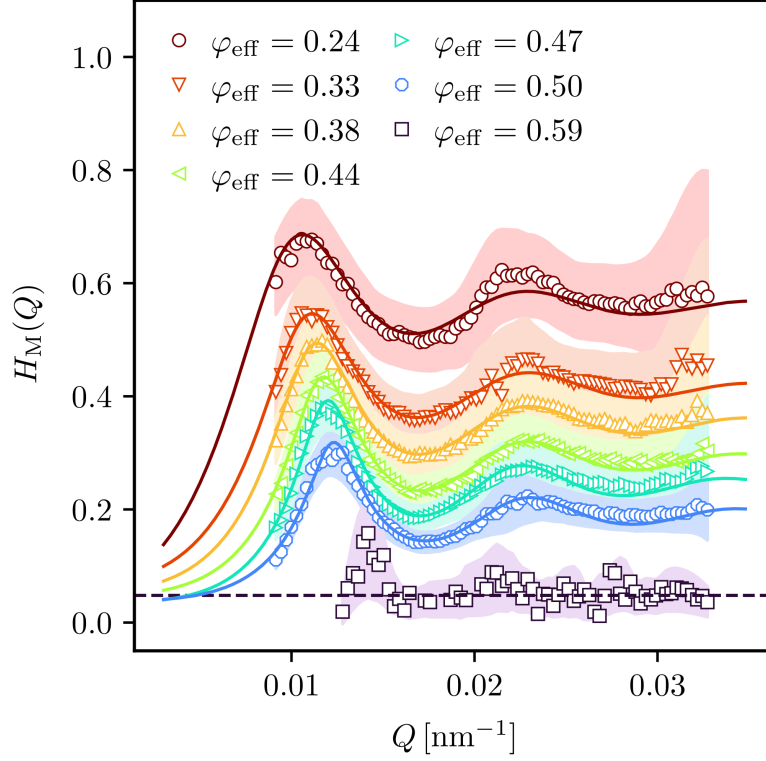


Figure 2.7: Experimentally obtained measurable hydrodynamic functions $H_M(Q)$ for effective hard-sphere volume fractions ranging from $0.24 < \varphi_{\text{eff}} < 0.59$. The solid lines represent the results from the rescaled $\delta\gamma$ -theory. For the glassy sample, the horizontal dashed line is an estimate of the self part of the hydrodynamic function. The shaded regions represent the experimental uncertainties.

treatment of HIs the measurable hydrodynamic function $H_M(Q)$ is modeled within an effective one-component approach by using the well-known, semi-analytical $\delta\gamma$ -scheme proposed by Beenakker and Mazur.^{116,117} Any hydrodynamic function $H(Q)$ can be decomposed in a wave-vector-dependent distinct part and a wave-vector-independent self part according to

$$H(Q) = H_s + H_d(Q) = \frac{D_s}{D_0} + H_d(Q), \quad (2.17)$$

with the self part H_s being equal to the short-time self-diffusion coefficient D_s normalized by D_0 . The distinct part $H_d(Q)$ can be calculated within the $\delta\gamma$ -scheme with knowledge of the static structure factor $S(Q)$ and the particle volume

fraction φ via

$$H_d(x) = \frac{3}{2\pi} \int_0^\infty \left[\frac{\sin x'}{x'} \right] [1 + \varphi S_{\gamma_0}(x')]^{-1} \times \int_{-1}^1 (1 - \mu^2) [S(|\mathbf{x} - \mathbf{x}'|) - 1] d\mu dx', \quad (2.18)$$

Here, $x = 2QR$ is a reduced wave vector with R being the particle radius and $\mu = \hat{\mathbf{x}} \cdot \hat{\mathbf{x}'}$ is the cosine of the angle enclosed by the unit vectors $\hat{\mathbf{x}}$ and $\hat{\mathbf{x}'}$. The calculation of the function $S_{\gamma_0}(x)$ is described by Genz and Klein.¹¹⁸ It is found that a combination of the $\delta\gamma$ -scheme supplied with the average of the partial structure factors $\langle S(Q) \rangle$ for the distinct part and H_s being determined by a least squares fit already gives a quite acceptable, but not a complete quantitative representation of the experimentally obtained hydrodynamic function. This description is improved by introducing two empirical scaling parameters, resulting in

$$H(Q) = H_s + AH_d^{\delta\gamma}(Q^*), \quad (2.19)$$

with $Q^* = \alpha(Q - Q_m) + Q_m$, where A scales the amplitude of the distinct part and α scales the Q -axis about the location of the principal peak Q_m .

Fig. 2.7 shows experimentally determined hydrodynamic functions in an effective hard-sphere volume fraction range of $0.24 < \varphi_{\text{eff}} < 0.59$ alongside the theoretical prediction from the rescaled $\delta\gamma$ -scheme. The experimental data are accurately described for all investigated volume fractions in the liquid-like regime and for the entire accessible wave-vector-range within experimental accuracy, supporting the success of the rescaling approach. In the glassy state with a packing fraction of $\varphi_{\text{eff}} = 0.59$, the hydrodynamic function shows virtually no dependence on the wave vector, except for a small peak that coincides with the maximum of $S_M(Q)$.

2.2 Mode-Coupling Theory for the Quantitative Analysis of Experiments

From both a fundamental and an applied point of view, the quantitative prediction of the dynamics of a system from its structural features is of central importance. Mode-coupling theory (MCT) is a popular theoretical approach for this task, since it enables the computation of dynamic properties in terms of time-dependent correlation functions based only on static, time-independent inputs¹² (see section 1.2.4). As MCT is an approximate method, the simplifications it imposes often prevent a complete quantitative match between the theory's predictions and properties obtained from experiments or computer simulations.⁸² Even though a quantitative accuracy may not be necessary when the objective is to provide fundamental explanations of observed phenomena, predicting the characteristics of a concrete material is crucial in practice for the guided design of complex compounds. In the following sections, it is shown for two specialized applications that by refining existing, well established schemes with comparatively simple modifications previously unfeasible quantitative theoretical descriptions of experimental observations with MCT become possible.

2.2.1 Collective Dynamics and Transport Properties of Model Hard-Sphere Suspensions

In **Publication IV**, the development of a mode-coupling scheme for the quantitative description of the structural relaxation dynamics of the previously examined PMMA-PDMS suspensions is outlined. The characterization of particle morphology, size distribution, static structure and short-time diffusion has been described in detail in the previous sections. Therefore, we can directly state our objective, which is calculating the full time dependence of the measurable intermediate scattering function (ISF) which, as a reminder, is defined by

$$S_M(Q, t) = \frac{\sum_{\alpha, \beta=1}^n (x_\alpha x_\beta)^{1/2} b_\alpha(Q) b_\beta(Q) S_{\alpha\beta}(Q, t)}{\sum_{\alpha=1}^n x_\alpha b_\alpha^2(Q)}. \quad (2.20)$$

Since both the size distribution in terms of the number fractions x_α and all parameters needed to calculate the scattering amplitudes $b_\alpha(Q)$ from the SLD-distribution of the proposed core-shell model [Eq. (2.1)] are known quantities, this task essentially equals finding the time dependence of the matrix of partial ISFs $\mathbf{S}(Q, t)$ with elements $S_{\alpha\beta}(Q, t)$.

The mode-coupling equations which determine the time-dependence of $\mathbf{S}(Q, t)$ for colloidal multi-component systems without hydrodynamic interactions (HIs) read

as⁷⁸

$$\frac{\partial}{\partial t} \mathbf{S}(Q, t) + Q^2 \mathbf{D} \mathbf{S}^{-1}(Q) \mathbf{S}(Q, t) + \mathbf{D} \int_0^t \mathbf{M}(Q, t - t') \frac{\partial}{\partial t'} \mathbf{S}(Q, t') dt' = 0, \quad (2.21)$$

where \mathbf{D} denotes the diagonal matrix of Stokes-Einstein diffusion coefficients and $\mathbf{M}(Q, t)$ is the matrix of irreducible memory functions with elements

$$M_{\alpha\beta}(Q, t) = \frac{1}{16\pi^3(\rho_\alpha\rho_\beta)^{1/2}} \sum_{\gamma\gamma'\delta\delta'} \int V_{\alpha\gamma\delta}(\mathbf{Q}, \mathbf{k}) V_{\beta\gamma'\delta'}(\mathbf{Q}, \mathbf{k}) \times S_{\gamma\gamma'}(k, t) S_{\delta\delta'}(|\mathbf{Q} - \mathbf{k}|, t) d\mathbf{k}. \quad (2.22)$$

The vertices

$$V_{\alpha\gamma\delta}(\mathbf{Q}, \mathbf{k}) = \frac{\mathbf{Q} \cdot \mathbf{k}}{Q} \delta_{\alpha\delta} C_{\alpha\gamma}(k) + \frac{\mathbf{Q} \cdot (\mathbf{Q} - \mathbf{k})}{Q} \delta_{\alpha\gamma} C_{\alpha\delta}(|\mathbf{Q} - \mathbf{k}|) \quad (2.23)$$

are time-independent static functions connected to the density-weighted partial direct correlation functions

$$C_{\alpha\beta}(Q) = (\rho_\alpha\rho_\beta)^{1/2} c_{\alpha\beta}(Q) = \delta_{\alpha\beta} - (S^{-1})_{\alpha\beta}(Q), \quad (2.24)$$

which are determined from the partial structure factors via the multi-component Ornstein-Zernike equation.⁶⁵

Nägele et al.⁷⁸ present a mode-coupling model in which HIs are incorporated both in the short-time expansion of $\mathbf{S}(Q, t)$ and in the memory integral. However, their approach is only valid for dilute dispersions with comparatively large inter-particle distances where HIs can be described by a far-field expansion of the diffusion tensor. For dense systems, where near-field contributions cannot be neglected, the inclusion of HIs in the memory kernel is currently not feasible.

The approach in this work is to neglect the influence of HIs on the memory functions and to simply rescale the time dependence of $\mathbf{S}(Q, t)$ by a dimensionless, effective matrix of hydrodynamic functions with elements

$$[H_{\text{eff}}(Q)]_{\alpha\beta} = \delta_{\alpha\beta} H_s + (x_\alpha x_\beta)^{1/2} H_d(Q). \quad (2.25)$$

This matrix is constructed from the parameterized one-component description of $H_M(Q)$ in Eq. (2.19). The influence of HIs at long times is thus mediated solely through the propagation of these altered initial conditions. The validity of this approach is supported by observations from Medina-Noyola¹¹⁹ and Brady^{120,121}, which state that the influence of HIs on the long-time relaxation for dense hard-sphere systems turns out to be negligible beyond a shift of time scales. Supplied with the correct input, the scheme applied in this form now reproduces the experimentally observed short-time behavior of the measurable ISF $S_M(Q, t)$. In a first

attempt to determine the full time dependence of $\mathbf{S}(Q, t)$, the memory function $\mathbf{M}(Q, t)$ is calculated using the experimentally obtained partial structure factors deduced from the SLS experiments. As apparent from Fig. 2.8, the structural relaxation time is in this case found to be significantly overestimated, especially at the highest investigated number densities. This is expected, since MCT's tendency to overemphasize correlations within the memory function is a widely known limitation of the theory.⁸² To counter this trend, a heuristic modification proposed by Amokrane et al.¹²² is adopted which, in short, is realized by supplying the vertices in the memory kernel [Eq. (2.23)] with direct correlation functions $\mathbf{C}(Q)$ evaluated not at the actual, experimentally observed number density, but rather at a rescaled, effective particle volume fraction. The overestimation of dynamic correlations is thus ad hoc countered by artificially diminishing the structural correlations of the static input. The precise value of this effective volume fraction is determined such that the resulting measurable structure factor $S_M(Q, t)$ best matches the experimental outcome. The results depicted in Fig. 2.8 emphasize the significant improvements invoked by this comparatively simple modification. Within MCT, it is possible to derive transport properties either directly or indirectly from $\mathbf{S}(Q, t)$. For two examples, namely, the shear viscosity η in the low shear rate limit and the long time self-diffusion coefficients $D_{L,\alpha}^s$, it is assessed how well these properties can be predicted based on the parameterized scheme for the collective dynamics without further adjustable parameters. Strikingly, for both properties the MCT predictions excellently match with results from independent experiments, as exemplarily displayed in Fig. 2.9 for the volume fraction dependence of the long time self-diffusion coefficient $D_{L,\alpha}^s$. These observations serve as an important consistency test: It can be conjectured that once a mode-coupling scheme can quantitatively model the collective dynamics of a system, transport properties can be predicted with the same accuracy.

As a significant drawback of the empirical modification, the first-principles character of MCT is lost due to the introduction of an adjustable parameter, which at first glance contradicts the objective of developing theories for the quantitative prediction of experimental results solely from structural inputs. This work is considered as a demonstration of the considerable potential of MCT as a practical method to quantitatively explain experimental findings. Simultaneously, our observations highlight the great demand for substantial theoretical advancements. A systematic improvement of the theory, which would eventually lead MCT to become a tool for the parameter-free, quantitative prediction of dynamical and mechanical material properties, is a challenging endeavor.¹³

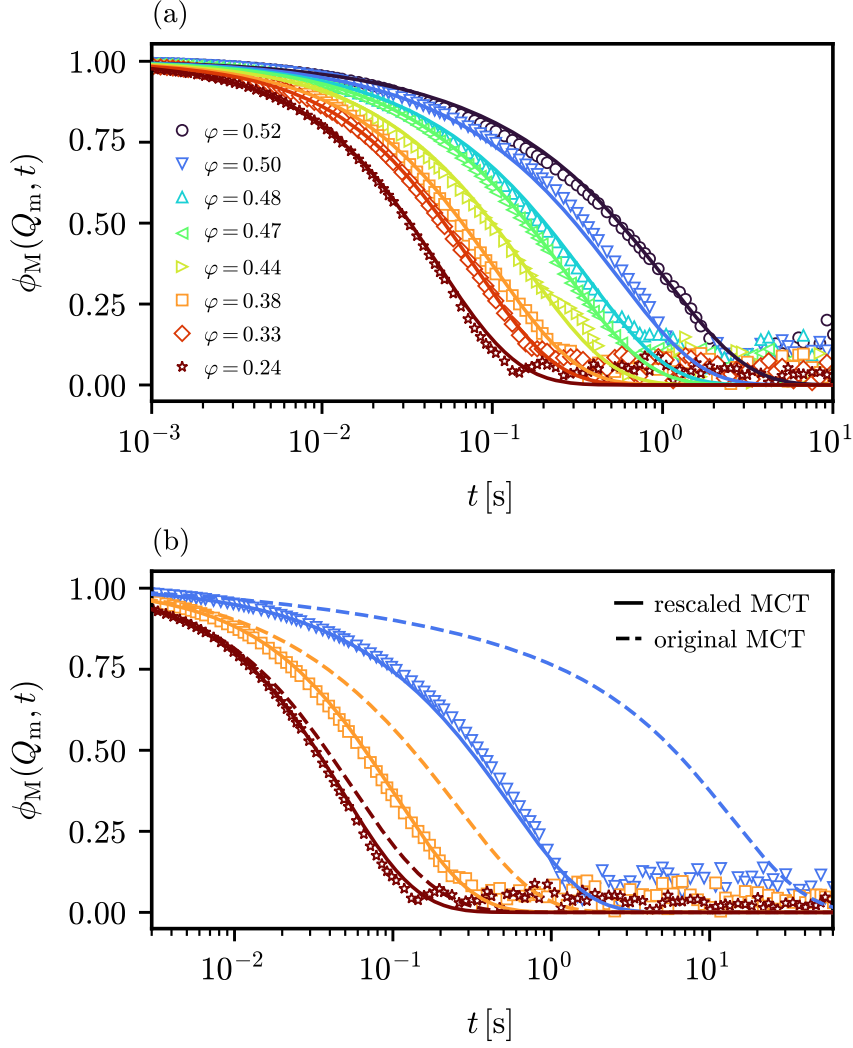


Figure 2.8: (a) Experimentally observed, normalized intermediate scattering function $\phi_M(Q_m, t) = S_M(Q_m, t)/S_M(Q_m)$ in comparison to the results of the rescaled mode-coupling scheme. Q_m is the location of the principal peak of $S_M(Q)$. (b) $\phi_M(Q_m, t)$ calculated with the rescaled volume fractions compared to results from the original MCT for the volume fractions $\varphi = 0.24$, $\varphi = 0.38$ and $\varphi = 0.50$.

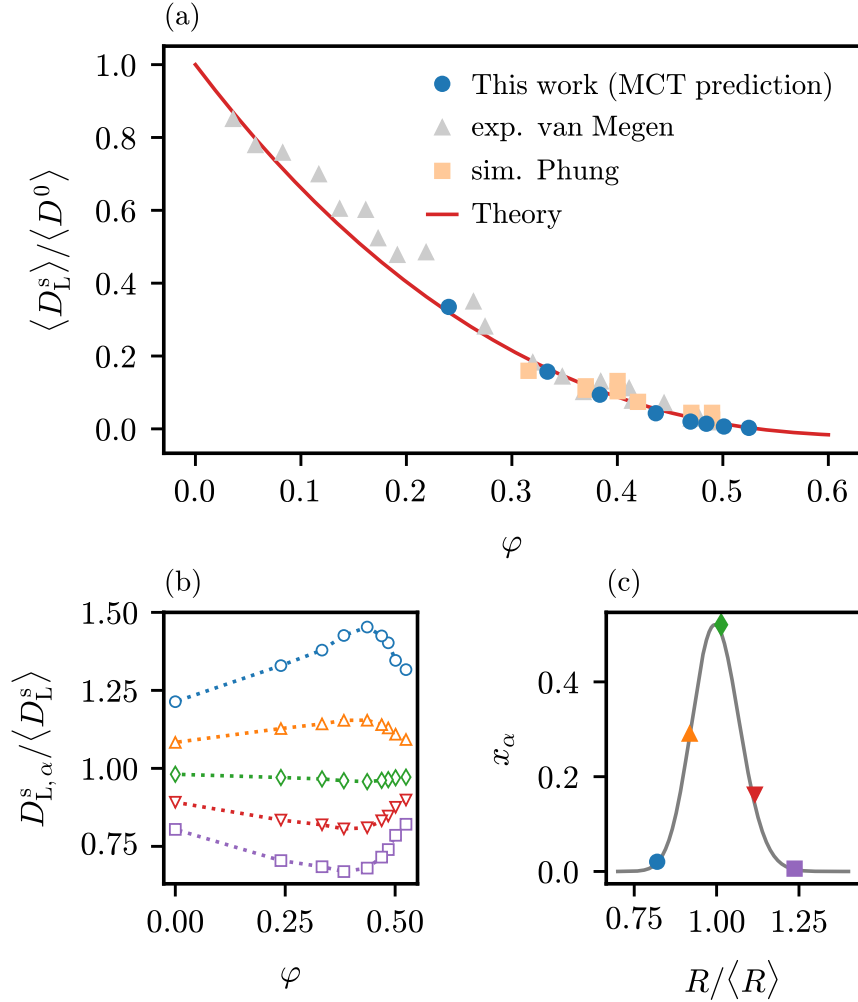


Figure 2.9: (a) Comparison between the average long-time self-diffusion coefficient $\langle D_L^s \rangle$ relative to the average Stokes-Einstein diffusion coefficient $\langle D^0 \rangle$ from the MCT prediction, direct measurements by van Megen and Underwood¹²³ on a similar model system, Stokesian dynamics simulations of a hard spheres by Phung¹²⁴ and a theoretical prediction based on parameterized simulation data¹²⁵ in conjunction with the factorization approximation by Medina-Noyola.¹¹⁹ (b) Normalized long-time self-diffusion coefficients $D_{L,\alpha}^s$ of the individual species of a five-component mixture, representative for the experimentally observed size distribution, in dependence on the volume fraction φ . (c) Distribution of particle radii in relation to the mean, with each symbol in correspondence to (b). The continuous Schulz-Flory distribution, which is approximated by the five-component mixture, is represented by the solid line.

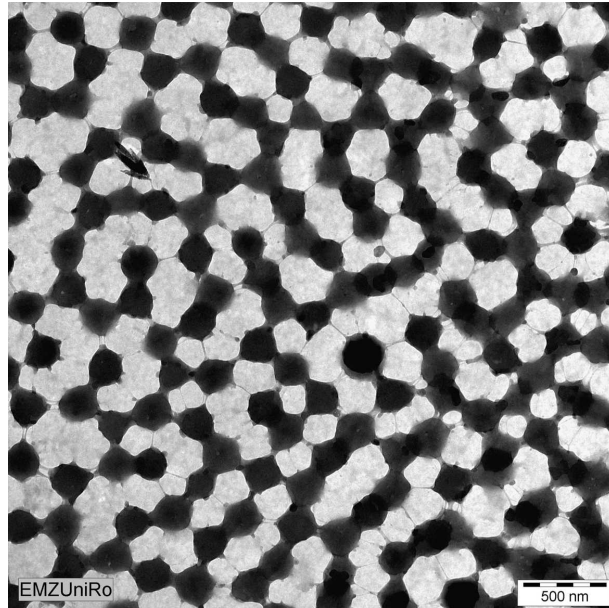


Figure 2.10: Transmission electron micrograph of a pNIPAM-*c*-GA hydrogel. The black spots can be identified as polymer spheres, linked by thin polymer strings. (Reproduced from Nack et al.¹²⁶ with permission of the International Union of Crystallography.)

2.2.2 Schematic Mode-Coupling Model for the Characterization of Viscoelastic Properties of Poly(*N*-isopropylacrylamide) Hydrogels

Stimuli-responsive hydrogels constitute a prominent class of smart materials whose gelation properties can be influenced by precisely tuneable external parameters such as temperature or pH.¹²⁷ Hydrogels based on poly(*N*-isopropylacrylamide) (pNIPAM)¹²⁸ receive wide attention as drug delivery systems or carriers for nanoparticles,^{129–132} due to their lower critical solution temperature (LCST) around 32 °C¹³³ being close to the human body temperature. In our group, pNIPAM hydrogels cross-linked by glutaraldehyde (GA) (short pNIPAM-*c*-GA) were previously employed by Nack et al.¹²⁶ as a viscoelastic matrix for the encapsulation of magnetic hematite particles. The mechanical characterization of the isolated matrix revealed that these materials show many characteristics known from glass-forming materials,^{86,134} such as shear-thinning, strain overshoots in large amplitude oscillatory shear experiments and two separated relaxation modes in the linear viscoelastic frequency spectrum.¹³⁵ Based on an inspection of transmission electron micrographs [Fig. 2.10], it can be assumed that the gel actually consists of spherical polymer particles interconnected by thin polymer strings.

In an effort to gain an advanced understanding of the viscoelastic features of poly(*N*-isopropylacrylamide) cross-linked with glutaraldehyde (pNIPAM-*c*-GA)

hydrogels, the linear and non-linear rheology of these systems is studied in **Publication I**. To quantify the experimental observations in terms of a theoretical model, a schematic mode-coupling scheme is introduced. This model can be regarded as an extension of the $F_{12}^{(\dot{\gamma})}$ -model developed by Fuchs and Cates¹³⁶ who adapted Götze's famous F_{12} -model⁵³ for the description of rheological properties. Frequency-dependent linear viscoelastic moduli $G'(\omega)$ and $G''(\omega)$ and the shear-rate-dependent viscosity $\eta(\dot{\gamma})$ are determined by rheometry for three different hydrogel samples, which share an overall polymer mass fraction of 10 % but differ in the cross-linker content used during synthesis. The cross-linking ratio $\chi = n_{\text{GA}}/(n_{\text{GA}} + n_{\text{NIPAM}})$ is quantified by the amount of GA relative to the total monomer amount and the three investigated cross-linking ratios in this work are $\chi = 0.025$, $\chi = 0.05$ and $\chi = 0.1$. A set of experimentally obtained moduli and viscosities for the three cross-linking ratios is displayed in Fig. 2.11. It is found that Fuchs and Cates' $F_{12}^{(\dot{\gamma})}$ -model is not able to accurately describe the experimentally found frequency- and shear-rate-dependence. In short, this is due to a limitation already present in the original F_{12} -model (see section 1.2.4), namely, that the critical Debye-Waller factor f_c within the model cannot be varied independently of the exponent parameter λ , as both are connected via the constraint $f_c = 1 - \lambda$. The F_{12} -scheme, which determines the time evolution of an arbitrary correlator $\Phi(t)$ via

$$\frac{1}{\Gamma} \frac{\partial}{\partial t} \Phi(t) + \Phi(t) + \int_0^t m(t-t') \frac{\partial}{\partial t'} \Phi(t') dt' = 0, \quad (2.26)$$

with the expansion $m(t) = v_1 \Phi(t) + v_2 \Phi^2(t)$, depends besides the initial relaxation rate Γ on the two vertex coefficients v_1 and v_2 . However, the model can also be parameterized in a physically more appealing picture by exploiting the connection between the vertices, the exponent parameter λ and a separation parameter ε , which determines the deviation of the Debye-Waller factor f from its critical value f_c in the vicinity of the glass transition via

$$\lim_{\varepsilon \rightarrow 0^+} f(\varepsilon) = f_c + (1 - f_c)^2 \sqrt{\frac{\varepsilon}{1 - \lambda}} + \mathcal{O}(\varepsilon). \quad (2.27)$$

ε serves as a general measure for the distance from a given state to the glass transition. A commonly employed parameterization is then fixing $v_2 = 1/\lambda^2$ while letting $v_1 = (2\lambda - 1)/\lambda^2 + \varepsilon\lambda/(1 - \lambda)$ be determined by both λ and ε . Fuchs and Cates' extension¹³⁶ for sheared systems is the introduction of the auxiliary function

$$h(t) = \left[1 + \left(\frac{\dot{\gamma}}{\dot{\gamma}_c} \Gamma t \right)^2 \right]^{-1}, \quad (2.28)$$

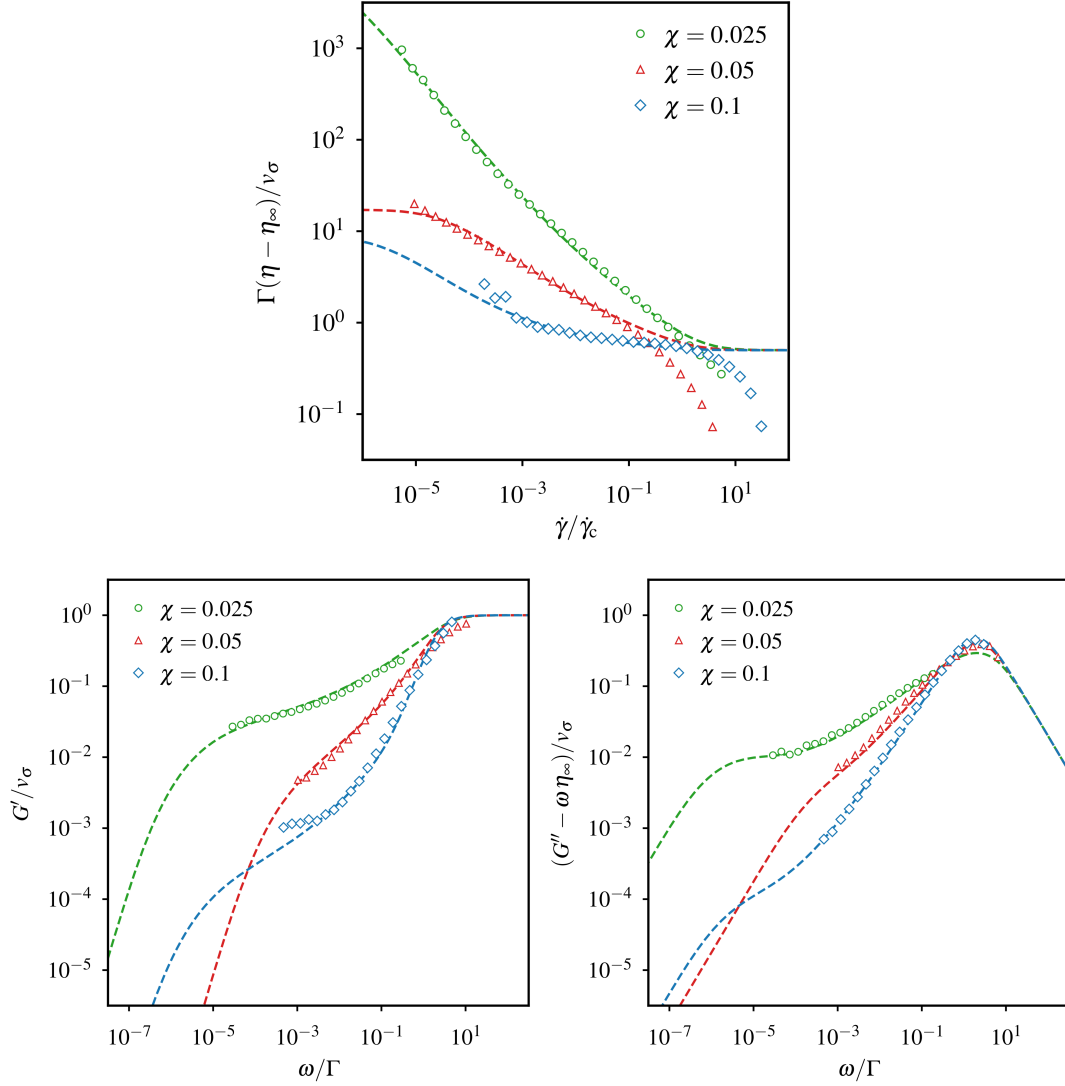


Figure 2.11: Dimensionless viscosity $\Gamma(\eta - \eta_\infty)/v_\sigma$ as a function of the dimensionless shear rate $\dot{\gamma}/\dot{\gamma}_c$ and dimensionless storage modulus G'/v_σ and loss modulus $(G'' - \omega\eta_\infty)/v_\sigma$ as a function of the dimensionless angular frequency ω/Γ , all for the three cross-linking ratios $\chi = 0.025$, $\chi = 0.05$ and $\chi = 0.1$ at a constant temperature of 20 °C. Γ is the initial relaxation rate of the correlator $\Phi(t)$, η_∞ is the viscosity at infinite shear rate and γ_c and v_σ are heuristic parameters which respectively determine the absolute magnitude of the shear rate and the stress.

which depends on the shear rate $\dot{\gamma}$ and an empirical parameter $\dot{\gamma}_c$. The memory equation for $\Phi(t)$ then reads

$$\frac{1}{\Gamma}\dot{\Phi}(t) + \Phi(t) + h(t) \int_0^t M(t-t') \dot{\Phi}(t') dt' = 0 \quad (2.29)$$

with $M(t) = h(t)m(t)$. The moduli $G'(\omega)$ and $G''(\omega)$ and the viscosity $\eta(\dot{\gamma})$ can be derived from $\Phi(t)$ via a Green-Kubo relation,^{137,138} as detailed in **Publication I**. It is found that the critical constraint $f_c = 1 - \lambda$ can be lifted if instead of Eq. (2.29), the set of coupled equations,

$$\frac{1}{\alpha\Gamma}\dot{\Phi}_0(t) + \Phi_0(t) + h(t) \int_0^t M_0(t-t') \dot{\Phi}_0(t') dt' = 0 \quad (2.30a)$$

$$\frac{1}{\Gamma}\dot{\Phi}(t) + \Phi(t) + h(t) \int_0^t \alpha M_0(t-t') \dot{\Phi}(t') dt' = 0, \quad (2.30b)$$

is employed for determining $\Phi(t)$, with $M_0(t) = h(t)[v_1\Phi_0(t) + v_2\Phi_0^2(t)]$. Within this rescaled scheme, the vertices v_1 and v_2 are still defined in terms of the exponent parameter λ and the separation parameter ε , but additionally, a third parameter

$$\alpha = \frac{\lambda}{1-\lambda} \frac{f_c}{1-f_c}, \quad (2.31)$$

provides the flexibility that allows f_c to be varied independently of λ . This is illustrated in Fig. 2.12, where exemplarily, $\Phi(t)$, $G'(\omega)$ and $G''(\omega)$ are compared for multiple values of f_c . Moreover, the parameterization of the scheme in terms of the separation parameter ε is contrasted with an alternative parameterization in terms of a reduced separation parameter $\varepsilon^* = \alpha^2\varepsilon$, which emerges naturally when an equivalent to Eq. (2.27) is re-derived for the modified model.

Fig. 2.11 displays least-squares fits of the rescaled $F_{12}^{(\dot{\gamma})}$ -model to the experimentally obtained viscosities and linear viscoelastic moduli. Within experimental accuracy, the rescaled schematic model quantitatively matches the observations, with the exception of $\eta(\dot{\gamma})$ at the highest strain rates, where the model predicts the onset of a Newtonian plateau while in reality, the viscosity decreases even further, most likely due to a secondary relaxation process which cannot be explained solely by the shear-induced destruction of nearest-neighbor cages responsible for the primary shear thinning. The visualized data is presented in terms of reduced coordinates such that the physics between samples with different cross-linking ratios χ can be compared separate from obvious changes in absolute amplitudes and time scales. Thus, the curves in Fig. 2.11 depend precisely on three parameters, the exponent parameter λ , the reduced separation parameter ε^* and the critical Debye-Waller

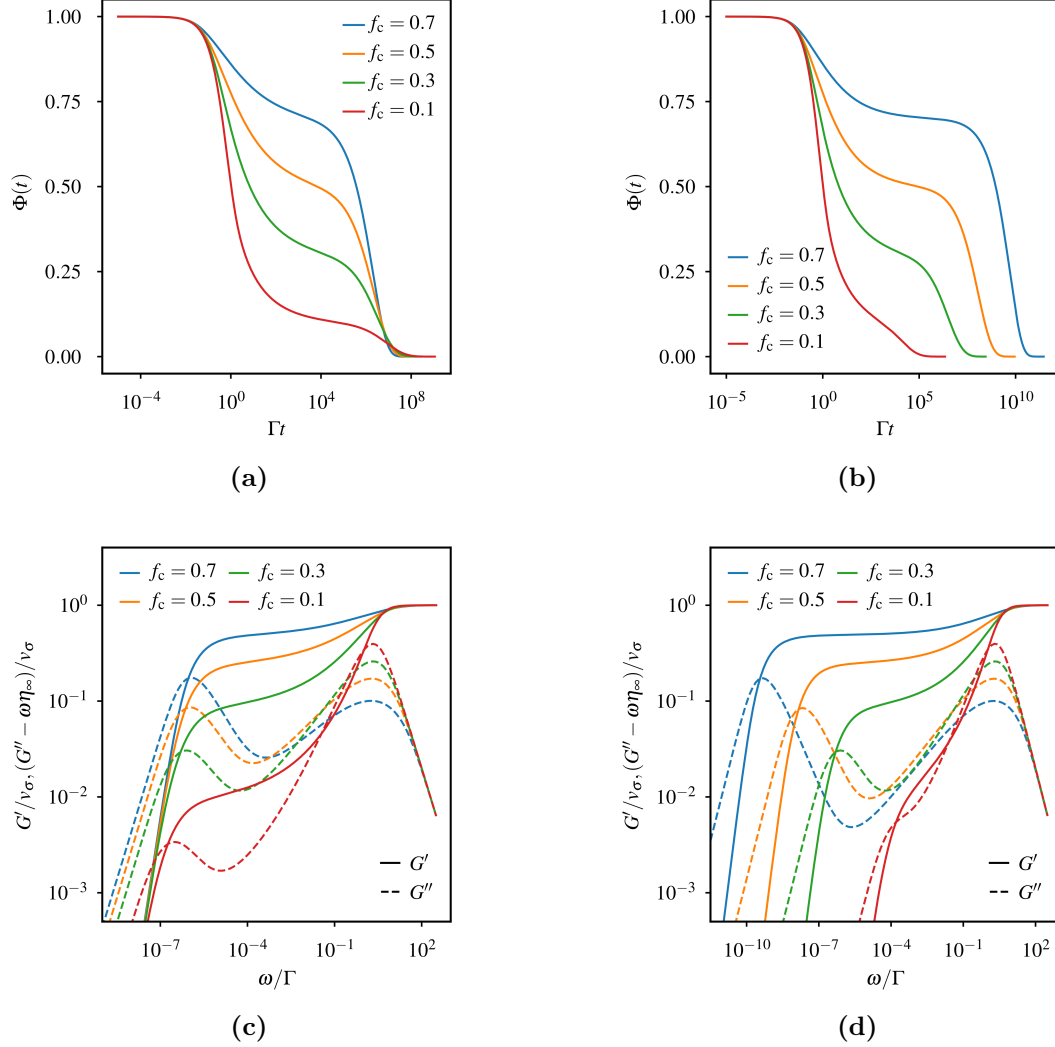


Figure 2.12: Influence of the critical Debye-Waller factor f_c on the correlation functions $\Phi(t)$ and the complex moduli $G'(\omega)$ and $G''(\omega)$ resulting from the rescaled $F_{12}^{(\dot{\gamma})}$ -model at either constant separation parameter ε or constant reduced separation parameter $\varepsilon^* = \alpha^2 \varepsilon$ and all for the exponent parameter $\lambda = 0.7$. While at constant ε only the height of the plateau is influenced, the α -relaxation time increases consistently with the plateau height if instead ε^* is held constant.

- (a) $\Phi(t)$ with $\varepsilon = -1 \times 10^{-3}$
- (b) $\Phi(t)$ with $\varepsilon^* = -1 \times 10^{-3}$
- (c) $G^*(\omega)$ with $\varepsilon = -1 \times 10^{-3}$
- (d) $G^*(\omega)$ with $\varepsilon^* = -1 \times 10^{-3}$

factor f_c . As a surprising observation, all differences caused by changing cross-linking ratios can be fully explained by variation of the critical Debye-Waller factor f_c , while both λ and ε^* are almost unaffected by changes in χ . Physically, the magnitude of the Debye-Waller factor is connected to the mobility of a particle inside its nearest neighbor cage, with f_c being lower the more freely a particle's position can fluctuate inside the cage. Based on this picture, it is astonishing that an increased degree of cross-linking causes a decrease of f_c , against the intuitive expectation that more cross-linking should inhibit movement instead of facilitating it. To explain this behavior, a more detailed investigation of the gel's mesostructure is required.

3 Perspective

The results of this thesis motivate future investigations in several directions. Regarding the PDMS-PMMA colloids, the mechanisms of the compression of the PDMS shell at high volume fractions demand further attention. To resolve this effect in more detail, investigating particles with a larger shell-to-core ratio is a good approach. This can be achieved either by preparing smaller particles with the same stabilizer or by using stabilizers with a higher molecular weight. Smaller particles would require the switch to small-angle X-ray or neutron scattering³⁸ to adequately resolve structural features. To probe inter-particle forces in a controlled fashion on a single particle level, direct-force-probing techniques like optical tweezers¹³⁹ or colloidal probe atomic force microscopy¹⁴⁰ are adequate methods. Laser light scattering on dense systems using a standard goniometer setup is largely limited to refractive-index-matched dispersions. Emerging modulated 3D cross-correlation techniques¹⁴¹ allow the characterization of turbid systems by overcoming multiple scattering without sacrificing a high amount of speckle contrast. An interesting complement to DLS is dynamic differential microscopy (DDM),^{142,143} which allows probing the dynamics of large ensembles of particles using a light microscopy setup, also for relatively turbid samples.

From a theoretical standpoint, a major obstacle in the MCT analysis of the PDMS-PMMA suspensions is the accurate treatment of hydrodynamics. Clearly, more effort to develop analytic frameworks for HIs in dense, multi-component systems is necessary. Another option is switching to model systems where HIs in polydisperse samples are more easy to handle, for example, dilute, highly charged colloids where multi-component theory on the well-studied Rotne-Prager level¹⁴⁴ is still applicable. Clearly however, then, a simplified description of HIs is traded for more complex potential interactions, with currently no accurate analytic expression for partial structure factors available.

The concept of empirically modified mode-coupling schemes can also be developed further. Inspiration can be taken from the process of developing closures for the Ornstein-Zernike relation, where it is common to approximate bridge functions in an empirical fashion.¹⁴⁵ The method from Amokrane et al.¹²² in this sense bears resemblance to the rescaled mean spherical approximation for Yukawa systems¹⁴⁶ or the Verlet-Weis correction for hard-sphere Percus-Yevick structure factors.¹⁴⁷ Another interesting research direction inspired by findings of this thesis could be further studying diffusion in correlated, continuously polydisperse systems. While most effort is concentrated on the investigation of monodisperse suspensions or binary mixtures, systems with continuous and purposely broad size distributions are gaining importance in the context of glass-forming liquids, where they are conjectured to give access to deeply supercooled states not reachable with simpler particle mixtures.^{148–150}

Follow-up studies regarding the pNIPAM-hydrogels could encompass a detailed structure analysis by means of SANS¹⁵¹ and direct imaging via cryo-EM.¹⁵² For a further mechanical characterization of these systems, microrheological investigations of the local viscoelasticity inside the network could provide promising insights, best realized with a combination of passive techniques based on, e.g., diffusing wave spectroscopy^{153,154} and active friction probing via optical tweezers.¹⁵⁵ Also interesting would be the development of theoretically more tractable and experimentally more controllable gel-forming colloidal model systems. This could be realized by considering dispersions with combined short-range attractive and long-range repulsive interactions¹⁵⁶ or possibly using colloids with highly controllable network forming capabilities via DNA-like surface functionalizations.¹⁵⁷

References

- [1] J. Diaz Maier and J. Wagner, *J. Chem. Phys.* **157**, 114901 (2022).
- [2] J. Diaz Maier and J. Wagner, *Soft Matter* **20**, 1309 (2024).
- [3] J. Diaz Maier, K. Gaus, and J. Wagner, *J. Appl. Crystallogr.* **57**, 1503 (2024).
- [4] J. Diaz Maier and J. Wagner, *Phys. Rev. E* **109**, 064605 (2024).
- [5] P. G. de Gennes, *Rev. Mod. Phys.* **64**, 645 (1992).
- [6] B. A. Grzybowski, C. E. Wilmer, J. Kim, K. P. Browne, and K. J. M. Bishop, *Soft Matter* **5**, 1110 (2009).
- [7] D. Fritz, K. Koschke, V. A. Harmandaris, N. F. A. van der Vegt, and K. Kremer, *Phys. Chem. Chem. Phys.* **13**, 10412 (2011).
- [8] J. van der Gucht, *Front. Phys.* **6** (2018).
- [9] W. M. Jacobs, A. Reinhardt, and D. Frenkel, *Proc. Natl. Acad. Sci.* **112**, 6313 (2015).
- [10] G. Schneider and K.-H. Baringhaus, *Molecular Design: Concepts and Applications* (John Wiley & Sons, Feb. 26, 2008), 284 pp.
- [11] A. Yethiraj, *Soft Matter* **3**, 1099 (2007).
- [12] L. M. C. Janssen, *Front. Phys.* **6** (2018).
- [13] I. Pihlajamaa, C. C. L. Laudicina, and L. M. C. Janssen, *Phys. Rev. Res.* **5**, 033120 (2023).
- [14] J. F. Morris, *Rheol. Acta* **48**, 909 (2009).
- [15] D. Babič, C. Schmitt, and C. Bechinger, *Chaos* **15**, 026114 (2005).
- [16] C. P. Royall, W. C. K. Poon, and E. R. Weeks, *Soft Matter* **9**, 17 (2012).
- [17] X. Ye, T. Narayanan, P. Tong, J. S. Huang, M. Y. Lin, B. L. Carvalho, and L. J. Fetters, *Phys. Rev. E* **54**, 6500 (1996).
- [18] D. Frenkel, *Science* **314**, 768 (2006).
- [19] G. Nägele, *Phys. Rep.* **272**, 215 (1996).
- [20] A. Yethiraj and A. van Blaaderen, *Nature* **421**, 513 (2003).
- [21] M. Klokkenburg, R. P. A. Dullens, W. K. Kegel, B. H. Ern e, and A. P. Philipse, *Phys. Rev. Lett.* **96**, 037203 (2006).
- [22] J.-W. Kim, R. J. Larsen, and D. A. Weitz, *J. Am. Chem. Soc.* **128**, 14374 (2006).

- [23] S. Sacanna and D. J. Pine, *Curr. Opin. Colloid Interface Sci.* **16**, 96 (2011).
- [24] S. Sacanna, D. J. Pine, and G.-R. Yi, *Soft Matter* **9**, 8096 (2013).
- [25] V. Rao Dugyala, S. V. Daware, and M. G. Basavaraj, *Soft Matter* **9**, 6711 (2013).
- [26] H. R. Vutukuri, B. Bet, R. van Roij, M. Dijkstra, and W. T. S. Huck, *Sci. Rep.* **7**, 16758 (2017).
- [27] W. Wang, X. Lv, J. L. Moran, S. Duan, and C. Zhou, *Soft Matter* **16**, 3846 (2020).
- [28] B. Liebchen and H. Löwen, *J. Chem. Phys.* **150**, 061102 (2019).
- [29] A. Walther and A. H. E. Müller, *Soft Matter* **4**, 663 (2008).
- [30] J. Hu, S. Zhou, Y. Sun, X. Fang, and L. Wu, *Chem. Soc. Rev.* **41**, 4356 (2012).
- [31] A. Walther and A. H. E. Müller, *Chem. Rev.* **113**, 5194 (2013).
- [32] M. E. McConney, S. Singamaneni, and V. V. Tsukruk, *Polym. Rev.* **50**, 235 (2010).
- [33] F. Giavazzi and R. Cerbino, *J. Opt.* **16**, 083001 (2014).
- [34] M. C. Jenkins and S. U. Egelhaaf, *Adv. Colloid Interface Sci.* **136**, 65 (2008).
- [35] C. P. Royall, A. A. Louis, and H. Tanaka, *J. Chem. Phys.* **127**, 044507 (2007).
- [36] V. Prasad, D. Semwogerere, and E. R. Weeks, *J. Phys.: Condens. Matter* **19**, 113102 (2007).
- [37] J. Watt, D. L. Huber, and P. L. Stewart, *MRS Bull.* **44**, 942 (2019).
- [38] T. Li, A. J. Senesi, and B. Lee, *Chem. Rev.* **116**, 11128 (2016).
- [39] D. Lehner, G. Kellner, H. Schnablegger, and O. Glatter, *J. Colloid Interface Sci.* **201**, 34 (1998).
- [40] S. Mobilio, F. Boscherini, and C. Meneghini, eds., *Synchrotron Radiation: Basics, Methods and Applications* (Springer, Berlin, Heidelberg, 2015).
- [41] B. J. Berne and R. Pecora, *Dynamic Light Scattering: With Applications to Chemistry, Biology and Physics* (Dover Publications, Mineola, New York, 1976).
- [42] P. A. Hassan, S. Rana, and G. Verma, *Langmuir* **31**, 3 (2015).
- [43] O. G. Shpyrko, *J. Synchrotron Radiat.* **21**, 1057 (2014).
- [44] O. Glatter, ed., *Scattering Methods and their Application in Colloid and Interface Science* (Elsevier, Jan. 1, 2018).

-
- [45] Z. Sun, C. D. Tomlin, and E. M. Sevick-Muraca, *Langmuir* **17**, 6142 (2001).
- [46] J. S. Pedersen, *Adv. Colloid Interface Sci.* **70**, 171 (1997).
- [47] F. Carsughi, *Appl. Sci.* **12**, 10677 (2022).
- [48] R. Botet, S. Kwok, and B. Cabane, *J. Appl. Cryst.* **53**, 1570 (2020).
- [49] I. Breßler, J. Kohlbrecher, and A. F. Thünemann, *J. Appl. Cryst.* **48**, 1587 (2015).
- [50] E. I. Kats and A. R. Muratov, *Phys. Rev. E* **97**, 012610 (2018).
- [51] P. Español and H. Löwen, *J. Chem. Phys.* **131**, 244101 (2009).
- [52] M. Haataja, L. Gránásy, and H. Löwen, *J. Phys.: Condens. Matter* **22**, 360301 (2010).
- [53] W. Götze, *Z. Phys. B: Condens. Matter* **56**, 139 (1984).
- [54] D. R. Reichman and P. Charbonneau, *J. Stat. Mech.* **2005**, P05013 (2005).
- [55] L. Yeomans-Reyna and M. Medina-Noyola, *Phys. Rev. E* **64**, 066114 (2001).
- [56] M. A. Chávez-Rojo and M. Medina-Noyola, *Phys. Rev. E* **72**, 031107 (2005).
- [57] L. F. Elizondo-Aguilera and Th. Voigtmann, *Phys. Rev. E* **100**, 042601 (2019).
- [58] W. Demtröder, *Experimentalphysik 1: Mechanik und Wärme*, Springer-Lehrbuch (Springer, Berlin, Heidelberg, 2015).
- [59] D. T. Chen, Q. Wen, P. A. Janmey, J. C. Crocker, and A. G. Yodh, *Annu. Rev. Condens. Matter Phys.* **1**, 301 (2010).
- [60] N. J. Wagner and J. Mewis, eds., *Theory and Applications of Colloidal Suspension Rheology*, Cambridge Series in Chemical Engineering (Cambridge University Press, Cambridge, 2021).
- [61] J. C. Maxwell, *Philos. Trans. R. Soc. Lond.* **155**, 459 (1865).
- [62] C. Huygens, *Traité de la lumière* (chez Pierre vander Aa, marchand libraire, Leiden, 1690), book.
- [63] M. Born, *Z. Physik* **37**, 863 (1926).
- [64] J.-P. Hansen, D. Levesque, and J. Zinn-Justin, *Liquids, Freezing and Glass Transition* (North Holland, 1991), 536 pp.
- [65] J.-P. Hansen and I. R. McDonald, eds., *Theory of Simple Liquids* (Academic Press, Oxford, Jan. 1, 2013).
- [66] L. S. Ornstein and F. Zernike, *Proc. Akad. Sci.* **17**, 793 (1914).
- [67] J. K. Percus and G. J. Yevick, *Phys. Rev.* **110**, 1 (1958).
- [68] A. Vrij, *J. Chem. Phys.* **69**, 1742 (1978).

- [69] A. Vrij, *J. Chem. Phys.* **71**, 3267 (1979).
- [70] L. Blum and G. Stell, *J. Chem. Phys.* **71**, 42 (1979).
- [71] L. Blum and G. Stell, *J. Chem. Phys.* **72**, 2212 (1980).
- [72] A. J. F. Siegert, *On the Fluctuations in Signals Returned by Many Independently Moving Scatterers* (Radiation Laboratory, Massachusetts Institute of Technology, 1943), 28 pp.
- [73] R. G. W. Brown, *Appl. Opt.*, AO **26**, 4846 (1987).
- [74] G. Nägele and P. Baur, *Phys. A* **245**, 297 (1997).
- [75] P. G. De Gennes, *Physica* **25**, 825 (1959).
- [76] U. Bengtzelius, W. Gotze, and A. Sjolander, *J. Phys. C: Solid State Phys.* **17**, 5915 (1984).
- [77] G. Szamel and H. Löwen, *Phys. Rev. A* **44**, 8215 (1991).
- [78] G. Nägele, J. Bergenholtz, and J. K. G. Dhont, *J. Chem. Phys.* **110**, 7037 (1999).
- [79] W. Götze, *J. Phys.: Condens. Matter* **11**, A1 (1999).
- [80] W. Götze, *Z. Phys. B: Condens. Matter* **60**, 195 (1985).
- [81] J. C. Phillips, *Rep. Prog. Phys.* **59**, 1133 (1996).
- [82] S. P. Das, *Rev. Mod. Phys.* **76**, 785 (2004).
- [83] V. Krakoviack and C. Alba-Simionesco, *J. Chem. Phys.* **117**, 2161 (2002).
- [84] J. J. Crassous, M. Siebenbürger, M. Ballauff, M. Drechsler, D. Hajnal, O. Henrich, and M. Fuchs, *J. Chem. Phys.* **128**, 204902 (2008).
- [85] M. Siebenbürger, M. Fuchs, H. Winter, and M. Ballauff, *J. Rheol.* **53**, 707 (2009).
- [86] J. M. Brader, M. Siebenbürger, M. Ballauff, K. Reinheimer, M. Wilhelm, S. J. Frey, F. Weysser, and M. Fuchs, *Phys. Rev. E* **82**, 061401 (2010).
- [87] M. Domschke, M. Marsilius, T. Blochowicz, and T. Voigtmann, *Phys. Rev. E* **84**, 031506 (2011).
- [88] D. Hajnal and M. Fuchs, *Eur. Phys. J. E* **28**, 125 (2009).
- [89] G. Nägele and J. Bergenholtz, *J. Chem. Phys.* **108**, 9893 (1998).
- [90] G. Nägele and J. K. G. Dhont, *J. Chem. Phys.* **108**, 9566 (1998).
- [91] M. Fuchs and M. E. Cates, *Phys. Rev. Lett.* **89**, 248304 (2002).
- [92] M. Fuchs and M. E. Cates, *J. Phys.: Condens. Matter* **17**, S1681 (2005).
- [93] L. Antl, J. W. Goodwin, R. D. Hill, R. H. Ottewill, S. M. Owens, S. Papworth, and J. A. Waters, *Colloids Surf.* **17**, 67 (1986).

-
- [94] M. T. Elsesser and A. D. Hollingsworth, *Langmuir* **26**, 17989 (2010).
- [95] L. Palangetic, K. Feldman, R. Schaller, R. Kalt, W. R. Caseri, and J. Vermant, *Faraday Discuss.* **191**, 325 (2016).
- [96] J. E. Hallett, I. Grillo, and G. N. Smith, *Langmuir* **36**, 2071 (2020).
- [97] R. H. Pelton, A. Osterroth, and M. A. Brook, *J. Colloid Interface Sci.* **137**, 120 (1990).
- [98] R. Pelton, A. Osterroth, and M. A. Brook, *J. Colloid Interface Sci.* **147**, 523 (1991).
- [99] S. M. Klein, V. N. Manoharan, D. J. Pine, and F. F. Lange, *Colloid Polym. Sci.* **282**, 7 (2003).
- [100] A. P. Richez, L. Farrand, M. Goulding, J. H. Wilson, S. Lawson, S. Biggs, and O. J. Cayre, *Langmuir* **30**, 1220 (2014).
- [101] S. Kawaguchi and K. Ito, in *Polymer Particles*, edited by M. Okubo, *Advances in Polymer Science* (Springer, Berlin, Heidelberg, 2005), pp. 299–328.
- [102] B. Derjaguin, *Kolloid-Z.* **69**, 155 (1934).
- [103] J. G. Kirkwood and E. M. Boggs, *J. Chem. Phys.* **10**, 394 (1942).
- [104] B. Widom, *Science* **157**, 375 (1967).
- [105] C. P. Royall, M. E. Leunissen, A.-P. Hynninen, M. Dijkstra, and A. van Blaaderen, *J. Chem. Phys.* **124**, 244706 (2006).
- [106] S. Kale, A. Lederer, M. Oettel, and H. J. Schöpe, *Soft Matter* **19**, 2146 (2023).
- [107] S.-E. Phan, W. B. Russel, Z. Cheng, J. Zhu, P. M. Chaikin, J. H. Dunsmuir, and R. H. Ottewill, *Phys. Rev. E* **54**, 6633 (1996).
- [108] W. B. Russel, P. M. Chaikin, J. Zhu, W. V. Meyer, and R. Rogers, *Langmuir* **13**, 3871 (1997).
- [109] G. V. Schulz, *Z. Phys. Chem.* **43B**, 25 (1939).
- [110] P. J. Flory, *J. Am. Chem. Soc.* **58**, 1877 (1936).
- [111] P. Bartlett and R. H. Ottewill, *J. Chem. Phys.* **96**, 3306 (1992).
- [112] B. D’Aguanno and R. Klein, *Phys. Rev. A* **46**, 7652 (1992).
- [113] F. W. J. Olver, ed., *NIST Handbook of Mathematical Functions Paperback and CD-ROM* (Cambridge University Press, May 17, 2010), 968 pp.
- [114] F. Sciortino, S. Mossa, E. Zaccarelli, and P. Tartaglia, *Phys. Rev. Lett.* **93**, 055701 (2004).
- [115] Y. Liu, W.-R. Chen, and S.-H. Chen, *J. Chem. Phys.* **122**, 044507 (2005).

- [116] C. W. J. Beenakker and P. Mazur, *Phys. A* **120**, 388 (1983).
- [117] C. W. J. Beenakker and P. Mazur, *Phys. A* **126**, 349 (1984).
- [118] U. Genz and R. Klein, *Phys. A* **171**, 26 (1991).
- [119] M. Medina-Noyola, *Phys. Rev. Lett.* **60**, 2705 (1988).
- [120] J. F. Brady, *J. Chem. Phys.* **99**, 567 (1993).
- [121] J. F. Brady, *J. Fluid Mech.* **272**, 109 (1994).
- [122] S. Amokrane, F. Tchangnwa Nya, and J. M. Ndjaka, *Eur. Phys. J. E* **40**, 17 (2017).
- [123] W. van Meegen and S. M. Underwood, *J. Chem. Phys.* **91**, 552 (1989).
- [124] T. N. Phung, “Behavior of concentrated colloidal suspensions by Stokesian dynamics simulation”, PhD thesis (California Institute of Technology, 1993).
- [125] J. Riest, T. Eckert, W. Richtering, and G. Nägele, *Soft Matter* **11**, 2821 (2015).
- [126] A. Nack, J. Seifert, C. Passow, and J. Wagner, *J. Appl. Cryst.* **51**, 87 (2018).
- [127] L. Klouda and A. G. Mikos, *Eur. J. Pharm. Biopharm., Interactive Polymers for Pharmaceutical and Biomedical Applications* **68**, 34 (2008).
- [128] H. G. Schild, *Prog. Polym. Sci.* **17**, 163 (1992).
- [129] X. Xu, Y. Liu, W. Fu, M. Yao, Z. Ding, J. Xuan, D. Li, S. Wang, Y. Xia, and M. Cao, *Polymers* **12**, 580 (2020).
- [130] M. Cao, Y. Wang, X. Hu, H. Gong, R. Li, H. Cox, J. Zhang, T. A. Waigh, H. Xu, and J. R. Lu, *Biomacromolecules* **20**, 3601 (2019).
- [131] T. Yadavalli, S. Ramasamy, G. Chandrasekaran, I. Michael, H. A. Therese, and R. Chennakesavulu, *J. Magn. Magn. Mater., 10th International Conference on the Scientific and Clinical Applications of Magnetic Carriers 10-14 June, 2014, Dresden, Germany* **380**, 315 (2015).
- [132] H. Kim, A. Jo, S. Baek, D. Lim, S.-Y. Park, S. K. Cho, J. W. Chung, and J. Yoon, *Sci. Rep.* **7**, 41090 (2017).
- [133] M. Heskins and J. E. Guillet, *J. Macromol. Sci., Chem.* **2**, 1441 (1968).
- [134] T. Voigtmann, M. Siebenbürger, C. P. Amann, S. U. Egelhaaf, S. Fritschi, M. Krüger, M. Laurati, K. J. Mutch, and K. H. Samwer, *Colloid Polym. Sci.* **298**, 681 (2020).
- [135] A. Nack, “Particle-matrix interactions in ferrogels containing shape-anisotropic, magnetic nanoparticles”, PhD thesis (Universität Rostock, 2017).
- [136] M. Fuchs and M. E. Cates, *Faraday Discuss.* **123**, 267 (2003).

-
- [137] J. M. Brader, Th. Voigtmann, M. E. Cates, and M. Fuchs, *Phys. Rev. Lett.* **98**, 058301 (2007).
- [138] J. M. Brader, M. E. Cates, and M. Fuchs, *Phys. Rev. Lett.* **101**, 138301 (2008).
- [139] C. Zhang, J. Muñetón Díaz, A. Muster, D. R. Abujetas, L. S. Froufe-Pérez, and F. Scheffold, *Nat. Commun.* **15**, 1020 (2024).
- [140] F. J. Montes Ruiz-Cabello, G. Trefalt, P. Maroni, and M. Borkovec, *Phys. Rev. E* **90**, 012301 (2014).
- [141] I. D. Block and F. Scheffold, *Rev. Sci. Instrum.* **81**, 123107 (2010).
- [142] R. Cerbino and V. Trappe, *Phys. Rev. Lett.* **100**, 188102 (2008).
- [143] X. Zhang, J. Fu, Z. Zhang, M. Jangda, C. Rosu, G. D. B. Parkinson, and P. S. Russo, *Macromolecules* **57**, 3 (2024).
- [144] M. G. McPhie and G. Nägele, *J. Chem. Phys.* **127**, 034906 (2007).
- [145] F. Lucco Castello and P. Tolias, *Phys. Rev. E* **105**, 015208 (2022).
- [146] J.-P. Hansen and J. B. Hayter, *Mol. Phys.* **46**, 651 (1982).
- [147] L. Verlet and J.-J. Weis, *Phys. Rev. A* **5**, 939 (1972).
- [148] A. Ninarello, L. Berthier, and D. Coslovich, *Phys. Rev. X* **7**, 021039 (2017).
- [149] I. Pihlajamaa, V. E. Debets, C. C. L. Laudicina, and L. M. C. Janssen, *SciPost Phys.* **15**, 217 (2023).
- [150] C. C. L. Laudicina, I. Pihlajamaa, and L. M. C. Janssen, *Phys. Rev. Res.* **5**, 033121 (2023).
- [151] E. M. Saffer, M. A. Lackey, D. M. Griffin, S. Kishore, G. N. Tew, and S. R. Bhatia, *Soft Matter* **10**, 1905 (2014).
- [152] C. Marmorat, A. Arinstein, N. Koifman, Y. Talmon, E. Zussman, and M. Rafailovich, *Sci. Rep.* **6**, 25495 (2016).
- [153] A. Palmer, T. G. Mason, J. Xu, S. C. Kuo, and D. Wirtz, *Biophys. J.* **76**, 1063 (1999).
- [154] M. Alexander, I. Piska, and D. G. Dalgleish, *Food Hydrocolloids* **22**, 1124 (2008).
- [155] J. Caspers, N. Ditz, K. Krishna Kumar, F. Ginot, C. Bechinger, M. Fuchs, and M. Krüger, *J. Chem. Phys.* **158**, 024901 (2023).
- [156] J. C. F. Toledano, F. Sciortino, and E. Zaccarelli, *Soft Matter* **5**, 2390 (2009).
- [157] L. Di Michele, F. Varrato, J. Kotar, S. H. Nathan, G. Foffi, and E. Eiser, *Nat. Commun.* **4**, 2007 (2013).

Publication I

Viscoelastic properties of pNIPAM-hydrogels: A mode-coupling theory study

J. Diaz Maier and J. Wagner

J. Chem. Phys. **157**, 114901 (2022)

<https://doi.org/10.1063/5.0097841>

Reprinted from J. Diaz Maier and J. Wagner, J. Chem. Phys. **157**, 114901 (2022), with the permission of AIP Publishing.

Contribution:

I conceptualized this work together with J.W. I performed the experiments, implemented software for the curation of measurement data, devised and implemented the extension to the schematic mode-coupling model, performed fits, analyzed the results and wrote the original draft. The manuscript was revised together with J.W.

My approximated contribution to the publication in percent: 90 %

Viscoelastic properties of pNIPAM-hydrogels: A mode-coupling theory study

Cite as: J. Chem. Phys. 157, 114901 (2022); doi: 10.1063/5.0097841

Submitted: 2 May 2022 • Accepted: 23 June 2022 •

Published Online: 15 September 2022



View Online



Export Citation



CrossMark

Joel Diaz Maier  and Joachim Wagner^{a)} 

AFFILIATIONS

Institut für Chemie, Universität Rostock, 18051 Rostock, Germany

Note: This paper is part of the JCP Special Topic on Colloidal Gels.

^{a)} Author to whom correspondence should be addressed: joachim.wagner@uni-rostock.de.

URL: <https://www.wagner.chemie.uni-rostock.de>

ABSTRACT

We investigate the viscoelastic properties of poly(*N*-isopropylacrylamide) (pNIPAM) hydrogels cross-linked with glutaraldehyde by means of small amplitude oscillatory and steady shear experiments in dependence on the frequency and shear rate. These properties are strongly influenced by the ratio of monomer and glutaraldehyde as a cross-linker. Due to the thermosensitivity of pNIPAM, the rheological properties of these hydrogels can be tuned by the temperature as an external stimulus. The experimentally obtained viscosities and linear viscoelastic moduli are analyzed by a schematic mode-coupling ansatz employing a rescaled F_{12} -model.

Published under an exclusive license by AIP Publishing. <https://doi.org/10.1063/5.0097841>

I. INTRODUCTION

During the last decades, hydrogels as smart materials have attracted large scientific interest both from the viewpoint of fundamental science and as a result of their manifold applications from the viewpoint of engineering. Due to their nonergodicity, hydrogels are attractive model systems for the investigation of structure-dynamics relations in soft matter.¹ Hydrogels as hydrophilic polymer networks are capable of incorporating large amounts of water and, thus, are, in principle, biocompatible.² Caused by their biocompatibility, hydrogels are promising smart materials for biomedical applications,³ drug delivery,^{4–6} and biosensors.⁷

Stimuli-responsive hydrogels whose properties can be tuned by parameters such as pH or temperature^{8,9} are not only for applications but also for fundamental research of special interest: The mesoscale structure and dynamics can gradually be influenced by these precisely tunable parameters. The most prominent thermoresponsive hydrogel is poly(*N*-isopropylacrylamide) (pNIPAM)¹⁰ with a lower critical solution temperature $T_{LCST} = 304$ K close to ambient temperature.¹¹

Colloidal suspensions as highly defined model systems essentially contributed to the theoretical understanding of structure-dynamics relations in nonergodic systems. Structure and diffusive motion in both hard-sphere-like model systems consisting of

PMMA^{12,13} and charged Yukawa systems^{14–16} have exhaustively been studied. The theoretical understanding of dynamical processes in strongly interacting colloidal systems is substantially founded on mode-coupling theory (MCT).^{17–19} Later on, the use of MCT for the prediction of rheological properties of nonergodic systems has been established.^{20–24} Stimulated by these theoretical advances, the nonlinear flow behavior of colloidal glasses has been investigated experimentally.^{25–27}

The viscoelastic behavior of pNIPAM hydrogels cross-linked with glutaraldehyde has previously been described.^{28,29} Opposite to a cross-linking by means of a copolymer, where permanent links connect polymer chains, by the reaction of glutaraldehyde with the secondary amine functionalities of *N*-isopropylacrylamide (NIPAM), hemiaminals are formed. The formation of hemiaminals with secondary amines that cannot condense to imines in a second reaction step is reversible in aqueous media and, thus, leads to a fluctuating network of cross-linked microgels.

The aim of this contribution is a systematic investigation of the frequency- and shear-rate dependent flow behavior of cross-linked pNIPAM hydrogels and its analysis by an MCT approach. Schematic MCT approaches such as the F_{12} model introduced by Götze¹⁸ reproduce the essential relaxation behavior without *a priori* knowledge of the structure factor $S(Q)$ and, thus, are widely used to describe rheological properties of viscoelastic systems. However,

the classical F_{12} -model fails to describe the rheological properties consistently for all cross-linking ratios. Rescaled F_{12} -models³⁰ successfully have been used to describe slow dynamic processes in glass forming liquids studied by means of quasielastic scattering methods^{31–34} and dielectric spectroscopy.³⁵ In this paper, we apply a rescaled F_{12} -model to describe the rheological behavior of hydrogels with different content of cross-linkers.

II. THEORETICAL BACKGROUND

A. Mode-coupling theory

Mode-coupling theory (MCT) provides a first-principles approach for the prediction of the relaxation dynamics of glass-forming liquids. Employing a projection-operator formalism,^{36–39} the time evolution of the autocorrelation function of wave-vector-dependent density fluctuations $\Phi(Q, t)$ can be described via a Mori-Zwanzig equation, which for colloidal systems in the overdamped limit¹⁹ can be expressed as

$$\frac{1}{\Gamma(Q)} \dot{\Phi}(Q, t) + \Phi(Q, t) + \int_0^t m(Q, t-t') \dot{\Phi}(Q, t') dt' = 0. \quad (1)$$

Within the mode-coupling approximation,¹⁷ the memory kernel $m(Q, t)$ is related to the number density ρ and the static structure factor $S(Q)$. The short-time dynamics is expanded in a series $\Phi(Q, t) = 1 - \Gamma(Q)t + \mathcal{O}(t^2)$ with the relaxation rate $\Gamma(Q)$ as initial slope.

Schematic, wave-vector-independent models aim to capture the phenomenology of the full MCT equations utilizing a simplified memory kernel. An established model is the F_{12} -model proposed by Götze,¹⁸

$$\frac{1}{\Gamma} \dot{\Phi}(t) + \Phi(t) + \int_0^t m(t-t') \dot{\Phi}(t') dt' = 0, \quad (2)$$

with the expansion $m(t) = v_1\Phi(t) + v_2\Phi^2(t)$ for the memory function. The vertices v_1 and v_2 of the memory kernel and the initial relaxation rate Γ are adjustable parameters of this model.

For sufficiently small vertices, $\Phi(t)$ decays to zero displaying a two-step relaxation process in resemblance to the dynamics of supercooled liquids, while at a critical value, a bifurcation of the long-time limit occurs. In the latter case, a single decay onto a nonzero plateau, called β -process, remains, while the long-time dynamics, i.e., the α -process is frustrated as typical for the glassy state. The long-time limit of the density correlation function $f = \Phi(t \rightarrow \infty)$ is the non-ergodicity parameter or Debye-Waller factor.

Within the F_{12} -model, the critical vertices are related by $v_1^c = (2\lambda - 1)/\lambda^2$ and $v_2^c = 1/\lambda^2$ to the exponent parameter λ , leading to the critical Debye-Waller factor $f_c = 1 - \lambda$ within $1/2 \leq \lambda < 1$.^{18,40}

For nonergodic systems, the approach and departure from the plateau f_c can be described by the universal power laws $\Phi(t) \sim f_c + At^{-a}$ and $\Phi(t) \sim f_c - Bt^b$, where the exponents a and b are related to the exponent parameter λ via the relation,

$$\lambda = \frac{\Gamma(1-a)^2}{\Gamma(1-2a)} = \frac{\Gamma(1+b)^2}{\Gamma(1+2b)}, \quad (3)$$

with $\Gamma(x)$ denoting the gamma function.⁴¹

The distance to the glass transition can be quantified by a separation parameter ε , which satisfies the relation,

$$\lim_{\varepsilon \rightarrow 0^+} f(\varepsilon) = f_c + (1 - f_c)^2 \sqrt{\frac{\varepsilon}{1-\lambda}} + \mathcal{O}(\varepsilon), \quad (4)$$

describing the deviation of the Debye-Waller factor f from the critical Debye-Waller factor f_c in the glassy state. Within the F_{12} -model, the separation parameter is related to the critical vertices by $\varepsilon = (\delta v_1 f_c + \delta v_2 f_c^2)/(1 - f_c)$ with $v_i = v_i^c + \delta v_i$. Choosing $\delta v_2 = 0$ leads to $v_2 = v_2^c = 1/\lambda^2$ depending only on the exponent parameter λ .^{25,42–44} The vertex $v_1 = (2\lambda - 1)/\lambda^2 + \varepsilon\lambda/(1 - \lambda)$ depends on the separation parameter ε and the exponent parameter $\lambda = 1 - f_c$ in this case.

B. MCT in external shear flow

Integration through transients (ITT) is a widely used approach to extend MCT to systems underlying a shear flow.^{20,21} Applying this formalism to the F_{12} -model leads to

$$\frac{1}{\Gamma} \dot{\Phi}(t) + \Phi(t) + h(t) \int_0^t M(t-t') \dot{\Phi}(t') dt' = 0, \quad (5)$$

in the case of steady-state rheology. Utilizing the auxiliary function,

$$h(t) = \left[1 + \left(\frac{\dot{\gamma}}{\dot{\gamma}_c} \Gamma t \right)^2 \right]^{-1}, \quad (6)$$

which is related to the reduced shear rate $\dot{\gamma}/\dot{\gamma}_c$, the memory function reads as $M(t) = h(t)m(t)$. Here, $\dot{\gamma}$ is the shear rate, and the critical shear rate $\dot{\gamma}_c$ is an additional adjustable parameter of the F_{12} -model for sheared systems. Note that in the limit $\dot{\gamma} \rightarrow 0$, the expression for the quiescent F_{12} -model is recovered.

Within schematic MCT, the generalized shear modulus reads with the stress vertex v_σ and the high-frequency viscosity η_∞ as

$$G(t) = v_\sigma \Phi^2(t) + \eta_\infty \delta(t), \quad (7)$$

where the latter quantity η_∞ accounts for hydrodynamic interactions not included in the idealized MCT. The time-dependent shear stress $\sigma(t)$ for a given shear rate $\dot{\gamma}(t)$ is accessible via a generalized, nonlinear Green-Kubo relation,^{45,46}

$$\sigma(t) = \int_{-\infty}^t \dot{\gamma}(t') G(t-t') dt'. \quad (8)$$

Starting from this expression,

$$\eta = \frac{\sigma}{\dot{\gamma}} = \int_0^\infty v_\sigma \Phi^2(t) dt + \eta_\infty, \quad (9)$$

is obtained for the shear viscosity.

In the case of oscillatory shear experiments, a periodic shear strain $\gamma(t) = \gamma_0 \sin(\omega t)$ with the amplitude of deformation γ_0 results. To consider a frequency- and deformation-dependent phase shift between stress and strain, a two-time correlation function $G(t, t')$ is required due to the time-translational variance of the shear flow.²⁷ In the limit of small amplitudes $\gamma_0 \ll 1$, however, with a

trivial phase relation between stress and strain, the two-time correlation function depends in good approximation only on the time difference $t - t'$ and, thus, can be replaced by the time correlation function $G(t - t')$ as defined in Eq. (7).

The frequency-dependent complex modulus $G(\omega)$ is the Fourier transform of the time-dependent modulus,

$$G(\omega) = G'(\omega) + iG''(\omega) = i\omega \int_0^{\infty} G(t) e^{-i\omega t} dt, \quad (10)$$

which leads to expressions for the storage modulus $G'(\omega)$ and the loss modulus $G''(\omega)$ in terms of the respective sine and cosine transformations,

$$G'(\omega) = \omega \int_0^{\infty} v_{\sigma} \Phi^2(t) \sin \omega t dt, \quad (11a)$$

$$G''(\omega) = \omega \int_0^{\infty} v_{\sigma} \Phi^2(t) \cos \omega t dt + \omega \eta_{\infty}. \quad (11b)$$

III. RESCALED F_{12} -MODEL IN SHEARED SYSTEMS

The discussed F_{12} -model has been proven to accurately describe the phenomenology of glass forming liquids, despite its relative simplicity.^{25–27} There is, however, the well-known constraint that the exponent parameter λ and the critical Debye–Waller factor f_c cannot be varied independently of each other, leading, for example, to the inability to describe processes where a change of f_c at constant λ is assumed. As such, it is preferable to extend the accessible parameter domain by lifting the constraint $f_c = 1 - \lambda$.

The approach in this paper is to calculate an effective correlation function from a rescaled F_{12} -model, which is similar to a class of models previously used.^{47–49} For clarity, the modification of the quiescent equilibrium model is discussed first. After that, the approach is generalized to account for steady-state shear, which can also be applied for oscillatory shear experiments in the linear viscoelastic regime.

Starting from the regular F_{12} -model,

$$\frac{1}{\Gamma_0} \dot{\Phi}_0(t) + \Phi_0(t) + \int_0^t m_0(t-t') \dot{\Phi}_0(t') dt' = 0, \quad (12)$$

with $m_0(t) = v_1 \Phi_0(t) + v_2 \Phi_0^2(t)$, an initial correlation function $\Phi_0(t)$ can be obtained. Using this initial correlation function $\Phi_0(t)$, a rescaled correlation function $\Phi_1(t)$ is obtained by introducing a scaling parameter α . In the rescaled F_{12} -model, the memory kernel reads as $m_1(t) = \alpha m_0(t)$, leading to

$$\frac{1}{\Gamma_1} \dot{\Phi}_1(t) + \Phi_1(t) + \int_0^t \alpha m_0(t-t') \dot{\Phi}_1(t') dt' = 0, \quad (13)$$

where time-invariance is preserved by choosing $\Gamma_1 = \Gamma_0/\alpha$. The long-time limit of the memory function at the bifurcation transition reads within the rescaled F_{12} -model as

$$\lim_{t \rightarrow \infty} m_{1,c}(t) = \frac{f_{1,c}}{1-f_{1,c}} = \alpha \frac{f_{0,c}}{1-f_{0,c}} = \alpha \frac{1-\lambda}{\lambda}. \quad (14)$$

Obviously, with $\alpha = 1$ the original F_{12} -model is recovered as a special case. In the following, for ease of notation, the subscript 1 for the quantities referring to the rescaled schematic model is omitted.

The modification leads to the introduction of a factor α into Eq. (4), yielding the expression,

$$\lim_{\varepsilon \rightarrow 0^+} f(\varepsilon) = f_c + (1-f_c)^2 \alpha \sqrt{\frac{\varepsilon}{1-\lambda}} + \mathcal{O}(\varepsilon). \quad (15)$$

This result can be obtained by rewriting Eq. (4) in terms of the long-time limit of the memory function $m(t \rightarrow \infty) = f/(1-f)$, and multiplying all memory functions with a factor α . With the reduced separation parameter $\varepsilon^* = \alpha^2 \varepsilon$, an expression formally identical to Eq. (4) is obtained. Since the exponent parameter λ is independent of α , the exponents a and b from Eq. (3) are preserved and all scaling relations only involving λ are identical to the original F_{12} -model.

The MCT equations are numerically solved using common methods.^{50,51} Within the rescaled F_{12} -model, as exemplarily shown in Fig. 1 with exponent parameter $\lambda = 0.7$ and separation parameter $\varepsilon = -10^{-3}$, tunable critical Debye–Waller factors f_c can be obtained. Keeping λ and ε constant, both, α - and β -relaxation times are preserved. Keeping instead λ and the reduced separation parameter ε^* constant, the α -relaxation time is changed by the critical Debye–Waller factor f_c (Fig. 2): Increasing critical Debye–Waller factors f_c lead to enlarged α -relaxation times.

From this point, the extension to sheared systems is straightforward. Again introducing the auxiliary function $h(t)$ [Eq. (6)], the set of equations,

$$\frac{1}{\alpha\Gamma} \dot{\Phi}_0(t) + \Phi_0(t) + h(t) \int_0^t M_0(t-t') \dot{\Phi}_0(t') dt' = 0, \quad (16a)$$

$$\frac{1}{\Gamma} \dot{\Phi}(t) + \Phi(t) + h(t) \int_0^t \alpha M_0(t-t') \dot{\Phi}(t') dt' = 0, \quad (16b)$$

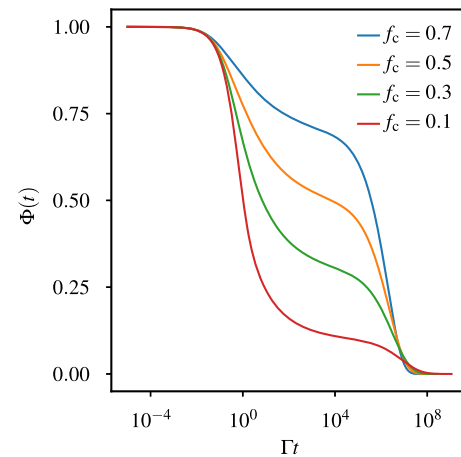


FIG. 1. Correlation functions $\Phi(t)$ resulting from the rescaled schematic model [Eq. (13)] for selected critical Debye–Waller factors f_c at constant exponent parameter $\lambda = 0.7$ and separation parameter $\varepsilon = -1 \times 10^{-3}$. The function with $f_c = 1 - \lambda = 0.3$ corresponds to the original F_{12} -model [Eq. (2)].

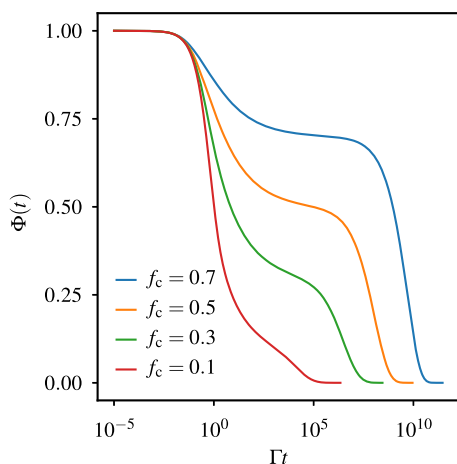


FIG. 2. Correlation functions resulting from the rescaled schematic model [Eq. (13)] for selected critical Debye–Waller factors f_c at constant exponent parameter $\lambda = 0.7$ and reduced separation parameter $\varepsilon^* = \alpha^2 \varepsilon = -1 \times 10^{-3}$. The function with $f_c = 1 - \lambda = 0.3$ corresponds to the original F_{12} -model [Eq. (2)].

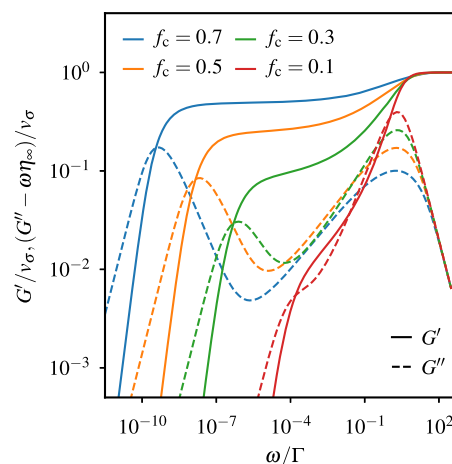


FIG. 4. Frequency-dependent storage modulus G' (solid lines) and loss modulus G'' (dashed lines) resulting from the rescaled schematic model [Eq. (13)] for selected critical Debye–Waller factors f_c at constant exponent parameter $\lambda = 0.7$ and reduced separation parameter $\varepsilon^* = \alpha^2 \varepsilon = -1 \times 10^{-3}$. The functions with $f_c = 1 - \lambda = 0.3$ correspond to the original F_{12} -model [Eq. (2)].

with $M_0(t) = h(t)m_0(t)$ is obtained.

Storage and loss moduli $G'(\omega)$ and $G''(\omega)$ resulting from the rescaled F_{12} -model at constant exponent parameter $\lambda = 0.7$ are displayed in Figs. 3 and 4. In Fig. 3, a constant separation parameter $\varepsilon = -10^{-3}$ is used, while in Fig. 4, a constant reduced separation parameter $\varepsilon^* = -10^{-3}$ is assumed.

As expected from the correlation functions in Figs. 1 and 2, where the β -relaxation time is not influenced by the critical Debye–Waller factor f_c , the maximum of the high-frequency loss peak associated with the β -process is independent of the frequency ω . At constant separation parameter ε , the α -relaxation

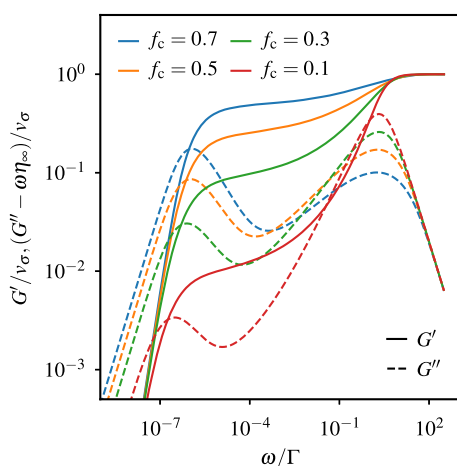


FIG. 3. Frequency-dependent storage modulus G' (solid lines) and loss modulus G'' (dashed lines) resulting from the rescaled schematic model [Eq. (13)] for selected critical Debye–Waller factors f_c at constant exponent parameter $\lambda = 0.7$ and separation parameter $\varepsilon = -1 \times 10^{-3}$. The functions with $f_c = 1 - \lambda = 0.3$ correspond to the original F_{12} -model [Eq. (2)].

time related to the low-frequency loss peak is practically independent of f_c and, thus, the maximum of the low-frequency loss peak is nearly frequency-independent. Opposite, when the α -relaxation time depends on the critical Debye–Waller factor at constant reduced separation parameter ε^* , the low-frequency loss peak's maximum strongly depends on the frequency. The plateau of the storage modulus increases with the critical Debye–Waller factor f_c as well as the low-frequency loss peak's amplitude. In contrast, the high-frequency loss peak's amplitude decreases with rising f_c .

IV. EXPERIMENTAL

A. Sample preparation

Poly(*N*-isopropylacrylamide) (pNIPAM) hydrogels are synthesized via emulsion polymerization of *N*-isopropylacrylamide (NIPAM) in the presence of glutaraldehyde (GA) as a cross-linking agent, as described in Ref. 28. By the addition of GA, a network of interconnected spherical polymer particles is obtained,⁵² as visible in TEM micrographs.²⁸ By variation of the molar ratio of NIPAM and GA during synthesis, the cross-linking ratio,

$$\chi = \frac{n_{\text{GA}}}{n_{\text{GA}} + n_{\text{NIPAM}}}, \quad (17)$$

can be adjusted. In this paper, hydrogels with three different cross-linking ratios $\chi = 0.025$, $\chi = 0.05$ and $\chi = 0.1$ are investigated. After synthesis, the gels were purified by dialysis against deionized water for at least one week and concentrated to a volume of around 100 ml via vacuum evaporation. The polymer mass fraction w was determined gravimetrically. Subsequently, the water content of each hydrogel was adjusted by dilution with deionized water to obtain a final polymer mass fraction of $w = 0.1$. Since the mass density of pNIPAM is approximately identical to that of the majority compound water, the mass fraction w is practically identical to the

volume fraction ϕ . To ensure homogeneity, the samples, after stirring, were left for at least one week for equilibration before any experiment.

B. Rheology

Rheological experiments were performed using an MCR 302 Rheometer (Anton Paar) in cone-plate geometry with a cone diameter of $d = 25$ mm. For the least viscous gel with cross-linking ratio $\chi = 0.1$, a cone with a diameter of $d = 50$ mm was used to increase the torque sensitivity. Employing a PT 100 sensor for temperature control in the center of the bottom plate, combined with a Peltier hood to minimize solvent evaporation, a temperature stability better than $\Delta T = \pm 0.05$ K was achieved. The less viscous hydrogel samples with cross-linking ratios $\chi = 0.1$ and $\chi = 0.05$ were applied to the bottom plate using a pipette with an enlarged tip, while samples with $\chi = 0.025$ had to be loaded with help of a spatula. To erase loading history and to ensure sample homogeneity, all gels were subjected to rotational shear with a shear rate of $\dot{\gamma} = 100$ s⁻¹ until the monitored viscosity remained constant. Prior to any experiment, each sample was pre-sheared with a shear rate of $\dot{\gamma} = 100$ s⁻¹ for 60 s followed by a resting period of 5 min. Experiments were conducted for each sample at four temperatures in a range between $\vartheta = 10$ °C and $\vartheta = 25$ °C. Frequency sweeps from $\omega = 100$ rad s⁻¹ to $\omega = 0.01$ rad s⁻¹ were performed to probe the linear viscoelastic response of the hydrogels. The optimal strain amplitude γ_0 was determined from preliminary tests for each sample and was fixed to $\gamma_0 = 0.05$ for $\chi = 0.1$, whereas $\gamma_0 = 0.01$ was used for gels with smaller cross-linking ratios. The steady-state viscosity η was measured for shear rates $1000 \geq \dot{\gamma} \geq 0.001$ s⁻¹.

V. RESULTS AND DISCUSSION

Storage moduli $G'(\omega)$ and loss moduli $G''(\omega)$ from frequency sweeps and the dynamic viscosity $\eta(\dot{\gamma})$ from flow curve measurements were determined for three different cross-linking ratios at

four temperatures each. For each cross-linking ratio χ , the model [Eqs. (16)] discussed in Sec. III is fitted to the experimental data at all temperatures simultaneously using an unweighted least-squares fit algorithm employing the following constraints: The exponent parameter λ was determined from preliminary fits and was fixed to a value of $\lambda = 0.815$ for the actual fits. This is above the value calculated for hard sphere suspensions^{53,54} of $\lambda \approx 0.76$, where the dynamic arrest is governed by packing effects. Values higher than that are typical for systems where different mechanisms for dynamic arrest compete with each other,⁵⁵ like in systems with attractive short range interactions,^{56,57} or asymmetric binary mixtures.⁵⁸ The critical Debye–Waller factor f_c and the stress vertex v_σ are assumed only to depend on the cross-linking ratio but not on the temperature. The remaining parameters, the separation parameter ε , the relaxation rate Γ , the critical shear rate $\dot{\gamma}_c$, and the high frequency viscosity η_∞ are fitted without constraints. The optimum fit parameters are compiled in Table I. For the largest cross-linking ratio $\chi = 0.1$, the separation parameter ε could not reliably be determined because the separation parameter mostly influences the α -relaxation, which occurs for this specific sample at frequencies below the experimentally observable frequency range. Opposite, for the sample with the lowest cross-linking ratio $\chi = 0.025$ the high-frequency limit η_∞ could not reliably be determined, since for this sample hydrodynamic effects become important at frequencies beyond the experimentally accessible frequency range. Experimentally determined moduli and viscosities for all investigated temperatures together with fits employing the rescaled F_{12} -model are displayed in the [supplementary material](#) (Sec. S-I).

A. Viscosity and viscoelastic moduli

The measured frequency-dependent linear viscoelastic response of the hydrogels is exemplarily shown in Fig. 5 for all three cross-linking ratios. All samples show behavior typical for glass forming liquids and both, the elastic, and the viscous response can be described well with the rescaled F_{12} -model over nearly the

TABLE I. Optimum fit parameters and uncertainties resulting from the rescaled, schematic model [Eq. (16)] used to describe viscoelastic moduli and viscosity for three cross-linking ratios χ at four different temperatures ϑ .

χ	ϑ [°C]	λ	f_c	$\varepsilon \times 10^3$	$\varepsilon^* \times 10^3$	Γ [s ⁻¹]	v_σ [Pa]	$\dot{\gamma}_c$ [s ⁻¹]	η_∞ [Pa s]
0.025	10	0.815 ^a	0.169(6)	-3.02(22)	-2.4(4)	200(40)	1390(120)	74(16)	N/A ^b
	15			-2.10(18)	-1.69(29)	260(50)		125(26)	
	20			-1.81(16)	-1.45(26)	350(60)		180(40)	
	25			-1.28(12)	-1.03(19)	500(90)		510(100)	
0.050	10	0.815 ^a	0.0575(15)	-15.9(11)	-1.15(15)	5.7(4)	53.7(23)	53(10)	1.27(10)
	15			-16.3(10)	-1.18(14)	7.5(6)		78(15)	1.01(9)
	20			-14.1(8)	-1.02(12)	9.7(8)		107(20)	0.78(8)
	25			-6.7(5)	-0.48(7)	12.4(10)		340(50)	0.60(7)
0.100	10	0.815 ^a	0.0134(5)	N/A ^c	N/A	11.0(7)	4.72(27)	4.4(18)	0.446(19)
	15					15.5(9)		4.0(11)	0.363(15)
	20					21.2(13)		5.2(13)	0.288(11)
	25					31.0(19)		2.5(6)	0.252(9)

^aFixed value determined from preliminary fits.

^bSet to $\eta_\infty = 0$ Pa s in the respective plots.

^cSet to $\varepsilon = -5 \times 10^{-3}$ in the respective plots.

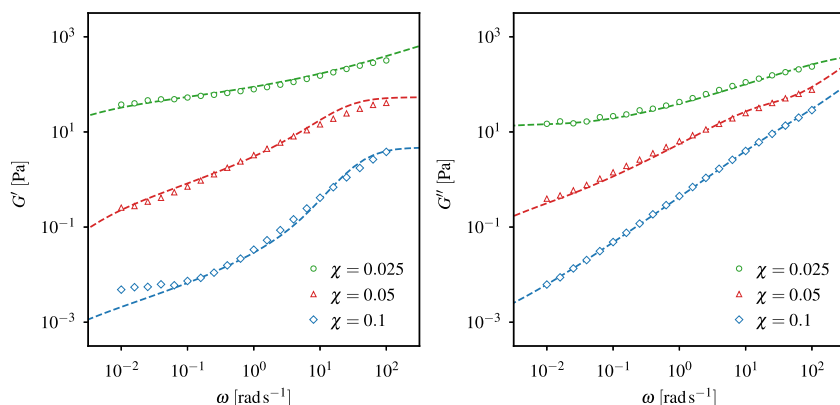


FIG. 5. Experimentally determined storage modulus G' (l.h.s) and loss modulus G'' (r.h.s) as functions of angular frequency ω for three cross-linking ratios χ at $\vartheta = 20$ °C. The dashed lines are fits employing the schematic model [Eq. (16)].

full investigated frequency range with minor deviations, especially at higher temperatures. With increasing cross-linking ratio χ , the overall magnitude of storage modulus G' and loss modulus G'' decreases. Furthermore, increasing χ results in a transition from a viscoelastic solid to a liquid-like gel. This also implies that G' and G'' decay more rapidly with decreasing frequency for higher cross-linking ratios. As such, the disparity between gels with different cross-linking ratios is more pronounced at lower frequencies.

Viscosity flow curves for different cross-linking densities are displayed in Fig. 6. Analogous to the linear viscoelastic moduli, the overall magnitude of the viscosity η is lowered for higher cross-linking ratios χ . All samples feature shear-thinning behavior, with the effect more noticeable for lower χ . For high shear rates, the viscosity reaches a similar order of magnitude for all investigated samples. For shear rates $\dot{\gamma} \lesssim 1$ s⁻¹, the measured viscosity can be described reasonably with the schematic MCT model. For higher shear rates, the theoretical prediction deviates from the measured

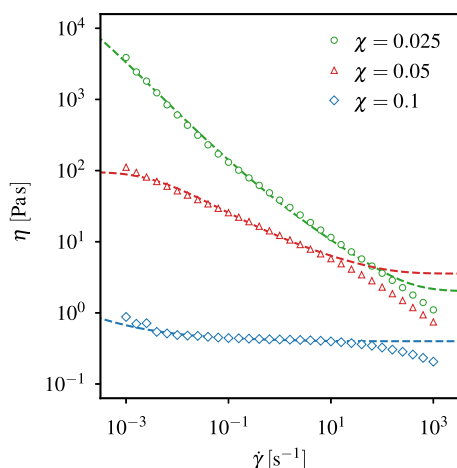


FIG. 6. Experimentally determined viscosity η as a function of shear rate $\dot{\gamma}$ for three cross-linking ratios χ at $\vartheta = 20$ °C. The dashed lines are fits employing the schematic model [Eq. (16)].

data as the model predicts the decay to a second Newtonian plateau for the given range of shear rates, while, in fact, a prolonged decay to even lower viscosities is observed. For the highest cross-linking ratio $\chi = 0.1$, the formation of an intermediate plateau is visible. As such, there appears to be evidence that for steady-state shearing, a secondary relaxation process, which cannot be described by ideal MCT emerges at high shear rates.

Given the success of the employed model to describe the experimental data, the observed effects can be interpreted in terms of the model parameters. The stress vertex v_σ scales the overall magnitude of both the viscoelastic moduli and the viscosity. v_σ is, therefore, strongly dependent on the cross-linking ratio χ and a systematic decrease of v_σ with rising χ is apparent. Surprisingly, the relaxation rate Γ does not change systematically with varying cross-linking ratio. While Γ is significantly larger for $\chi = 0.025$, the rates of the other two samples are of the same order of magnitude where, in fact, the lowest rates are observed for the intermediate cross-linking ratio $\chi = 0.05$. The critical shear rate $\dot{\gamma}_c$ only affects the relative scale of the viscosity's shear-rate dependence. As $\dot{\gamma}_c$ is greater for lower cross-linking densities, for these samples similar effects are observed at higher shear rates. The high frequency viscosity η_∞ has influence on both, the steady-state viscosity at high shear rates, and the viscoelastic moduli at high frequencies. However, as was pointed out previously, the model does not account for the measured viscosity at high shear rates for our samples, so that η_∞ is solely determined by the high-frequency behavior of the loss modulus G'' , adding the heuristic term $\omega\eta_\infty$ to the MCT prediction. For $\chi = 0.025$, η_∞ could not be estimated reliably. This parameter depends moderately on χ and is slightly reduced for higher cross-linking densities.

Employing the dimensionless moduli G'/v_σ , $(G'' - \omega\eta_\infty)/v_\sigma$ and the dimensionless frequency ω/Γ , the frequency-dependent response can be displayed independently of any scaling parameters (Fig. 7). The experimental data are located in an intermediate region between α - and β -process as clearly visible in this representation covering an extended range of frequencies. With this reduction, it is apparent that all samples approximately share the same qualitative high-frequency behavior, whereas differences between cross-linking ratios appear most prominently at low frequencies. Hence, the cross-linking ratio essentially influences the Debye-Waller factor f_c , i.e., the height of the G' -plateau. Similarly, using a reduced shear rate

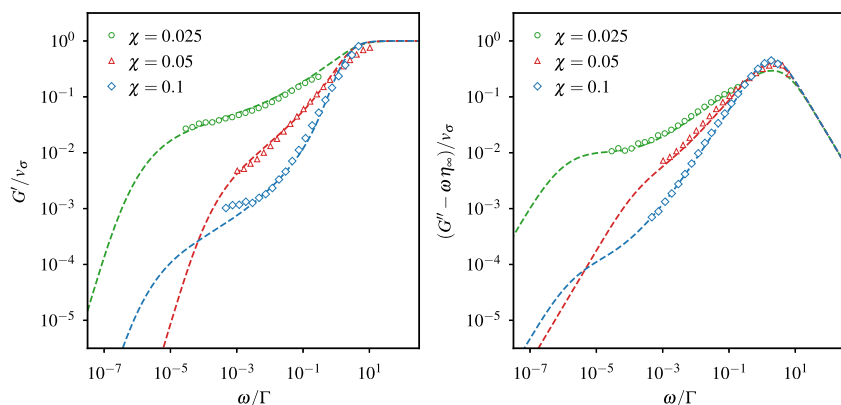


FIG. 7. Dimensionless storage modulus G'/v_σ (l.h.s) and loss modulus $(G'' - \omega\eta_\infty)/v_\sigma$ (r.h.s) as functions of dimensionless angular frequency ω/Γ for three cross-linking ratios χ at $\theta = 20^\circ\text{C}$. The dashed lines are fits employing the schematic model [Eq. (16)].

$\dot{\gamma}/\dot{\gamma}_c$, a dimensionless viscosity $\Gamma(\eta - \eta_\infty)/v_\sigma$ can be defined as displayed in Fig. S-7 in the [supplementary material](#). The experimental data deviate from the model fits for high shear rates and the reduction does also not lead to superimposition of the experimental high-shear-rate data.

The only quantities changing with cross-linking ratio are the separation parameter ε and the critical Debye–Waller factor f_c as the exponent parameter λ is assumed to be approximately constant for all χ . The critical Debye–Waller factor f_c strongly depends on the cross-linking ratio and decreases with rising χ . In the picture of MCT this means that for highly cross-linked gels, most of the density fluctuations decay during the β -relaxation, such that the cage dynamics typical for supercooled glass forming liquids are actually more pronounced for samples with lower cross-linking. As ε could not be determined for $\chi = 0.1$ reliably, only two cross-linking ratios can be compared. The absolute value of ε is diminished at the lower cross-linking ratio, indicating an approach to a dynamic arrest of slow modes. This is consistent with the observed overall increase of viscoelastic features for lower cross-linking ratios. Curiously, the scaled separation parameter ε^* is of the same order of magnitude for both samples, giving the impression that ε^* might be more suitable to quantify the approach to an ideal freezing transition when comparing different cross-linking ratios. With this assumption, the differences between samples beyond scaling parameters are mostly characterized by a change of the critical Debye–Waller factor f_c .

B. Temperature dependence

Due to the thermoresponsivity of pNIPAM, the rheological properties of these hydrogels sensitively can be tuned via the temperature as an external stimulus. The temperature-dependence of the viscosity and the linear viscoelastic moduli can for the most part be expressed through the three scaling parameters Γ , $\dot{\gamma}_c$, and η_∞ . The assumption that the stress vertex v_σ is temperature-independent is rather to keep the model as simple as possible and to avoid correlations between the parameters than by physical intuition. Since the high-shear-rate viscosity η_∞ and the rates Γ and $\dot{\gamma}_c$ all describe thermally activated dynamic processes, within a limited temperature range, a constant activation energy E_a can be determined employing an Arrhenius-type equation,

$$A(T) = A_0 \exp\left(\pm \frac{E_a}{RT}\right), \quad (18)$$

with the minus sign for the rates Γ and $\dot{\gamma}_c$ and the plus sign for the viscosity η_∞ . As exemplarily demonstrated in Fig. 8, the model parameters follow this behavior quite well, slightly deviating values are found only for temperatures close to the lower critical solution temperature of pNIPAM at $\sim 304\text{ K}$. Apparent activation energies E_a determined from least squares fits are compiled in Table II. Activation energies for all parameters are approximately of the same order of magnitude. Comparing different cross-linking densities, the most apparent variation of E_a with cross-linking ratio arises for the reciprocal critical shear rate $\dot{\gamma}_c^{-1}$, where more cross-linking leads to a lower activation energy and, therefore, less variation of $\dot{\gamma}_c$ with temperature. Opposite, the parameters η_∞ and Γ only moderately depend on the cross-linking ratio χ .

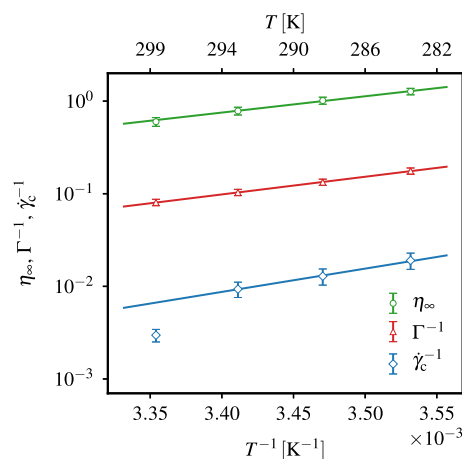


FIG. 8. Arrhenius plots of the high-frequency viscosity η_∞ , the reciprocal relaxation rate Γ^{-1} , and the reciprocal critical shear rate $\dot{\gamma}_c^{-1}$, exemplarily shown for $\chi = 0.05$. The lines indicate least-squares fits of the data employing Eq. (18), where for the determination of the activation energy resulting from $\dot{\gamma}_c^{-1}$ only the data obtained at the three lowest temperatures is considered.

TABLE II. Activation energies E_a and uncertainties determined from the temperature dependence of the reciprocal relaxation rate Γ^{-1} , the reciprocal critical shear rate $\dot{\gamma}_c^{-1}$, and the high-frequency viscosity η_∞ employing Eq. (18).

χ	Γ^{-1}	E_a [kJ mol $^{-1}$]	
		$\dot{\gamma}_c^{-1}$	η_∞
0.025	38.8(24)	60(5)	N/A
0.05	36.5(6)	48.1(24)	33.7(16)
0.1	45.2(6)	16(14)	30.6(14)

Qualitative changes in rheological behavior beyond scaling of magnitudes can be described by variation of the separation parameter ε^* , whose absolute value decreases with higher temperature, which actually implies an increase of viscoelastic features with rising temperatures. This is unexpected when comparing this behavior to concentrated suspensions of only intra-cross-linked spherical pNIPAM microgels, where an increase in temperature reduces the hydrodynamic radius of these particles, which in turn leads to a decrease of the effective volume fraction of the system.^{25,26} The mesostructural reason for this effect is still unknown, since for our system of inter-cross-linked microgels effects beyond the effective hydrodynamic radius influence the rheological properties. Increasing temperature leading to faster fluctuations of the hemiaminal cross-links is a possible reason.

VI. CONCLUSIONS

Hydrogels consisting of cross-linked pNIPAM are interesting model systems for the investigation of the nonergodicity of soft matter. Due to its thermosensitivity, the structural and dynamic properties of these systems are tunable by the temperature as an external stimulus. The most prominent property of hydrogels is their viscoelasticity that can be characterized employing steady-state as well as oscillatory shear experiments in dependence on the shear rate $\dot{\gamma}$, frequency ω , and amplitude of deformation γ_0 .

The rheological properties of hydrogels depend both on the polymer volume fraction ϕ and the cross-linking ratio χ . Here, we investigated at constant volume fraction $\phi \approx 0.1$ the influence of the cross-linking ratio χ .

Using a schematic mode-coupling approach with a rescaled F_{12} -model, a consistent description of the here described rheological properties in dependence on both, temperature and cross-linking ratio is possible. In contrast to the original F_{12} -model proposed by Götze,¹⁸ within the rescaled variant, the critical Debye–Waller factor f_c can be adjusted by a scaling parameter α . Since the cross-linking ratio χ strongly influences the critical Debye–Waller factor f_c , the original F_{12} -model is not capable to describe the steady-state viscosity and frequency-dependent complex moduli for all investigated cross-linking ratios.

Unexpectedly, the elasticity of these hydrogels increases with rising temperature and therewith approach to the lower critical solution temperature. This effect is more pronounced with decreasing cross-linking ratio χ . To identify the mesostructural reason for this unexpected temperature dependence, further experiments are required. Here, small angle neutron scattering (SANS) would be a method of choice to get structural information on relevant length scales in dependence on the temperature.

SUPPLEMENTARY MATERIAL

See the [supplementary material](#) for experimentally determined viscosities and viscoelastic moduli in the linear viscoelastic regime at different temperatures (Sec. S-I) and shear-rate-dependent reduced steady state viscosity (Sec. S-II).

ACKNOWLEDGMENTS

Financial support within the priority program SPP 1681 of the Deutsche Forschungsgemeinschaft is acknowledged.

AUTHOR DECLARATIONS

Conflict of Interest

The authors have no conflicts to disclose.

Author Contributions

Joel Diaz Maier: Conceptualization (equal); Investigation (equal); Software (equal); Validation (equal); Visualization (equal); Writing – original draft (equal). **Joachim Wagner:** Conceptualization (equal); Investigation (equal); Software (equal); Supervision (equal); Validation (equal); Visualization (equal).

DATA AVAILABILITY

The data that support the findings of this study are available from the corresponding author upon reasonable request.

REFERENCES

- Y. E. Shapiro, *Prog. Polym. Sci.* **36**, 1184–1253 (2011).
- M. L. Oyen, *Int. Mater. Rev.* **59**, 44–59 (2014).
- P. H. Corkhill, C. J. Hamilton, and B. J. Tighe, *Biomaterials* **10**, 3–10 (1989).
- P. Gupta, K. Vermani, and S. Garg, *Drug Discov. Today* **7**, 569–579 (2002).
- B. Baroli, *J. Pharm. Sci.* **96**, 2197–2223 (2007).
- C.-C. Lin and K. S. Anseth, *Pharm. Res.* **26**, 631–643 (2009).
- J. Tavakoli and Y. Tang, *Polymers* **9**, 364 (2017).
- J. Wu, Z.-G. Su, and G.-H. Ma, *Int. J. Pharm.* **315**, 1–11 (2006).
- R. Marcombe, S. Cai, W. Hong, X. Zhao, Y. Lapusta, and Z. Suo, *Soft Matter* **6**, 784–793 (2010).
- H. G. Schild, *Prog. Polym. Sci.* **17**, 163–249 (1992).
- M. Heskins and J. E. Guillet, *J. Macromol. Sci., Chem.* **2**, 1441–1455 (1968).
- P. N. Pusey and W. van Megen, *Nature* **320**, 340–342 (1986).
- P. N. Pusey and W. van Megen, *Phys. Rev. Lett.* **59**, 2083–2086 (1987).
- W. Härtl, H. Versmold, and X. Zhang-Heider, *J. Chem. Phys.* **102**, 6613–6618 (1995).
- W. Härtl, *Curr. Opin. Colloid Interfaces* **6**, 479–483 (2001).
- B. R. Saunders and B. Vincent, *Adv. Colloid Interface Sci.* **80**, 1–25 (1999).
- U. Bengtzelius, W. Götze, and A. Sjolander, *J. Phys. C: Solid State* **17**, 5915–5934 (1984).
- W. Götze, *Z. Phys. B: Condens. Matter* **56**, 139–154 (1984).
- G. Szamel and H. Löwen, *Phys. Rev. A* **44**, 8215–8219 (1991).
- M. Fuchs and M. E. Cates, *Phys. Rev. Lett.* **89**, 248304 (2002).
- M. Fuchs and M. E. Cates, *J. Phys.: Condens. Matter* **17**, S1681–S1696 (2005).
- G. Nägele and J. Bergenholtz, *J. Chem. Phys.* **108**, 9893–9904 (1998).

- ²³A. J. Banchio, G. Nägele, and J. Bergenholtz, *J. Chem. Phys.* **111**, 8721–8740 (1999).
- ²⁴M. Fuchs, “Nonlinear rheological properties of dense colloidal dispersions close to a glass transition under steady shear,” in *High Solid Dispersions*, edited by M. Cloitre (Springer, Berlin, Heidelberg, 2010), pp. 55–115.
- ²⁵J. J. Crassous, M. Siebenbürger, M. Ballauff, M. Drechsler, D. Hajnal, O. Henrich, and M. Fuchs, *J. Chem. Phys.* **128**, 204902 (2008).
- ²⁶M. Siebenbürger, M. Fuchs, H. Winter, and M. Ballauff, *J. Rheol.* **53**, 707–726 (2009).
- ²⁷J. M. Brader, M. Siebenbürger, M. Ballauff, K. Reinheimer, M. Wilhelm, S. J. Frey, F. Weysser, and M. Fuchs, *Phys. Rev. E* **82**, 061401 (2010).
- ²⁸A. Nack, J. Seifert, C. Passow, and J. Wagner, *J. Appl. Crystallogr.* **51**, 87–96 (2018).
- ²⁹N. Lucht, S. Hinrichs, L. Großmann, C. Pelz, E. Felgenhauer, E. Clasen, M. Schwenk, and B. Hankiewicz, *Phys. Sci. Rev.* 20190120 (2021).
- ³⁰V. Krakoviack and C. Alba-Simionesco, *J. Chem. Phys.* **117**, 2161–2171 (2002).
- ³¹T. Franosch, W. Götze, M. R. Mayr, and A. P. Singh, *Phys. Rev. E* **55**, 3183–3190 (1997).
- ³²A. P. Singh, G. Li, W. Götze, M. Fuchs, T. Franosch, and H. Z. Cummins, *J. Non-Cryst. Solids* **235–237**, 66–70 (1998).
- ³³B. Rufflé, S. Beaufils, B. Toudic, C. Ecolivet, A. Le Sauze, and R. Marchand, *J. Non-Cryst. Solids* **235–237**, 244–249 (1998).
- ³⁴B. Rufflé, C. Ecolivet, and B. Toudic, *Europhys. Lett.* **45**, 591–597 (1999).
- ³⁵M. Domschke, M. Marsilius, T. Blochowicz, and T. Voigtmann, *Phys. Rev. E* **84**, 031506 (2011).
- ³⁶R. Zwanzig, *J. Chem. Phys.* **33**, 1338–1341 (1960).
- ³⁷R. Zwanzig, *Phys. Rev.* **124**, 983–992 (1961).
- ³⁸H. Mori, *Prog. Theor. Phys.* **33**, 423–455 (1965).
- ³⁹H. Mori, *Prog. Theor. Phys.* **34**, 399–416 (1965).
- ⁴⁰W. Götze, *Z. Phys. B: Condens. Matter* **60**, 195–203 (1985).
- ⁴¹W. Götze, *J. Phys.: Condens. Matter* **2**, 8485–8498 (1990).
- ⁴²M. Fuchs and M. E. Cates, *Faraday Discuss.* **123**, 267–286 (2003).
- ⁴³J. M. Brader, T. Voigtmann, M. Fuchs, R. G. Larson, and M. E. Cates, *Proc. Natl. Acad. Sci. U. S. A.* **106**, 15186–15191 (2009).
- ⁴⁴D. Hajnal and M. Fuchs, *Eur. Phys. J. E* **28**, 125–138 (2009).
- ⁴⁵J. M. Brader, T. Voigtmann, M. E. Cates, and M. Fuchs, *Phys. Rev. Lett.* **98**, 058301 (2007).
- ⁴⁶J. M. Brader, M. E. Cates, and M. Fuchs, *Phys. Rev. Lett.* **101**, 138301 (2008).
- ⁴⁷C. Alba-Simionesco and M. Krauzman, *J. Chem. Phys.* **102**, 6574–6585 (1995).
- ⁴⁸C. Alba-Simionesco, V. Krakoviack, M. Krauzman, P. Migliardo, and F. Romain, *J. Raman Spectrosc.* **27**, 715–721 (1996).
- ⁴⁹V. Krakoviack, C. Alba-Simionesco, and M. Krauzman, *J. Chem. Phys.* **107**, 3417–3427 (1997).
- ⁵⁰M. Fuchs, W. Götze, I. Hofacker, and A. Latz, *J. Phys.: Condens. Matter* **3**, 5047–5071 (1991).
- ⁵¹E. Flenner and G. Szamel, *Phys. Rev. E* **72**, 031508 (2005).
- ⁵²Z. Hu and G. Huang, *Angew. Chem., Int. Ed.* **42**, 4799–4802 (2003).
- ⁵³J. L. Barrat, W. Götze, and A. Latz, *J. Phys.: Condens. Matter* **1**, 7163–7170 (1989).
- ⁵⁴M. Fuchs, I. Hofacker, and A. Latz, *Phys. Rev. A* **45**, 898–912 (1992).
- ⁵⁵M. Bernabei, A. J. Moreno, and J. Colmenero, *Phys. Rev. Lett.* **101**, 255701 (2008).
- ⁵⁶M. Sperl, *Phys. Rev. E* **68**, 031405 (2003).
- ⁵⁷E. Zaccarelli, G. Foffi, K. A. Dawson, S. V. Buldyrev, F. Sciortino, and P. Tartaglia, *Phys. Rev. E* **66**, 041402 (2002).
- ⁵⁸A. J. Moreno and J. Colmenero, *Phys. Rev. E* **74**, 021409 (2006).

Supplementary Material

Viscoelastic properties of pNIPAM-Hydrogels: A mode coupling theory study

Joel Diaz Maier¹ and Joachim Wagner^{1, a)}

Institut für Chemie, Universität Rostock, 18051 Rostock, Germany

S-I. TEMPERATURE DEPENDENCE OF SHEAR VISCOSITY AND VISCOELASTIC MODULI IN THE LINEAR VISCOELASTIC REGIME

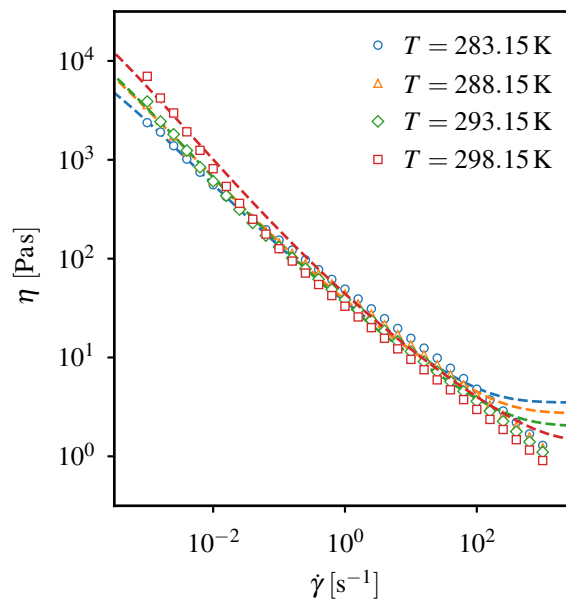


FIG. S-1. Experimentally determined viscosity η as a function of shear rate $\dot{\gamma}$ for four temperatures T at cross-linking ratio $\chi = 0.025$. Dashed lines are fits employing the schematic model [Eq. (16)].

^{a)}Electronic mail: joachim.wagner@uni-rostock.de

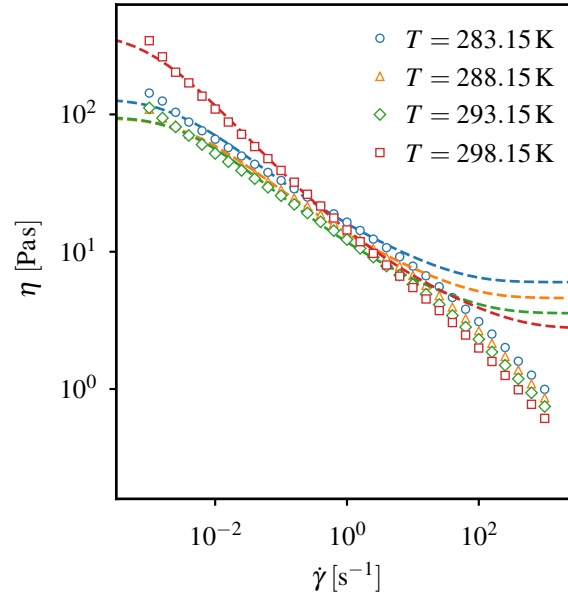


FIG. S-2. Experimentally determined viscosity η as a function of shear rate $\dot{\gamma}$ for four temperatures T at cross-linking ratio $\chi = 0.05$. Dashed lines are fits employing the schematic model [Eq. (16)].

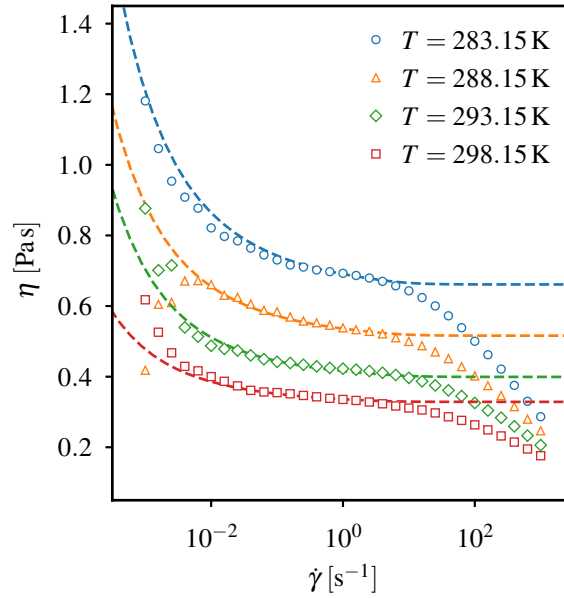


FIG. S-3. Experimentally determined viscosity η as a function of shear rate $\dot{\gamma}$ for four temperatures T at cross-linking ratio $\chi = 0.1$. Dashed lines are fits employing the schematic model [Eq. (16)].

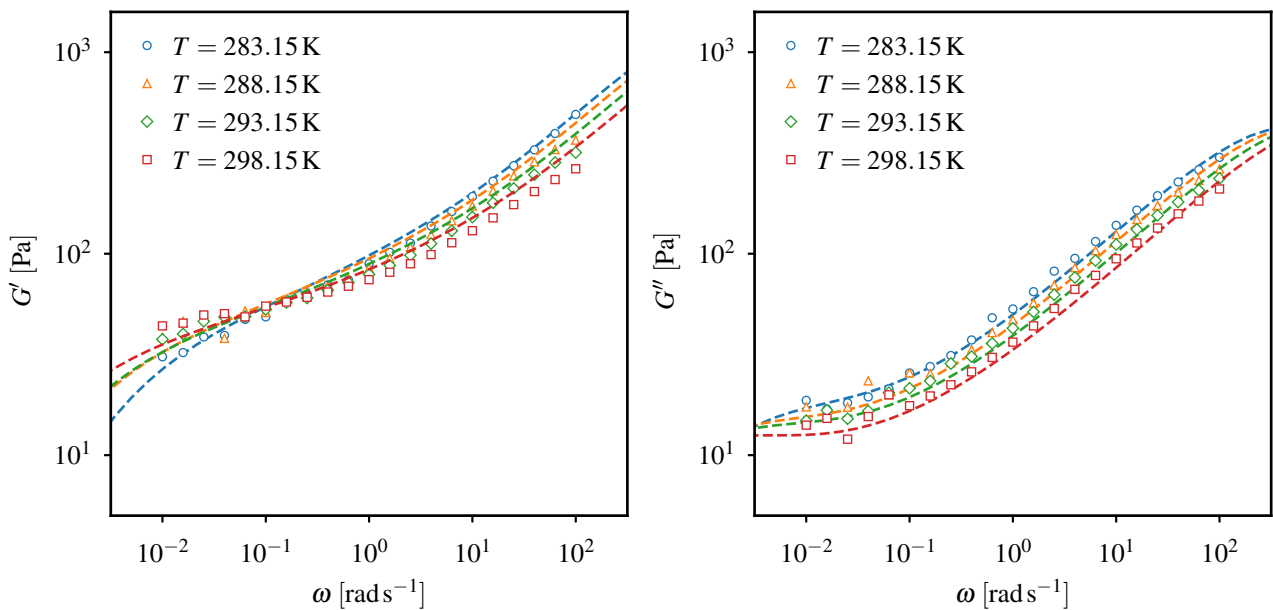


FIG. S-4. Experimentally determined storage modulus G' (l.h.s) and loss modulus G'' (r.h.s) as functions of angular frequency ω for four temperatures T at cross-linking ratio $\chi = 0.025$. Dashed lines are fits employing the schematic model [Eq. (16)].

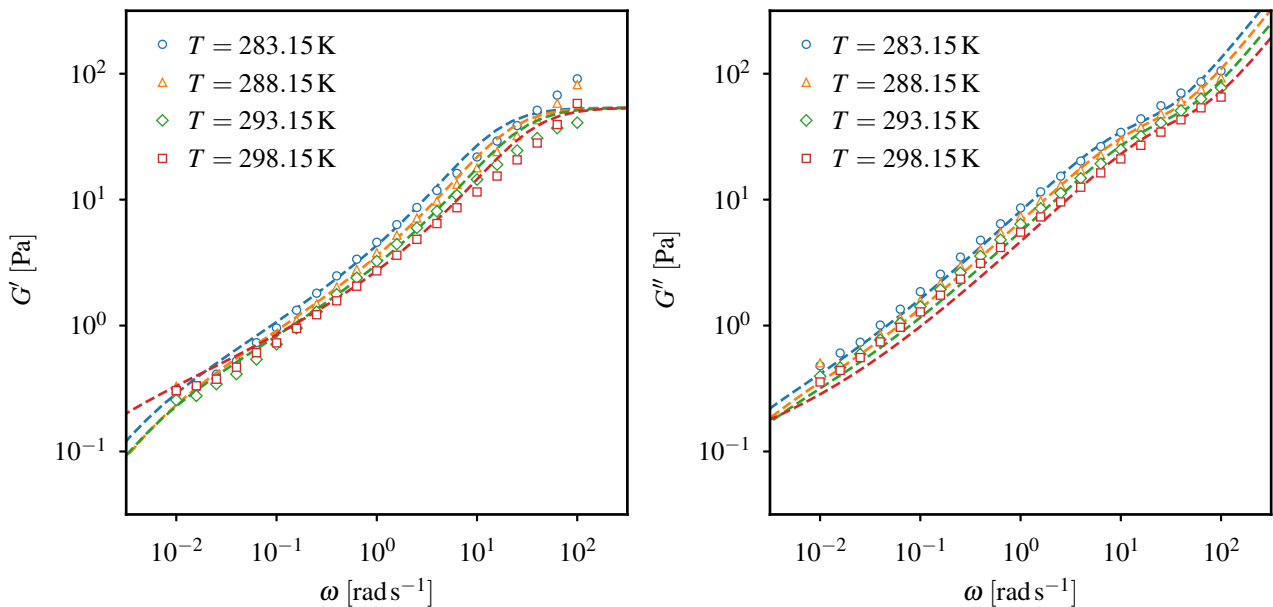


FIG. S-5. Experimentally determined storage modulus G' (l.h.s) and loss modulus G'' (r.h.s) as functions of angular frequency ω for four temperatures T at cross-linking ratio $\chi = 0.05$. Dashed lines are fits employing the schematic model [Eq. (16)].

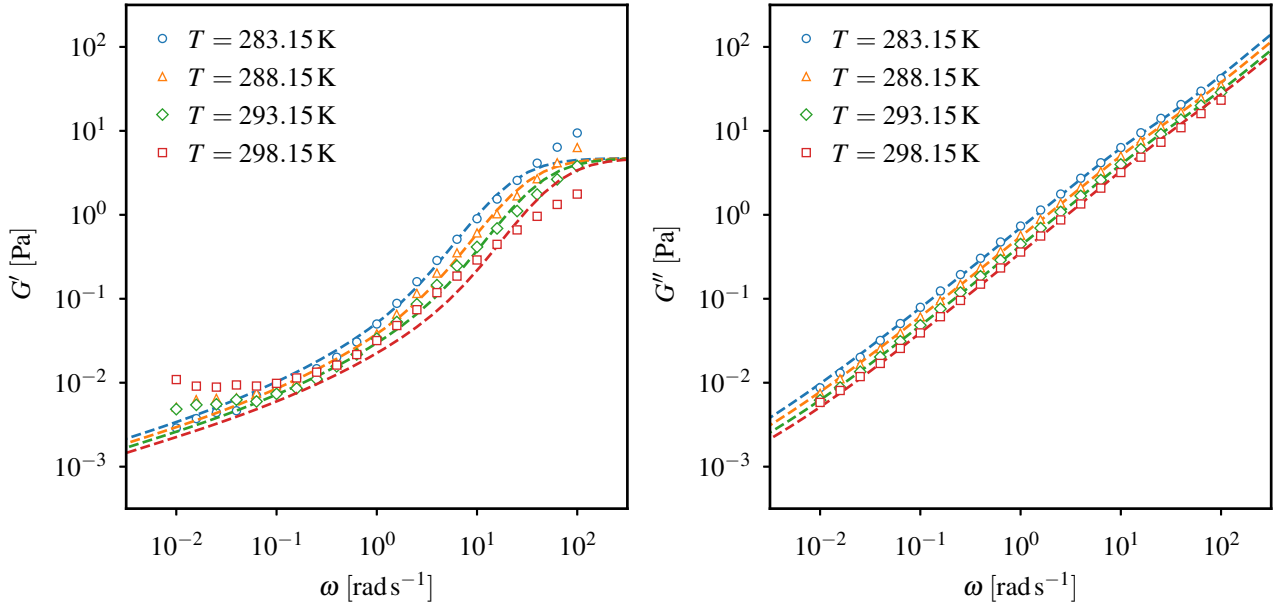


FIG. S-6. Experimentally determined storage modulus G' (l.h.s) and loss modulus G'' (r.h.s) as functions of angular frequency ω for four temperatures T at cross-linking ratio $\chi = 0.1$. Dashed lines are fits employing the schematic model [Eq. (16)].

S-II. SHEAR-RATE DEPENDENT, DIMENSIONLESS STEADY STATE VISCOSITY

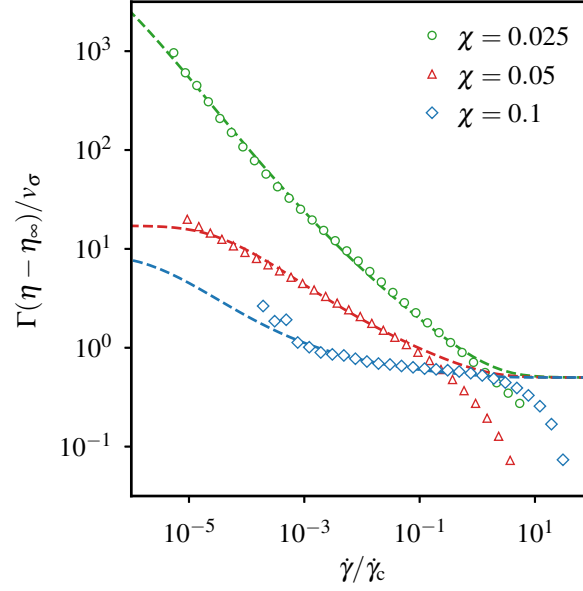


FIG. S-7. Dimensionless viscosity $\Gamma(\eta - \eta_\infty)/v_\sigma$ as a function of dimensionless shear rate $\dot{\gamma}/\dot{\gamma}_c$ for three cross-linking ratios χ at $\vartheta = 20^\circ\text{C}$. The dashed lines are fits employing the schematic model [Eq. (16)].

Publication II

Structure and short-time diffusion of concentrated suspensions consisting of silicone-stabilised PMMA particles: a quantitative analysis taking polydispersity effects into account

J. Diaz Maier and J. Wagner

Soft Matter **20**, 1309–1319 (2024)

<https://doi.org/10.1039/D3SM01510F>

Open-access article distributed under the terms of the Creative Commons Attribution 3.0 Unported (CC-BY 3.0) License.

Contribution:

I conceptualized this work together with J.W. I performed the experiments, implemented the combined multi-component hard-sphere/core-shell/ $\delta\gamma$ -theory model, developed software for data analysis, performed fits, analyzed the results and wrote the original draft. The manuscript was revised together with J.W.

My approximated contribution to the publication in percent: 90 %



Cite this: *Soft Matter*, 2024,
20, 1309

Structure and short-time diffusion of concentrated suspensions consisting of silicone-stabilised PMMA particles: a quantitative analysis taking polydispersity effects into account

Joel Diaz Maier  and Joachim Wagner *

We characterise structure and dynamics of concentrated suspensions of silicone-stabilised PMMA particles immersed in index-matching decalin–tetralin mixtures by means of static and quasielastic light scattering experiments. These particles can reproducibly be prepared *via* a comparatively easy route and are thus promising model systems with hard-sphere interaction. We demonstrate the hard-sphere behaviour of dense suspensions of these systems rigorously taking polydispersity effects into account. Structure factors $S(Q)$ can in the entire range of volume fractions with liquid-like structure quantitatively be modelled using a multi-component Percus–Yevick ansatz regarding the particle size distribution and the form factor assuming a core–shell model with a scattering length density gradient in the PMMA core. Herewith, hydrodynamic functions $H(Q)$ are in the whole accessible Q -range beyond the second maximum of $H(Q)$ quantitatively modelled using a rescaled $\delta\gamma$ -approach for all investigated volume fractions. With these data, previously provided characterisation of dilute systems is extended: the excellent agreement of structural and dynamic properties with theoretical predictions for hard spheres demonstrates the suitability of these particles as a model system for hard spheres.

Received 8th November 2023,
Accepted 13th January 2024

DOI: 10.1039/d3sm01510f

rsc.li/soft-matter-journal

1 Introduction

Colloidal suspensions have attracted wide interest as highly defined and tunable model systems for the investigation of condensed matter. The hard-sphere model is of special interest, as it describes, despite its simplicity, the most fundamental properties of dense, simple liquids with a dominating repulsive interaction potential.^{1,2} Initiated by the pioneering work of Pusey and van Megen,^{3,4} suspensions of sterically stabilised poly(methyl methacrylate) (PMMA) particles in non-polar solvents are the most commonly used colloidal model systems for experimental studies of hard spheres, which encompass investigations of the bulk phase behaviour,^{3,5} the fluid structure, both in reciprocal space *via* scattering experiments^{6,7} and in real space *via* microscopy,^{8–10} structure-dynamics relations,^{11–14} crystalline^{15,16} and glass-like^{17–22} structures as well as the study of non-equilibrium phenomena such as sedimentation under gravity²³ or rheological properties.^{24,25}

Synthesis *via* dispersion polymerisation²⁶ yields particles which are composed of a solid PMMA core, surrounded by a shell of stabiliser molecules, whose steric hindrance prevents the aggregation of particles upon close contact, leading to steep

repulsive forces. The most commonly employed stabiliser is a poly(12-hydroxystearic acid) (PHSA) comb polymer whose synthesis is well studied²⁷ but nevertheless considered difficult and a major obstacle for a reproducible particle synthesis with the detailed complications being described in depth elsewhere.^{28,29}

In the pursuit of alternatives, a class of poly(dimethylsiloxane) (PDMS)-based stabilisers recently gained attention. Unlike their PHSA counterpart, these PDMS-stabilisers are commercially available and can directly be copolymerised with MMA due to their reactive end-group functionalisation which considerably simplifies the preparation of suspensions. The synthesis of these PMMA–PDMS particles and the influence of varying reaction conditions on the particle size and polydispersity is well documented.^{30,31} In a recent small-angle neutron scattering (SANS)-study,²⁹ the particles were confirmed to exhibit a core–shell structure analogue to the well known PMMA–PHSA colloids. Furthermore, the study revealed several characteristics of the novel dispersions: The size distribution of submicron-sized particles suitable for scattering experiments is generally slightly broader and the stabiliser shell is slightly thicker than for PMMA–PHSA particles of comparable size. On the other hand, there is an enhanced difference of the scattering contrast between the core and the shell, which generally enables a clearer determination of the scattering form

Institut für Chemie, Universität Rostock, 18051 Rostock, Germany.
E-mail: joachim.wagner@uni-rostock.de



factor. It is worth mentioning that the shell thickness and thus the core-to-shell ratio of these particles can to a certain degree be tuned by employing PDMS-stabilisers with different molecular weight. Particles of this type are already adopted in multiple studies concerning the gelation of colloid-polymer mixtures,^{32–36} the formation of crystalline structures³⁷ or the particle transport in microfluidic channels.³⁸

In comparison to the established, thoroughly characterised PMMA-PHSA colloids, studies of PDMS-stabilised particles' topology and dynamics are rather limited. In this work, we investigate structure-dynamics relations of these particles in dense, fluid-like suspensions *via* static and dynamic light scattering. By studying concentrated systems, not only information on the particle morphology, but also on their local ordering is attainable from the scattered intensity. Thus, by comparing experimentally obtained static structure factors with theoretical predictions, the suitability of PDMS-stabilised PMMA particles as a hard-sphere model system can be tested. Dynamic scattering experiments give access to the wavevector-dependent diffusion of the particles which is influenced both by potential and solvent-mediated, hydrodynamic interactions. By investigating the relation between structural and hydrodynamic features, it can be assessed if the hard-sphere character of these particles also manifests itself in the hydrodynamics of the system.

2 Theoretical background

2.1 Scattering of polydisperse particles

Consider a multicomponent system consisting of n distinct species of isotropically interacting, spherical particles, where the composition is specified by the number fraction $x_\alpha = N_\alpha/N$, which is the ratio of the number of particles N_α of species α to the total number of particles N . For such a system, the wavevector-dependent mean intensity,

$$I(Q) \propto \sum_{\alpha,\beta=1}^n (x_\alpha x_\beta)^{1/2} b_\alpha(Q) b_\beta(Q) S_{\alpha\beta}(Q), \quad (1)$$

probed in a static scattering experiment, is proportional to the weighted sum of the scattering amplitudes $b_\alpha(Q)$, describing the scattering function of a single particle of species α , and the partial structure factors $S_{\alpha\beta}(Q)$, representing interparticle correlations.³⁹ The scattering amplitude

$$b_\alpha(Q) = 4\pi \int_0^\infty \rho_\alpha(r) r^2 \frac{\sin(Qr)}{Qr} dr \quad (2)$$

is given by the Fourier–Bessel transform of the scattering contrast $\rho_\alpha(r)$, which for light scattering is proportional to the difference between the refractive index of the particle and the refractive index of the surrounding medium. The partial structure factors can in principle be retrieved from computer simulations or by employing integral equation schemes. For hard spheres, an analytical solution for $S_{\alpha\beta}(Q)$ for an arbitrary number of components can be obtained by solving the

multicomponent Ornstein–Zernike equation employing the Percus–Yevick closure.^{40–43}

In the absence of particle interactions, with $S_{\alpha\beta}(Q) = \delta_{\alpha\beta}$, where $\delta_{\alpha\beta}$ denotes the Kronecker symbol, eqn (1) reduces to

$$\overline{b^2}(Q) = \sum_{\alpha=1}^n x_\alpha b_\alpha^2(Q), \quad (3)$$

the squared scattering amplitude averaged over the size distribution. Similar to a monodisperse system, formally, the factorisation $I(Q) \propto P(Q)S_M(Q)$ into the normalised average form factor $P(Q) = \overline{b^2}(Q)/\overline{b^2}(0)$ and the measurable structure factor,

$$S_M(Q) = \left[\overline{b^2}(Q) \right]^{-1} \sum_{\alpha,\beta=1}^n (x_\alpha x_\beta)^{1/2} b_\alpha(Q) b_\beta(Q) S_{\alpha\beta}(Q) \quad (4)$$

can be employed for polydisperse suspensions. This structure factor is experimentally accessible by dividing the scattered intensity of a concentrated suspension by the intensity of a diluted system, weighted by the concentration ratio of the two samples. Within this procedure, special care has to be taken that the particle morphology in the concentrated sample is the same as in the diluted state. $S_M(Q)$ is influenced not only by the interparticle correlations but also by the scattering properties on a single particle level, which also means that samples with the same particle interactions but different form factors yield disparate measurable structure factors. A measure for the overall local ordering of the suspension, irrespective of the individual particle sizes and shapes, is the total structure factor,

$$S_{\text{tot}}(Q) = \sum_{\alpha,\beta=1}^n (x_\alpha x_\beta)^{1/2} S_{\alpha\beta}(Q), \quad (5)$$

which is independent of the scattering amplitudes.

For the particle size distribution, a reasonable choice for polymeric colloids is given by the Schulz–Flory distribution, originally derived to describe the molecular weight distribution of polymers,^{44,45}

$$c(R) = \frac{1}{\Gamma(Z+1)} \left(\frac{Z+1}{R_0} \right)^{Z+1} R^Z \exp\left(-\frac{Z+1}{R_0} R \right) \quad (6)$$

as the probability density function (pdf) of the total particle radius R , where $\Gamma(x)$ denotes the Gamma function. $R_0 = \langle R \rangle$ is the mean radius and the parameter Z is related to the polydispersity p of the suspension as $p^2 = (\langle R^2 \rangle - \langle R \rangle^2) / \langle R \rangle^2 = 1/(Z+1)$. We discretise the pdf to a more tractable n -component mixture, where the radii and number fractions for the resulting histogram are chosen such that the first $2n-1$ moments of the discrete and the continuous distribution match. This is essentially the application of an n -point Gaussian quadrature rule to integrate over the size distribution. For the Schulz–Flory distribution in particular, the roots of the generalised Laguerre polynomials can be employed.^{46,47} Because of the rather small wavevector range accessible in static light scattering experiments, only a small number of nodes is necessary for convergence.



2.2 Short-time dynamics and hydrodynamic function

Photon correlation spectroscopy probes dynamical properties by analysing the time-dependent fluctuations of the scattered intensity $I(Q,t)$. The normalised measurable intermediate scattering function (ISF) $\Phi_M(Q,t) = S_M(Q,t)/S_M(Q,0)$ is accessible from the intensity correlation function $g_2(Q,t)$ accessed in a homodyne dynamic scattering experiment. For ergodic systems, $g_2(Q,t)$ is connected to $\Phi_M(Q,t)$ by the Siegert relation,⁴⁸

$$g_2(Q,t) = \frac{\langle I(Q,0)I(Q,t) \rangle_t}{\langle I(Q,0) \rangle_t^2} = 1 + \beta(Q)\Phi_M^2(Q,t), \quad (7)$$

where the factor $\beta(Q)$ depends on the coherence properties of the radiation and the detector's aperture. The angular brackets $\langle \dots \rangle_t$ denote a time average. Similar to eqn (4), $S_M(Q,t)$ is related to the scattering amplitudes $b_\alpha(Q)$ and the partial ISFs $S_{\alpha\beta}(Q,t)$:

$$S_M(Q,t) = \left[\overline{b^2(Q)} \right]^{-1} \sum_{\alpha,\beta=1}^n (x_\alpha x_\beta)^{1/2} b_\alpha(Q) b_\beta(Q) S_{\alpha\beta}(Q,t). \quad (8)$$

In the short-time regime, for correlation times larger than the momentum relaxation time but smaller than the structural relaxation time, the particles exhibit simple translational Brownian motion and the normalised ISF is characterised by the exponential form

$$\Phi_M(Q,t) = \exp[-D_{\text{eff}}(Q)Q^2 t], \quad (9)$$

with an effective, collective diffusion coefficient $D_{\text{eff}}(Q)$, which for polydisperse samples can be written as

$$D_{\text{eff}}(Q) = \overline{D_0(Q)} \frac{H_M(Q)}{S_M(Q)}, \quad (10)$$

and is also called extended de Gennes relation.^{39,49} Here, $\overline{D_0(Q)}$ denotes the mean Stokes–Einstein diffusion coefficient, which can be expressed as a weighted average of the diffusion coefficients of the single species,

$$\overline{D_0(Q)} = \left[\overline{b^2(Q)} \right]^{-1} \sum_{\alpha=1}^n x_\alpha b_\alpha^2(Q) D_{0,\alpha}, \quad (11)$$

with

$$D_{0,\alpha} = \frac{k_B T}{6\pi\eta_0 R_{h,\alpha}}, \quad (12)$$

where k_B indicates Boltzmann's constant, T the temperature, η_0 the viscosity of the surrounding medium and $R_{h,\alpha}$ the hydrodynamic radius of the particles of species α . The measurable hydrodynamic function

$$H_M(Q) = \left[\overline{b^2(Q)} \right]^{-1} \sum_{\alpha,\beta=1}^n (x_\alpha x_\beta)^{1/2} b_\alpha(Q) b_\beta(Q) H_{\alpha\beta}(Q), \quad (13)$$

is experimentally accessible if $D_{\text{eff}}(Q)$, $\overline{D_0(Q)}$ and $S_M(Q)$ are known from static and dynamic scattering experiments. $H_M(Q)$ is related to the partial hydrodynamic functions $H_{\alpha\beta}(Q)$ whose calculation however, remains a computationally challenging task. For monodisperse systems, the hydrodynamic function $H(Q)$ can be calculated with the semi-analytical $\delta\gamma$ -scheme

proposed by Beenakker and Mazur,^{50,51} which gives a satisfactory approximation for the wavevector-dependent short-time diffusion of hard spheres, but can in principle be employed for any interaction potential, as the scheme only depends on the structure factor of the system as an external input.⁵² $H(Q)$ can be decomposed into the sum of a wavevector-independent self part and a wavevector-dependent distinct part according to

$$H(Q) = \frac{D_s}{D_0} + H^d(Q), \quad (14)$$

where the self part contains the short-time self diffusion coefficient D_s . Within the $\delta\gamma$ -scheme, the distinct part of the hydrodynamic function can be calculated from the static structure factor $S(Q)$ with the relation

$$H^d(x) = \frac{3}{2\pi} \int_0^\infty \left[\frac{\sin x'}{x'} \right] [1 + \varphi S_{\gamma_0}(x')]^{-1} \times \int_{-1}^1 (1 - \mu^2) [S(|\mathbf{x} - \mathbf{x}'|) - 1] d\mu dx', \quad (15)$$

where φ is the volume fraction, $x = 2QR$ is a reduced wavevector with the particle radius R and $\mu = \hat{\mathbf{x}} \cdot \hat{\mathbf{x}'}$ is the cosine of the angle enclosed by the unit vectors $\hat{\mathbf{x}}$ and $\hat{\mathbf{x}'}$. The calculation of the function $S_{\gamma_0}(x)$ is described ref. 52. Although the self part of $H(Q)$ can in principle also be calculated employing the $\delta\gamma$ -scheme, the method can be significantly improved if instead more accurate, semi-empirical expressions for D_s are used or if D_s is directly fitted to experimental data or simulation results.^{53,54} It has been shown that the combination of the $\delta\gamma$ -approach with a more elaborate description of D_s produces hydrodynamic functions in satisfactory agreement with computer simulations.⁵⁵

3 Experimental section

3.1 Materials

Dodecane, methyl methacrylate (MMA), 2,2'-azobis(2-methylpropionitrile) (AIBN), 1-octanethiol and 1,2,3,4-tetrahydronaphthalene (tetralin) were purchased from Sigma-Aldrich, monomethacryloxypropyl-terminated poly(dimethylsiloxane) (PDMS-MA) (10 000 g mol⁻¹) from ABCR and decahydronaphthalene (decalin, *cis/trans*-mixture) from Carl Roth. Tetralin and decalin were thoroughly filtered through 0.2 μm syringe filters to remove dust particles, other than that, all chemicals were used as received.

3.2 Dispersion polymerisation

The particles are synthesised by radical dispersion polymerisation following previously reported procedures.^{29–31}

In a round bottom flask, 140 ml dodecane and 3.0 ml PDMS-MA were degassed with nitrogen for 30 min and afterwards heated to 80 °C under magnetic stirring. Simultaneously, a mixture of 15.0 ml MMA, 145 mg AIBN and 175 μl 1-octanethiol was prepared in a round bottom flask and also degassed with nitrogen for 30 min at room temperature. To start the reaction, the monomer solution was added to the stabiliser solution with a syringe. After 5 min, the initially transparent solution turned



opaque, indicating the start of the polymerisation. The reaction was maintained in a nitrogen atmosphere at 80 °C for 4 h. After cooling down, the dispersion was purified by 4 cycles of centrifugation and redispersion in fresh decalin.

3.3 Sample preparation

A stock suspension of the particles was refractive-index matched in a mixture of decalin ($n_D^{20} = 1.474$) and tetralin ($n_D^{20} = 1.541$). This solvent mixture is known to cause a slight swelling of the particles, induced by the partial diffusion of the solvent molecules into the particle core.^{5,56} The final refractive index of the suspension was adjusted to $n_D^{20} = 1.496$ after a swelling period of one week after which the optical transparency persisted for several months even at high particle concentrations with no indication of polymer degradation due to the solvent. From the index-matched stock dispersion, samples of different particle concentrations in the fluid range were prepared either by concentration *via* centrifugation or by dilution with the index-matching solvent directly inside cylindrical quartz cuvettes. We additionally prepared from the same batch one highly concentrated suspension as a metastable colloidal glass. The fluid-like samples were gently mixed employing a vortex mixer to ensure sample homogeneity before the light scattering measurements. The mass density of the solvent mixture is slightly lower than that of the particles, however, no significant sedimentation effects and additionally no signs of crystallisation could be detected over a span of 48 h for the submicron sized colloids.

3.4 Light scattering

Light scattering experiments were performed with a CGS-3 goniometer supplied by ALV GmbH, Langen (Germany), employing an ALV/LSE-5004 multiple tau digital correlator, an avalanche photodiode single-photon detector with an optical fibre based detection unit and a frequency doubled Nd:YAG-Laser (wavelength 532 nm) as a light source. The cuvettes were placed in a temperature index matching vat filled with filtered toluene. All measurements were conducted at 20 °C, where the temperature was monitored with a Pt-100 sensor. The temperature stability of the setup is better than ± 0.1 K.

For static light scattering experiments, the scattered intensity was recorded at 90 distinct scattering angles for 30 s each, in a range between 30° and 150° such that the resulting scattering vectors $Q = (4\pi n/\lambda)\sin(\theta/2)$ are equidistantly spaced. The sample cuvettes were continuously rotated during the measurement to achieve ensemble averaging through the illumination of many independent scattering volumes. The recorded mean intensity was corrected for the intensity of the incident beam, the size of the illuminated sample volume and for background contributions of the cuvette and the pure solvent. In dynamic light scattering experiments, the intensity autocorrelation function $g_2(Q, t)$ was measured under the same conditions at the same scattering angles for 20 min each, however, without rotation of the sample cell.

4 Results and discussion

To model the scattering function of the particles, we employ an extended core-shell model, which also takes into account a possibly inhomogeneous core contrast caused by permeation of the decalin-tetralin mixture. For simplicity, it is assumed that this refractive-index gradient can be described by a linear decay inside the core, while the refractive index of the shell is assumed to be constant. This coarse-grained description of the particle is appropriate for the restricted wavevector-range accessible with static light scattering, where, in particular, detailed features of the surface morphology of the grafted stabiliser shell cannot be resolved. With these assumptions, the scattering contrast $\rho(r)$ in dependence on the distance r from the particle center is represented by

$$\rho(r) = \begin{cases} \rho_0 + (\rho_R - \rho_0)\frac{r}{R_c}, & \text{for } R_c \geq r, \\ \rho_\Delta, & \text{for } R_c + \Delta \geq r > R_c, \\ 0, & \text{for } r > R_c + \Delta, \end{cases} \quad (16)$$

where R_c is the core radius, Δ is the shell thickness and ρ_0 , ρ_R and ρ_Δ denote the contrast at the center of the core, at the boundary between core and shell and inside the shell, respectively. A Schulz-Flory function [eqn (6)] is used to model the size distribution of the particle cores while the stabiliser shell thickness is assumed to be identical for all particles. The partial structure factors $S_{\alpha\beta}(Q)$ are obtained from the analytical solution of the Percus-Yevick equation for an n -component mixture of hard spheres in combination with a multicomponent version of the Verlet-Weis correction.^{57,58} A model for the scattering cross section, given by eqn (1) as a product of form factor and measurable structure factor, can then directly be fitted to experimentally obtained intensities, as demonstrated in Fig. 1. The model shows excellent agreement with the experimental data and because of the unique combination of the features from both structure factor and form factor, the particle size distribution and the effective hard-sphere volume fraction can for each sample be accurately determined from the light scattering experiments, even with the restricted wavevector range compared to small-angle scattering, employing neutrons or X-rays as a probe.

Fig. 2 provides a more detailed depiction of the core-shell morphology of the particles. The radius of the PMMA core is independent of the effective volume fraction ϕ_{eff} and takes a mean value of (248 ± 3) nm for this particular sample. From the model fit, the polydispersity of the cores is determined to be approximately 7%. Unlike the particle cores, the thickness of the monodisperse shell is surprisingly observed to be affected by the particle concentration. At lower concentrations, the thickness has a limiting plateau value of (37 ± 5) nm, which is nearly independent of the volume fraction up to a critical value of $\phi_{\text{eff}} \approx 0.5$, after which the shell begins to shrink. In a highly concentrated glass-like suspension at $\phi_{\text{eff}} = 0.59$, the thickness is reduced to only (25 ± 2) nm. It is possible that the crowded environment in such dense particle suspensions



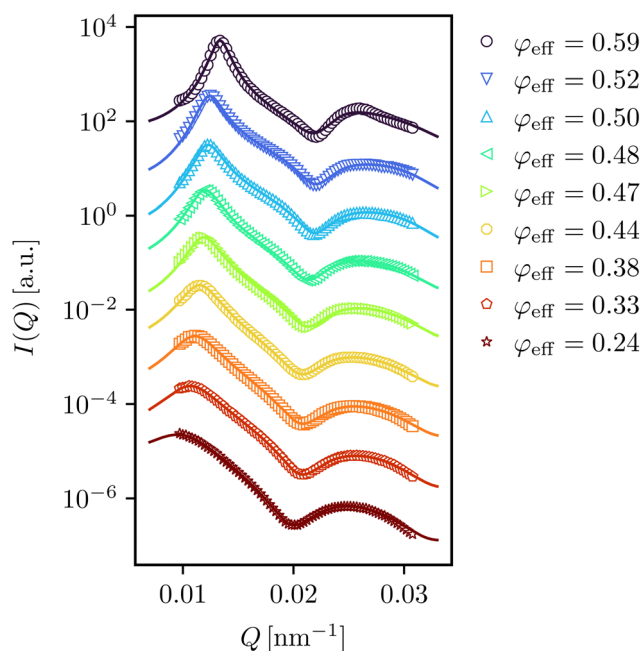


Fig. 1 Mean intensity $I(Q)$ of the investigated PMMA–PDMS particles, obtained by static light scattering, for effective hard-sphere volume fractions in a range from $0.24 < \varphi_{\text{eff}} < 0.59$, as indicated in the legend. The solid lines are the result of a least squares fit of the combined hard-sphere/core-shell model described in the text. For clarity of presentation, the curves are scaled by an arbitrary factor.

favours a more coiled conformation of the PDMS polymer chains. For a more detailed understanding of this behaviour, further investigations are required. As can be seen from the visual representation of the particle contrast at the top of Fig. 2, the effect is rather small when comparing the change in the shell thickness to the change of the total radius of the particles. In terms of the mean volume of a single particle, however, this still implies a decrease to about 88% of its initial volume, so the relationship between the particle number density and the volume fraction is noticeably nonlinear. For particles with even smaller cores in comparison to the shell, this effect is likely to be more prominent, especially when studying highly concentrated suspensions.

An upper bound for the shell thickness can be estimated from the fully elongated contour length of the PDMS-stabiliser.²⁹ If the functionalised stabiliser is approximated by a simple PDMS chain, where each repetition unit has a projected length of approximately 0.32 nm (taken from hexamethyldisiloxane in the gas phase⁵⁹) and a molar mass of 74 g mol^{-1} , the total molecular weight of $10\,000 \text{ g mol}^{-1}$ corresponds to a maximum possible length of 46 nm. The shell thickness estimated from the model fits is therefore realistic.

The extracted form factor $P(Q)$ of a dilute sample is depicted in Fig. 3, together with the corresponding radial profile of the scattering contrast. The form factor displays a somewhat uncommonly encountered shape, where the peak of the first local maximum exceeds the zero-wavevector limit. This is a result of the contrast matching procedure, where the refractive

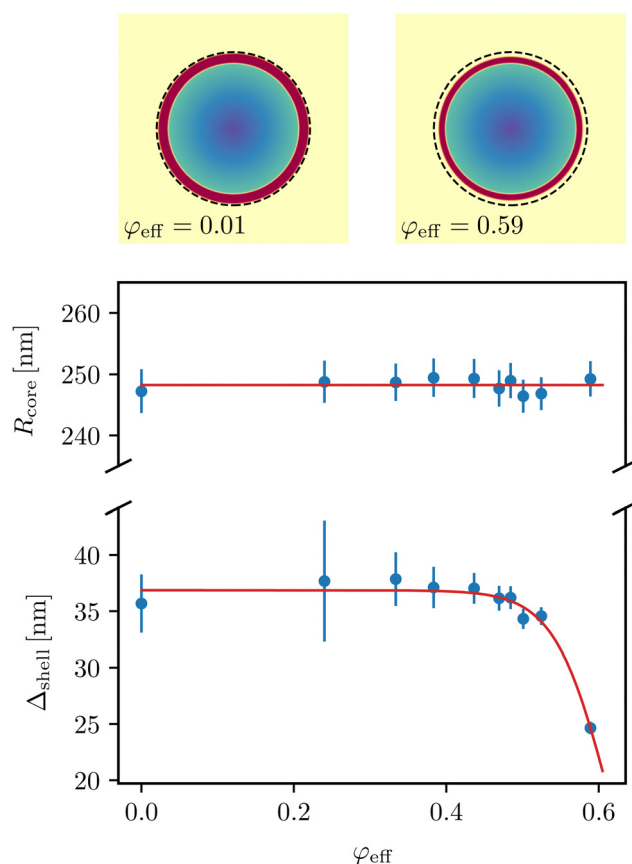


Fig. 2 Top: A false-color representation of the scattering contrast of the investigated particles to get an idea of the core-to-shell ratio in a dilute (left) and a concentrated sample (right). The dashed line indicates the contour of the particle in the dilute state. Bottom: The mean radius of the particle cores R_{core} and the thickness of the shell Δ_{shell} in dependence of the effective volume fraction φ_{eff} . The solid lines are a guide to the eye.

index of the decalin–tetralin solvent mixture is chosen to minimise the overall scattering of the suspension. This leads for the core-shell particles to a refractive index of the surrounding medium which lies between the index of the PDMS shell and the PMMA core, with a greatly reduced forward scattering contribution. The additional swelling causes a gradient of the refractive index inside the core, but does not qualitatively change the scattering pattern of the form factor. The relation between the different contrast contributions is better visualised in the contrast profile at the bottom of Fig. 3. It shows that the contrast of the shell to the suspending medium is similar in magnitude to the contrast between the core center and suspending medium, however, with opposite sign. Further, it reveals the extent of solvent permeation inside the PMMA core, where the contrast at the boundary between core and shell is almost halfway between the contrast of the core center and of the pure suspending medium.

Fig. 4 exemplarily displays the measurable structure factor $S_{\text{M}}(Q)$ of a concentrated suspension. $S_{\text{M}}(Q)$ is for polydisperse systems influenced by both the partial structure factors and the scattering amplitudes of all present species. A visualisation of $S_{\text{M}}(Q)$ is therefore mainly useful for the assessment of the fit



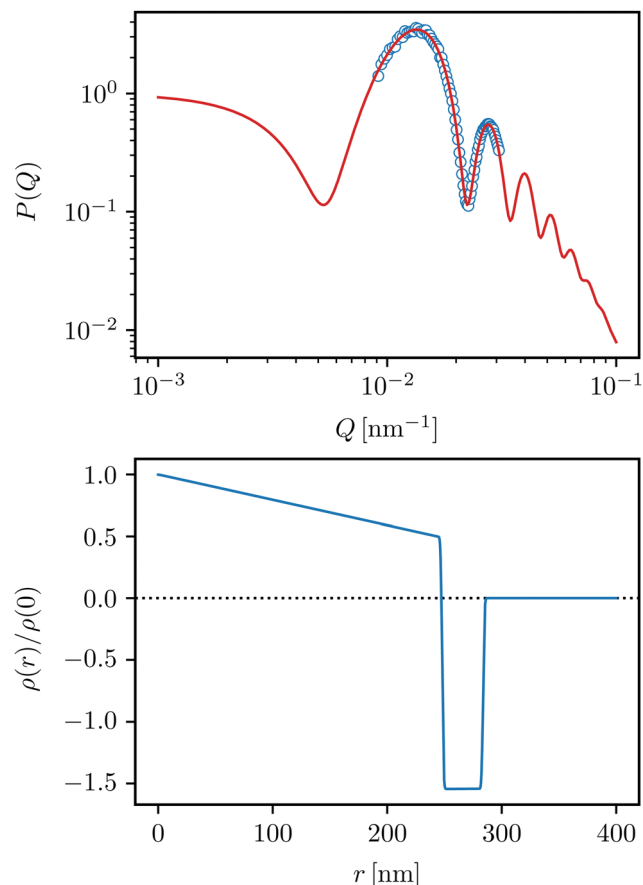


Fig. 3 Top: Extracted form factor $P(Q)$ of a dilute suspension of the investigated particles. The solid line is the form factor contribution of the employed model function which was fitted to the intensities in Fig. 1. From the extended wavevector-range, the characteristic scattering pattern of an index-matched core-shell particle is clearly visible. Bottom: Radial profile of the scattering contrast $\rho(r)$ in dependence on the distance r from the particle center, normalised to $\rho(0)$. The dotted line is a guide to the eye for the location of the solvent background $\rho_{\text{solv.}}(r) = 0$.

quality when comparing the experimental data and the theoretical prediction. A good agreement between the experimental data and the employed model is obvious and as such, the liquid-like suspension can be well described by an effective, polydisperse hard-sphere model within the Percus–Yevick theory. For comparison, the polydispersity-averaged total structure factor $S_{\text{tot}}(Q)$ and the structure factor of a corresponding monodisperse suspension with the same volume fraction are also shown. In the region around the main peak, $S_{\text{M}}(Q)$ and $S_{\text{tot}}(Q)$ behave very similarly, so for this particular model particle, the measurable structure factor provides a decent estimate of the ordering on length scales corresponding to the particle contact distance. The monodisperse structure factor overestimates the ordering as it neglects any polydispersity effects which generally diminish the peak height. Beyond the first maximum, $S_{\text{tot}}(Q)$ shows considerably stronger oscillations than $S_{\text{M}}(Q)$. The pronounced dampening of the oscillations in $S_{\text{M}}(Q)$ results mostly from the influence of the core-shell scattering amplitudes, the dampening resulting from

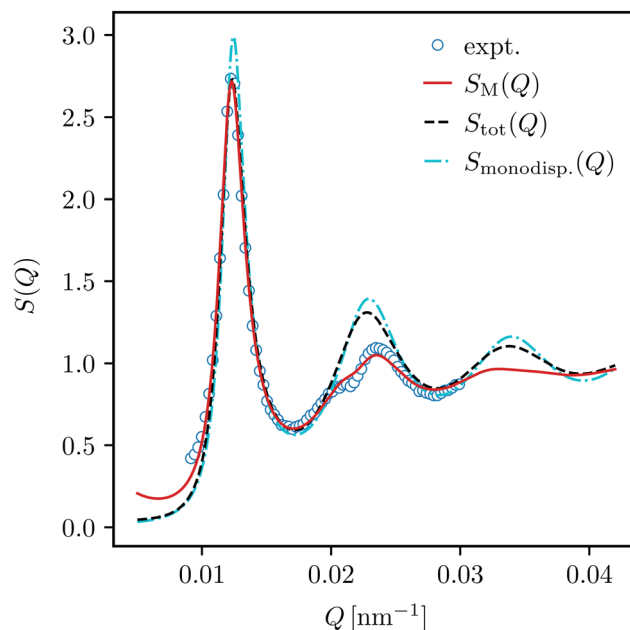


Fig. 4 Measurable structure factor $S_{\text{M}}(Q)$, exemplarily for a sample with an effective volume fraction of $\varphi_{\text{eff}} = 0.50$ and a mean radius of $R = 282$ nm. The solid line is the $S_{\text{M}}(Q)$ corresponding to the model fit to the intensities in Fig. 1, the dashed line represents the total structure factor $S_{\text{tot}}(Q)$ with the same partial structure factors and the dash-dotted line describes a monodisperse structure factor with the same radius and volume fraction.

the polydispersity on the other hand is much weaker, as is evident when comparing $S_{\text{tot}}(Q)$ to its monodisperse equivalent.

Dynamic light scattering experiments give access to the diffusional properties of the system. To analyse the short-time diffusion of the particles, the effective short-time diffusion coefficient $D_{\text{eff}}(Q)$ is obtained from the measurable intermediate scattering function $S_{\text{M}}(Q, t)$ using the cumulant method. In Fig. 5, $D_{\text{eff}}(Q)$, normalised to the apparent Stokes–Einstein diffusion coefficient $\overline{D}_0(Q)$, is displayed together with the experimental structure factor from Fig. 4. In accordance to the de Gennes relation [eqn (10)], $D_{\text{eff}}(Q)$ and $S_{\text{M}}(Q)$ show an alternating progression: The collective diffusion is decelerated on length scales with stable configurations, precisely where the local maxima of the structure factor occur.

The inverse relation, however, is not exact for this particular system, as the diffusion of the particles is not only influenced by their local interaction potential but also by indirect, hydrodynamic interactions mediated by diffusion-induced flow patterns in the suspending medium. With both $D_{\text{eff}}(Q)$ and $S_{\text{M}}(Q)$ known from independent experiments, the measurable hydrodynamic function $H_{\text{M}}(Q)$ is accessible. An exemplary visualisation of the resulting hydrodynamic function of a concentrated suspension is displayed in Fig. 6. It is possible to fully resolve the oscillating $H_{\text{M}}(Q)$ up to the second maximum and as expected for a hard-sphere system, the hydrodynamic interactions slow down the dynamics on all investigated length scales. The theoretical description of hydrodynamics in strongly interacting colloidal suspensions is still a very challenging task. We avoid a real multicomponent treatment of the hydrodynamic



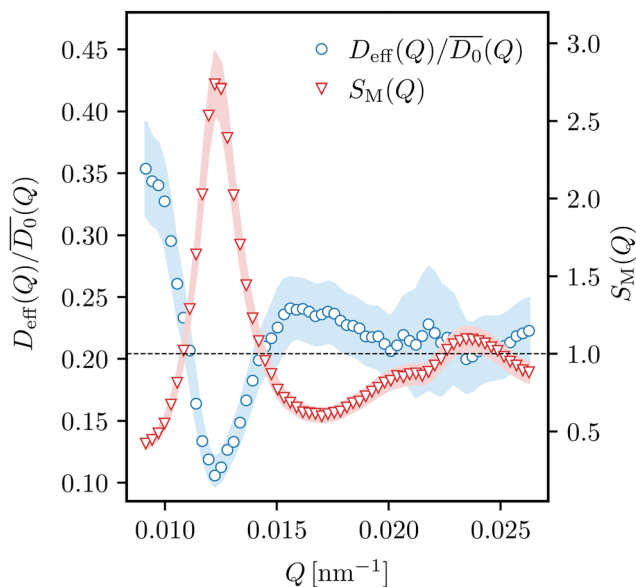


Fig. 5 Comparison between the normalised effective diffusion coefficient $D_{\text{eff}}(Q)/\overline{D}_0(Q)$ and the measurable structure factor $S_M(Q)$, for a suspension with effective volume fraction $\varphi_{\text{eff}} = 0.50$. The shaded area indicates the uncertainty of the experimental data. The dashed horizontal line is a guide to the eye for both $S_M(Q \rightarrow \infty) = 1$ and the location of the reduced self-diffusion coefficient $D_s/\overline{D}_0(Q \rightarrow \infty) \approx 0.21$.

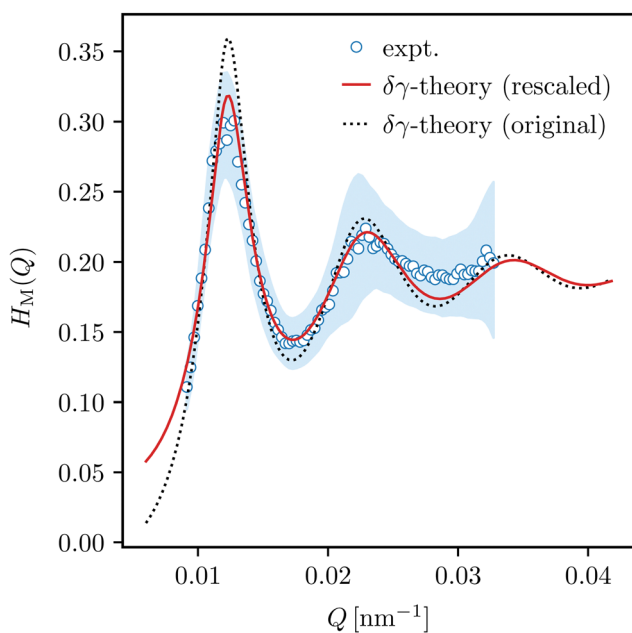


Fig. 6 Measurable hydrodynamic function $H_M(Q)$ of a suspension with an effective hard-sphere volume fraction of $\varphi_{\text{eff}} = 0.50$. The shaded area indicates the uncertainty of the experimental data. The dashed line is the theoretical prediction according to the original $\delta\gamma$ -theory while the solid line is the rescaled modification [eqn (17)].

interactions and prefer an effective one-component approach, which involves the $\delta\gamma$ -scheme proposed by Beenakker and Mazur.^{50,51} We choose the size-averaged total structure factor $S_{\text{tot}}(Q)$ to serve as the structure factor of a hypothetical

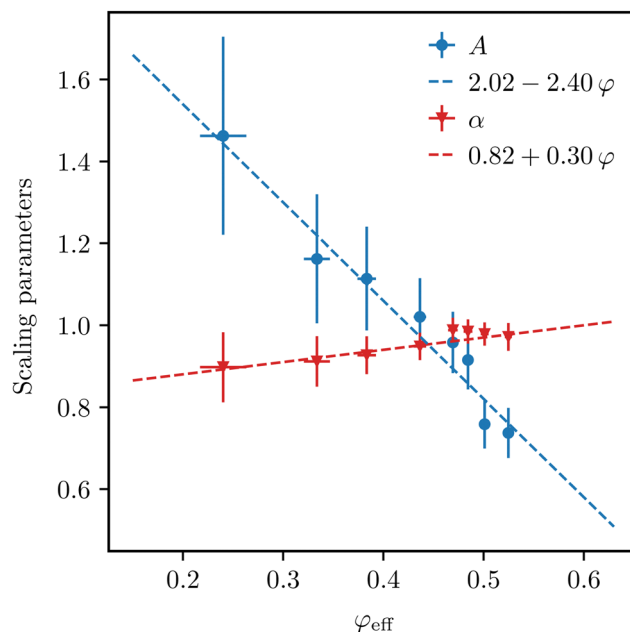


Fig. 7 The scaling parameters A and α from the rescaled $\delta\gamma$ -scheme introduced in the text in dependence on the effective volume fraction φ_{eff} . The dashed lines are linear least-squares fits, their fit parameters are indicated in the legend.

monodisperse system in hope that most of the polydispersity effects can be accounted for by the pre-averaging of this $S(Q)$. This input is then used to calculate the distinct part of the hydrodynamic function $H_d(Q)$ according to eqn (15). The self

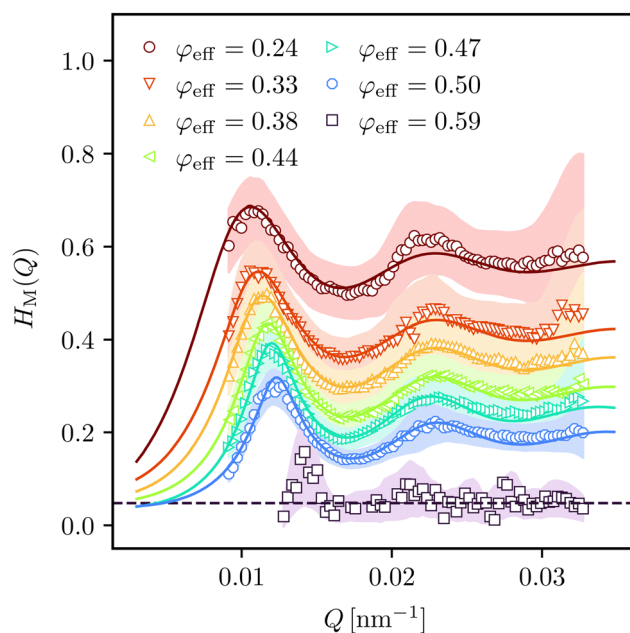


Fig. 8 Selected measurable hydrodynamic functions $H_M(Q)$ for effective hard-sphere volume fractions in a range from $0.24 < \varphi_{\text{eff}} < 0.59$, as indicated in the legend. The solid lines are results from the rescaled $\delta\gamma$ -theory described in the text. The shaded areas indicate the uncertainty of the experimental data. The horizontal dashed line is an estimate for the self part of $H(Q)$ for the glassy sample.



part D_s/D_0 is determined by a least-squares fit to the experimental data. The resulting prediction for $H_M(Q)$ is displayed in Fig. 6 as the dotted line and already shows a remarkably good agreement with the experiment. The general shape and especially the location of the main peak Q_m is reflected accurately, however, its amplitude is overestimated for this sample with $\varphi_{\text{eff}} = 0.50$ and, although much more subtly, there is a slight phase mismatch of the oscillation beyond the second maximum, which is more noticeable at lower effective volume fractions. As a further improvement, we decided to employ an empirical rescaling of the original $\delta\gamma$ - $H(Q)$. Similar rescaling procedures have previously been employed in conjunction with $\delta\gamma$ -theory, for example for studying solvent-permeable particles like microgels.^{60,61} The rescaled hydrodynamic function in our approach reads as

$$H_{\text{resc.}}(Q) = \frac{D_s}{D_0} + AH_d^{\delta\gamma}(Q^*), \quad (17)$$

with $Q^* = \alpha(Q - Q_m) + Q_m$. Besides the reduced self-diffusion coefficient D_s/D_0 as an adjustable parameter, two additional parameters are introduced: The factor A adjusts the height of the distinct part $H_d(Q)$ and the factor α scales the spatial frequency about Q_m so that the location of the principal peak remains constant. These two parameters are also determined

with a least-squares fit to the experimental $H_M(Q)$, so in total, three adjustable parameters are fitted simultaneously in our approach. The resulting curve is displayed in Fig. 6 as the solid line. The agreement of this rescaled $\delta\gamma$ -approach with the experimental data is excellent up until the second maximum. For larger Q , the deviation between experiment and theory is difficult to assess because of the high experimental uncertainty.

The volume-fraction dependence of the scaling parameters A and α of the rescaled $\delta\gamma$ -approach is displayed in Fig. 7. Both scaling factors can be parameterised, within experimental uncertainty, as a linear function. The two factors show opposing trends: α , which scales $H(Q)$ along the Q -axis, increases with higher volume fraction, whereas A , which scales the amplitude of $H(Q)$, decreases with rising φ_{eff} , with a much steeper slope. There exists a crossover region around $\varphi_{\text{eff}} \approx 0.45$ where both scaling factors are very similar and incidentally also close to unity. Thus, in this regime, the original $\delta\gamma$ -theory in conjunction with a fitted self-diffusion coefficient is already accurate without any rescaling. For volume fractions smaller than that, the height of the principal peak is underestimated by the original theory, while for larger φ_{eff} the peak height is overestimated instead. This is in accordance to results of a comparison between $\delta\gamma$ -theory and accelerated Stokesian dynamics simulations,⁵⁴ where the same trends are observed.

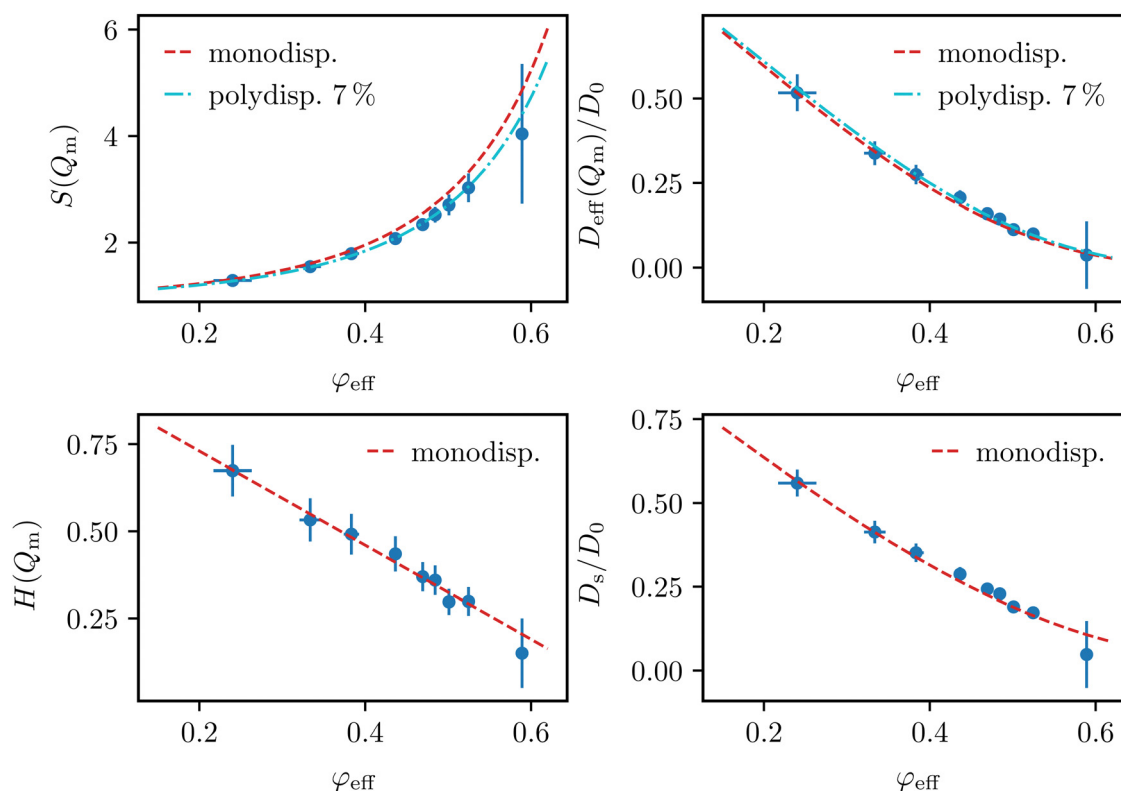


Fig. 9 Experimentally obtained characteristic properties in dependence on the effective hard-sphere volume fraction φ_{eff} with theoretical predictions from eqn (18). Top left: Principle peak height of the structure factor $S(Q_m)$, together with the theoretical predictions for monodisperse (dashed lines) and polydisperse (dashed-dotted lines) hard spheres. Bottom left: Hydrodynamic function $H(Q_m)$ at the structure factor main peak, together with the monodisperse prediction (dashed lines). Top right: Reduced effective diffusion coefficient $D_{\text{eff}}(Q_m)/D_0$, together with the monodisperse (dashed lines) and polydisperse (dashed-dotted lines) predictions, which are a combination of the theoretical curves from $S(Q_m)$ and $H(Q_m)$. Bottom right: Reduced self-diffusion coefficient D_s/D_0 , together with the monodisperse prediction (dashed lines).



Fig. 8 exemplarily shows selected extracted hydrodynamic functions together with the theoretical prediction from the introduced rescaled $\delta\gamma$ -scheme. The theory describes the experimental data well for all investigated volume fractions within experimental accuracy, which supports the success of the employed rescaling approach. In the glassy state at $\varphi_{\text{eff}} = 0.59$, practically no Q -dependence of the hydrodynamic function except a small maximum coinciding with the maximum of $S(Q)$ is observed. An estimate for the self part of $H(Q)$ is indicated by a dashed line.

From the experimental structure factors and hydrodynamic functions, the principal peak values $S(Q_m)$, $H(Q_m)$ and $D_{\text{eff}}(Q_m)$ can be extracted as characteristic properties, which, together with the reduced self-diffusion coefficient D_s/D_0 , can be readily compared to semi-empirical expressions from the literature:^{54,62}

$$S(Q_m) = 1 + 0.644\varphi \frac{1 - \varphi/2}{(1 - \varphi)^3}, \quad (18a)$$

$$H(Q_m) = 1 - 1.35\varphi, \quad (18b)$$

$$D_{\text{eff}}(Q_m) = D_0 \frac{H(Q_m)}{S(Q_m)}, \quad (18c)$$

$$\frac{D_s}{D_0} = 1 - 1.8315\varphi(1 + 0.1195\varphi - 0.70\varphi^2). \quad (18d)$$

The expressions are accurate at least up to the freezing transition of monodisperse hard spheres at $\varphi = 0.494$. The comparison between these theoretical predictions and experimental values [Fig. 9] therefore provides valuable insight into the influence of the particle polydispersity on these properties. As presumed, $S(Q_m)$ is overestimated by the expression for monodisperse spheres. It can instead be well described by the predictions of the multicomponent Percus–Yevick theory for hard spheres, as established previously. Altogether, all investigated properties follow closely the expected hard-sphere behavior. As a surprising observation, both $H(Q_m)$ and D_s/D_0 are well described by the predictions for monodisperse systems over the whole volume fraction range. The hydrodynamic interactions in this investigated system are therefore practically undisturbed by the moderate polydispersity. The effective diffusion coefficient $D_{\text{eff}}(Q_m)$ results from the combination of potential and hydrodynamic interactions. Looking at the two possible theoretical descriptions, depending on whether the monodisperse or the multicomponent expression for $S(Q_m)$ is used for the structural part, it is evident that the polydispersity only causes minimal deviations in the volume-fraction dependence of the diffusion coefficient. Variations in $H(Q_m)$ on the other hand would have a much more pronounced effect.

5 Conclusions

Colloidal PMMA particles grafted with PDMS-stabilisers are a promising alternative for established PMMA–PHSA particles. With the combination of MMA as monomer and PDMS which is commercially available with defined molecular weight and thus

chain length, in a dispersion polymerisation reaction, particles with tunable size of PMMA-core and PDMS-shell are accessible in a reproducible way with acceptable polydispersity.

Self-organisation of these PMMA–PDMS particles leads to liquid-like ordered colloidal suspensions whose structural and dynamic properties are investigated employing static and dynamic light scattering. Start values for the topological parameters of the particles are determined *via* static light scattering experiments with highly-diluted suspensions with neglectable particle interactions and thus uncorrelated particles. The scattering function of single particles or form factor can be described employing a core–shell model with a gradient of scattering length density in the PMMA-core induced by swelling in the index-matched suspending medium. With the form factor, regarding the size-distribution of the ensemble, the scattered intensity resulting from liquid-like ordered systems can quantitatively be described in the whole range of volume fractions up to the glass transition employing a Percus–Yevick ansatz for polydisperse hard spheres. Hence, the structure of self-organised systems can quantitatively be described employing hard-sphere interactions.

Since dynamic properties are even more sensitive to particle interactions, we investigated collective diffusion by means of dynamic light scattering experiments. Hydrodynamic functions are determined from the intermediate scattering functions, structure factors and polydispersity-weighted Einstein diffusion coefficients. The determined hydrodynamic functions can in the whole range of volume fractions investigated accurately be modeled using a rescaled $\delta\gamma$ -scheme based on hard-sphere interactions. Using a polydisperse Percus–Yevick ansatz, not only the principal peak of the hydrodynamic function, but also beyond its second maximum can for the first time quantitatively be described within experimental uncertainties. Also the amplitudes $S(Q_m)$ and $H(Q_m)$ of structure factor and hydrodynamic function as well as the reduced short-time self diffusion coefficient D_s/D_0 are in excellent agreement to predictions for hard-sphere systems. Hence, in addition to the structure, also the dynamic properties can quantitatively be described using a hard-sphere model. In conclusion, the PMMA–PDMS system is not only a comparatively easy accessible, but also a highly suitable hard-sphere model system.

Small-angle X-ray and neutron scattering experiments with practically no limitation with respect to Q_{max} are promising experiments giving access to the shell structure with enlarged spatial resolution. Since optical index matching is not mandatory for these techniques, apolar suspending media leading to higher contrast can facilitate such experiments. Herewith, additional insights to the mechanism of sterical stabilisation and shrinking of the shell thickness at high volume fractions can be expected. Static and dynamic X-ray scattering experiments such as X-ray photon correlation spectroscopy (XPCS) would also enable the investigation of systems with comparable size of core diameter and shell thickness, where the validity of a simple hard-sphere description is still an open question.

Further investigations on dynamics of glassy systems and rheological properties of liquid-like structured and glassy



systems are promising remaining tasks. A certain degree of polydispersity is needed to stabilise metastable glassy systems in order to prevent crystallisation. Since for these systems with still acceptable polydispersity, structural and dynamic properties can quantitatively be modeled by theoretical approaches regarding their size distribution, they are promising, comparatively easy accessible systems to systematically investigate structure-dynamics relations in colloidal glasses combining theory such as the mode coupling scheme and experiment. The availability of accurate experimental data can stimulate the development of theoretic approaches for glass dynamics and hydrodynamics rigorously taking polydispersity at high volume fractions into account which would also improve the prediction of macroscopic, rheological properties.

Author contributions

J. Diaz Maier: conceptualisation, data curation, formal analysis, investigation, methodology, software, validation, visualisation, writing – original draft. J. Wagner: conceptualisation, methodology, project administration, resources, supervision, validation, writing – review & editing.

Conflicts of interest

There are no conflicts to declare.

Notes and references

- J. G. Kirkwood and E. M. Boggs, *J. Chem. Phys.*, 1942, **10**, 394–402.
- B. Widom, *Science*, 1967, **157**, 375–382.
- P. N. Pusey and W. van Meegen, *Nature*, 1986, **320**, 340–342.
- P. N. Pusey and W. van Meegen, *Phys. Rev. Lett.*, 1987, **59**, 2083–2086.
- S.-E. Phan, W. B. Russel, Z. Cheng, J. Zhu, P. M. Chaikin, J. H. Dunsmuir and R. H. Ottewill, *Phys. Rev. E: Stat. Phys., Plasmas, Fluids, Relat. Interdiscip. Top.*, 1996, **54**, 6633–6645.
- D. J. Cebula, J. W. Goodwin, R. H. Ottewill, G. Jenkin and J. Tabony, *Colloid Polym. Sci.*, 1983, **261**, 555–564.
- A. Moussaïd and P. N. Pusey, *Phys. Rev. E: Stat. Phys., Plasmas, Fluids, Relat. Interdiscip. Top.*, 1999, **60**, 5670–5676.
- A. van Blaaderen and P. Wiltzius, *Science*, 1995, **270**, 1177–1179.
- C. P. Royall, A. A. Louis and H. Tanaka, *J. Chem. Phys.*, 2007, **127**, 044507.
- S. Kale, A. Lederer, M. Oettel and H. J. Schöpe, *Soft Matter*, 2023, **19**, 2146–2157.
- W. van Meegen, S. M. Underwood, R. H. Ottewill, N. S. J. Williams and P. N. Pusey, *Faraday Discuss. Chem. Soc.*, 1987, **83**, 47–57.
- R. H. Ottewill and N. S. J. Williams, *Nature*, 1987, **325**, 232–234.
- X. Qiu, X. L. Wu, J. Z. Xue, D. J. Pine, D. A. Weitz and P. M. Chaikin, *Phys. Rev. Lett.*, 1990, **65**, 516–519.
- P. N. Segrè, O. P. Behrend and P. N. Pusey, *Phys. Rev. E: Stat. Phys., Plasmas, Fluids, Relat. Interdiscip. Top.*, 1995, **52**, 5070–5083.
- Z. Cheng, P. M. Chaikin, J. Zhu, W. B. Russel and W. V. Meyer, *Phys. Rev. Lett.*, 2001, **88**, 015501.
- S.-E. Phan, W. B. Russel, J. Zhu and P. M. Chaikin, *J. Chem. Phys.*, 1998, **108**, 9789–9795.
- W. van Meegen and S. M. Underwood, *Phys. Rev. E: Stat. Phys., Plasmas, Fluids, Relat. Interdiscip. Top.*, 1993, **47**, 248–261.
- W. van Meegen and S. M. Underwood, *Phys. Rev. E: Stat. Phys., Plasmas, Fluids, Relat. Interdiscip. Top.*, 1994, **49**, 4206–4220.
- W. van Meegen, T. C. Mortensen, S. R. Williams and J. Müller, *Phys. Rev. E: Stat. Phys., Plasmas, Fluids, Relat. Interdiscip. Top.*, 1998, **58**, 6073–6085.
- M. Leocmach and H. Tanaka, *Nat. Commun.*, 2012, **3**, 974.
- J. E. Hallett, F. Turci and C. P. Royall, *Nat. Commun.*, 2018, **9**, 3272.
- F. Lehmkuhler, B. Hankiewicz, M. A. Schroer, L. Müller, B. Ruta, D. Sheyfer, M. Sprung, K. Tono, T. Katayama, M. Yabashi, T. Ishikawa, C. Gutt and G. Grübel, *Sci. Adv.*, 2020, **6**, eabc5916.
- C. P. Royall, J. Dzubiella, M. Schmidt and A. van Blaaderen, *Phys. Rev. Lett.*, 2007, **98**, 188304.
- P. Ballesta, R. Besseling, L. Isa, G. Petekidis and W. C. K. Poon, *Phys. Rev. Lett.*, 2008, **101**, 258301.
- E. Di Cola, A. Moussaïd, M. Sztucki, T. Narayanan and E. Zaccarelli, *J. Chem. Phys.*, 2009, **131**, 144903.
- L. Antl, J. W. Goodwin, R. D. Hill, R. H. Ottewill, S. M. Owens, S. Papworth and J. A. Waters, *Colloids Surf.*, 1986, **17**, 67–78.
- M. T. Elsesser and A. D. Hollingsworth, *Langmuir*, 2010, **26**, 17989–17996.
- L. Palangetic, K. Feldman, R. Schaller, R. Kalt, W. R. Caseri and J. Vermant, *Faraday Discuss.*, 2016, **191**, 325–349.
- J. E. Hallett, I. Grillo and G. N. Smith, *Langmuir*, 2020, **36**, 2071–2081.
- S. M. Klein, V. N. Manoharan, D. J. Pine and F. F. Lange, *Colloid Polym. Sci.*, 2003, **282**, 7–13.
- A. P. Richez, L. Farrand, M. Goulding, J. H. Wilson, S. Lawson, S. Biggs and O. J. Cayre, *Langmuir*, 2014, **30**, 1220–1228.
- H. Tsurusawa, J. Russo, M. Leocmach and H. Tanaka, *Nat. Mater.*, 2017, **16**, 1022–1028.
- H. Tsurusawa, M. Leocmach, J. Russo and H. Tanaka, *Sci. Adv.*, 2019, **5**, eaav6090.
- H. Tsurusawa, S. Arai and H. Tanaka, *Sci. Adv.*, 2020, **6**, eabb8107.
- M. Tateno, T. Yanagishima and H. Tanaka, *J. Chem. Phys.*, 2022, **156**, 084904.
- H. Tsurusawa and H. Tanaka, *Nat. Phys.*, 2023, **19**, 1171–1177.
- N. H. P. Orr, T. Yanagishima, E. Maire and R. P. A. Dullens, *Phys. Rev. Mater.*, 2021, **5**, 123605.
- T. Lin, T. E. Kodger and D. A. Weitz, *Soft Matter*, 2013, **9**, 5173–5177.



- 39 P. N. Pusey, in *Liquids, Freezing and Glass Transition*, ed. J. Z.-J. J. P. Hansen and D. Levesque, North-Holland, Amsterdam, 1991, pp. 765–942.
- 40 A. Vrij, *J. Chem. Phys.*, 1978, **69**, 1742–1747.
- 41 A. Vrij, *J. Chem. Phys.*, 1979, **71**, 3267–3270.
- 42 L. Blum and G. Stell, *J. Chem. Phys.*, 1979, **71**, 42–46.
- 43 L. Blum and G. Stell, *J. Chem. Phys.*, 1980, **72**, 2212.
- 44 G. Schulz, *Z. Phys. Chem.*, 1949, **46**, 155–193.
- 45 J. Wagner, *J. Appl. Crystallogr.*, 2012, **45**, 513–516.
- 46 B. D'Aguzzo and R. Klein, *Phys. Rev. A: At., Mol., Opt. Phys.*, 1992, **46**, 7652–7656.
- 47 B. D'Aguzzo, *Phys. Scr.*, 1993, **1993**, 84.
- 48 B. J. Berne and R. Pecora, *Dynamic light scattering: with applications to chemistry, biology and physics*, Dover Publications, 1976.
- 49 J.-P. Hansen and I. R. McDonald, *Theory of simple liquids: with applications to soft matter*, Academic Press, 2013.
- 50 C. W. J. Beenakker and P. Mazur, *Phys. A*, 1983, **120**, 388–410.
- 51 C. W. J. Beenakker and P. Mazur, *Phys. A*, 1984, **126**, 349–370.
- 52 U. Genz and R. Klein, *Phys. A*, 1991, **171**, 26–42.
- 53 J. Gapinski, A. Wilk, A. Patkowski, W. Häußler, A. J. Banchio, R. Pecora and G. Nägele, *J. Chem. Phys.*, 2005, **123**, 054708.
- 54 A. J. Banchio and G. Nägele, *J. Chem. Phys.*, 2008, **128**, 104903.
- 55 M. Heinen, P. Holmqvist, A. J. Banchio and G. Nägele, *J. Appl. Crystallogr.*, 2010, **43**, 970–980.
- 56 W. B. Russel, P. M. Chaikin, J. Zhu, W. V. Meyer and R. Rogers, *Langmuir*, 1997, **13**, 3871–3881.
- 57 L. Verlet and J.-J. Weis, *Phys. Rev. A: At., Mol., Opt. Phys.*, 1972, **5**, 939–952.
- 58 E. W. Grundke and D. Henderson, *Mol. Phys.*, 1972, **24**, 269–281.
- 59 K. B. Borisenko, B. Rozsondai and I. Hargittai, *J. Mol. Struct.*, 1997, **406**, 137–144.
- 60 G. C. Abade, B. Cichocki, M. L. Ekiel-Jeżewska, G. Nägele and E. Wajnryb, *J. Chem. Phys.*, 2010, **132**, 014503.
- 61 J. Riest, T. Eckert, W. Richtering and G. Nägele, *Soft Matter*, 2015, **11**, 2821–2843.
- 62 M. Heinen, A. J. Banchio and G. Nägele, *J. Chem. Phys.*, 2011, **135**, 154504.



Publication III

Measurable structure factors of dense dispersions containing polydisperse, optically inhomogeneous particles

J. Diaz Maier, K. Gaus and J. Wagner

J. Appl. Crystallogr. **57**, 1503–1513 (2024)

<https://doi.org/10.1107/S1600576724007957>

Open-access article distributed under the terms of the Creative Commons Attribution 4.0 International (CC-BY 4.0) License.

Contribution:

I conceptualized this work together with J.W. I implemented the software, K.G. analyzed the models under my supervision, I performed supporting calculations, aided in creating visualizations and wrote the original draft. The manuscript was revised by all authors.

My approximated contribution to the publication in percent: 60 %



Measurable structure factors of dense dispersions containing polydisperse optically inhomogeneous particles

Joel Diaz Maier, Katharina Gaus and Joachim Wagner*

Institut für Chemie, Universität Rostock, 18051 Rostock, Germany. *Correspondence e-mail: joachim.wagner@uni-rostock.de

Received 14 February 2024
Accepted 12 August 2024

Edited by E. P. Gilbert, Australian Centre for Neutron Scattering, ANSTO, Australia

Keywords: small-angle scattering; contrast variation; structure factors; hard-sphere interaction; dense dispersions; polydisperse particles; optical inhomogeneities; size distributions.

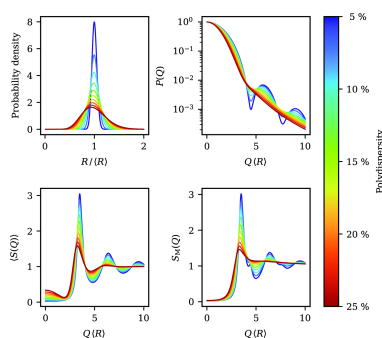
Here, it is investigated how optical properties of single scatterers in interacting multi-particle systems influence measurable structure factors. Both particles with linear gradients of their scattering length density and core-shell structures evoke characteristic deviations between the weighted sum $\langle S(Q) \rangle$ of partial structure factors in a multi-component system and experimentally accessible measurable structure factors $S_M(Q)$. While $\langle S(Q) \rangle$ contains only the structural information of self-organizing systems, $S_M(Q)$ is additionally influenced by the optical properties of their constituents, resulting in features such as changing amplitudes, additional peaks in the low-wavevector region or splitting of higher-order maxima, which are not related to structural reasons. It is shown that these effects can be systematically categorized according to the qualitative behaviour of the form factor in the Guinier region, which enables assessing the suitability of experimentally obtained structure factors to genuinely represent the microstructure of complex systems free from any particular model assumption. Hence, a careful data analysis regarding size distribution and optical properties of single scatterers is mandatory to avoid a misinterpretation of measurable structure factors.

1. Introduction

Colloidal dispersions attract wide interest in condensed matter physics as highly tunable model systems, mimicking atoms and molecules on the much larger mesoscopic scale with typical length scales between 10 and 1000 nm. Studying these systems enabled major advances in the comprehension of the characteristics of simple fluids and solids, which stimulated the progress of significant theoretical developments towards the understanding of complex systems and materials (Lu & Weitz, 2013).

Scattering experiments serve as essential methods for structural and dynamical investigations in colloidal many-particle systems (Li *et al.*, 2016). Small-angle scattering (SANS with neutrons or SAXS with X-rays as a probe) enables the characterization of colloidal suspensions across the entire range of relevant scattering vector magnitudes Q (Glatter, 2018). By employing visible light, which is also a natural choice since its wavelength is of the same order of magnitude as the typical size of a colloidal particle, the same type of analysis is in principle also possible in a simpler laboratory setup. This is however connected with the cost of a limited resolution and, as a consequence thereof, the restriction to comparatively large structures (Bohren & Huffman, 2008).

In non-interacting systems, the positions and orientations of the colloidal particles are completely uncorrelated. Thus, the scattered intensity results solely from the superposition of the



OPEN ACCESS

Published under a CC BY 4.0 licence

scattering functions of the single constituents. However, when the particles do interact, higher-level structures emerge from inherent self-organization due to interparticle forces, such as electrostatic and steric interactions or van der Waals attractions. The intensity is then influenced both by the optical properties of the scatterers themselves and by the spatial correlations between them. For idealized radially symmetric and monodisperse systems, where all particles are assumed to be identical, the two contributions can be rigorously separated into the form factor $P(Q)$, containing the single-particle properties, and the structure factor $S(Q)$, which encodes the structural correlations, employing the well known factorization $I(Q) \propto P(Q) S(Q)$ (Hansen *et al.*, 1991).

Realistic dispersions typically exhibit a distribution of characteristics, prominently through particle size. In polydisperse interacting systems, the characterization via scattering experiments is in general significantly more complicated, as the factorization of the intensity into form factor and structure factor can no longer be employed in a straightforward way (Salgi & Rajagopalan, 1993). Additionally, the observed diffraction patterns become increasingly featureless for broader size distributions, further obstructing the interpretation of experimental intensities. The analysis of multi-component systems thus requires a thorough understanding of the underlying distributions of scattering properties and particle interactions. Insights can be gained through contrast-variation techniques (Ballauff, 2001); selectively altering the contrast between specific particle types or between particles and the surrounding medium allows for the isolation and probing of distinct species, aiding the validation of theoretical models.

From an experimental standpoint, it is useful to analyse the measurable structure factor $S_M(Q)$, which is defined in such a way that the factorization property $I(Q) \propto P(Q) S_M(Q)$ is also recovered in the polydisperse case (Hansen *et al.*, 1991). $S_M(Q)$ is comparatively easy to access experimentally from the ratio between the intensities of an interacting suspension and a highly diluted non-interacting one. It is as such also widely used as a measure for structural correlations in polydisperse systems, where the height of the principal peak is especially well established as an order parameter (Banchio *et al.*, 1998). Under specific circumstances, this type of analysis can however turn into a serious pitfall: $S_M(Q)$ is also fundamentally affected by optical properties of the particles and not only by their interactions (Salgi & Rajagopalan, 1993).

For certain types of dispersions, some simplifying assumptions can be employed. In dilute suspensions of strongly interacting charged particles, for example, the interparticle distances typically are about an order of magnitude larger than the particle sizes because of the large electrostatic repulsion (Hayter & Penfold, 1981). In such a case, the correlation between the particle positions and the scattering amplitudes can be neglected. This neglect of correlations leads to the ‘decoupling approximation’, under which $S_M(Q)$ can be decomposed into a structure factor that genuinely represents the averaged structural correlations and weighting factors solely dependent on the scattering amplitudes (Pusey *et al.*,

1982; Kotlarchyk & Chen, 1983). This type of analysis was also recently used in a SANS study of moderately concentrated poly(*N*-isopropylacrylamide) microgels (Zhou *et al.*, 2023), where again the importance of an accurate treatment of polydispersity was stressed. Non-spherical particles cause effects in scattering patterns that appear quite similar to those introduced by size dispersity in systems of spherical particles (Pusey *et al.*, 1982). These effects can to a certain degree also be treated within the decoupling approximation (Kotlarchyk & Chen, 1983), whose range of validity has been extensively characterized (Greene *et al.*, 2016). In highly concentrated suspensions, where particles are in close contact, the accuracy of the decoupling approximation is strongly diminished, as in these systems the correlation lengths of the particles’ centres of mass are comparable to the correlation lengths inside the particles themselves (Pedersen, 1997). At such high particle volume fractions, excluded volume effects are the predominant contribution to the total interaction potential.

The fundamental interactions in dense colloidal dispersions consisting of spherical particles can to a good approximation be theoretically described with the hard-sphere model (Kirkwood & Boggs, 1942; Widom, 1967). The radial distribution functions of an n -component mixture of hard spheres can be calculated within the Percus–Yevick closure of the Ornstein–Zernike equation (Percus & Yevick, 1958) using Baxter’s technique (Baxter, 1970), giving access to the corresponding partial structure factors (Vrij, 1978, 1979; Blum & Stell, 1979, 1980). Building on Vrij’s work (Vrij, 1979; van Beurten & Vrij, 1981), Griffith *et al.* (1987) presented an analytical scattering function of a polydisperse hard-sphere fluid with a Schulz–Flory distribution (Flory, 1936; Schulz, 1939) of particle diameters. Despite their helpfulness, these expressions are not widely used because of their perceived complexity. Nayeri *et al.* (2009) later extended this approach to core–shell structured hard spheres and used their expressions to describe experimental intensities of a hard-sphere-like microemulsion system. Only recently, Botet *et al.* (2020) provided expressions for $S_M(Q)$ in a simple accessible form and for a number of commonly encountered size distributions. Their analytical expressions are valid for hard optically homogeneous spheres.

This resurgence of interest is an incentive to systematically examine how different form-factor models affect the characteristics of measurable structure factors. It is a well known fact that, especially in dense dispersions, $S_M(Q)$ is generally not equal to the structure factor $\langle S(Q) \rangle$ representing the averaged spatial correlations of the entire system (Salgi & Rajagopalan, 1993; Frenkel *et al.*, 1986). The mismatch between $S_M(Q)$ and $\langle S(Q) \rangle$ is precisely the reason why in many past studies an extraction of $S_M(Q)$ is deliberately not attempted. By describing the scattered intensity of concentrated suspensions with sophisticated models, a thorough characterization of particle properties is possible without calculating $S_M(Q)$, as performed, for example, by Stieger, Pedersen *et al.* (2004); Stieger, Richtering *et al.* (2004); Zackrisson *et al.* (2005); Balogh *et al.* (2007); or Scotti (2021).

Certainly, however, for many applications in condensed matter science, gaining an accurate approximation of the

structure factor is still highly desired. This is especially the case when employing computer simulations or many-body theory to model structural phenomena and wanting to compare detailed facets of particle self-organization directly with experimental outcomes (Dekker *et al.*, 2020; Peláez-Fernández *et al.*, 2011; Anta & Madden, 1999; Krause *et al.*, 1991; Stellbrink *et al.*, 2002). Beyond using structure factors to deduct structural patterns from experimental scattering data (Mohanty *et al.*, 2017; Phalakornkul *et al.*, 1996; Scheffold & Mason, 2009; Mason *et al.*, 2006), these quantities are used in theoretical approaches to calculate short- and long-time dynamics in many-particle systems. Two notable examples in this context are the $\delta\gamma$ -expansion by Beenakker & Mazur (1983, 1984) used to model hydrodynamic effects during short-time diffusion (Genz & Klein, 1991) and the widely known mode-coupling theory of the glass transition (Janssen, 2018), which both need the static structure factor as an input for calculations. In these theories, a popular method is to circumvent computationally expensive multi-component calculations by considering an effective one-component analysis using the experimentally obtained structure factor $S_M(Q)$ directly, assuming this quantity to be an accurate representation of the average structure factor $\langle S(Q) \rangle$ (Robert *et al.*, 2008; Di Cola *et al.*, 2009).

For a number of specialized cases, deviations between $\langle S(Q) \rangle$ and $S_M(Q)$ and the general influence of varying optical properties on $S_M(Q)$ have already been assessed (Banchio *et al.*, 1998; Pedersen, 2001). The purpose of this contribution is to raise further awareness on how particles' optical properties influence the shape of $S_M(Q)$ while the underlying interactions remain unchanged and to show that these observations can be model-independently systematized on the basis of quite universal principles. This enables practitioners to make informed judgements under which circumstances such an experimentally obtained structure factor can still serve as a valid order parameter. We show typical examples of shapes that can be realistically encountered during contrast-variation experiments, so even without explicitly employing established theoretical models [see *e.g.* Pedersen (1997) for a large collection of scattering functions], a qualitative assessment of experimental findings is possible. We also analyse two simplified models for optically inhomogeneous particles: those with a linear gradient of the scattering contrast and spheres with a core-shell structure. Nevertheless, the approach is readily adaptable to any model and provides a toolbox for the modelling of measurable structure factors for hard-sphere suspensions with arbitrary form factors, as demonstrated in several past studies (Vrij, 1979; Frenkel *et al.*, 1986; Pedersen, 2001; Nayeri *et al.*, 2009; Botet *et al.*, 2020; Diaz Maier & Wagner, 2024).

2. Scattering of hard-sphere mixtures

We consider a mixture of spherical particles, where each particle can be categorized into one of n species. The composition of the mixture is specified by the number fractions $x_\alpha = N_\alpha/N$, where N is the total number of particles and

N_α is the number of particles belonging to species α . We further restrict ourselves to elastic single scattering events where the Born approximation is applicable. In such a case, the mean intensity

$$I(Q) \propto \sum_{\alpha,\beta} (x_\alpha x_\beta)^{1/2} f_\alpha(Q) f_\beta(Q) S_{\alpha\beta}(Q) \quad (1)$$

is proportional to the weighted sum of the single-particle scattering amplitudes $f_\alpha(Q)$ and the partial structure factors $S_{\alpha\beta}(Q)$ (Salgi & Rajagopalan, 1993). Herein, the scattering amplitude

$$f_\alpha(Q) = 4\pi \int_0^\infty \rho_\alpha(r) r^2 \frac{\sin(Qr)}{Qr} dr \quad (2)$$

is the Fourier–Bessel transform of the scattering contrast $\rho_\alpha(r)$, whereas the partial structure factors $S_{\alpha\beta}(Q)$ are obtained from the solution of the multi-component Ornstein–Zernike equation. Expressions for $S_{\alpha\beta}(Q)$ of the hard-sphere fluid within the Percus–Yevick closure are given by Vrij (1979) but, for the convenience of the reader, the solution is re-articulated in Appendix A, and presented in a manner that is accessible and easily applicable. This genuine multi-component approach involving partial structure factors is a general and versatile formalism, from which both the decoupling approximation (Kotlarchyk & Chen, 1983) and the local monodisperse approximation (Pedersen, 1994), serving as a localized effective one-component approach suited for very polydisperse systems, can be derived.

For non-interacting particles, the partial structure factors are simply $S_{\alpha\beta}(Q) = \delta_{\alpha\beta}$, where $\delta_{\alpha\beta}$ denotes the Kronecker symbol. Equation (1) then reduces to the size average of the squared scattering amplitudes,

$$I(Q) \propto \langle f^2(Q) \rangle = \sum_\alpha x_\alpha f_\alpha^2(Q). \quad (3)$$

The average form factor

$$P(Q) = \frac{\langle f^2(Q) \rangle}{\langle f^2(0) \rangle} \quad (4)$$

is familiarly obtained from the normalization to forward scattering. As the measurable structure factor should satisfy the relation $I(Q) \propto P(Q) S_M(Q)$, the expression

$$S_M(Q) = [\langle f^2(Q) \rangle]^{-1} \sum_{\alpha,\beta} (x_\alpha x_\beta)^{1/2} f_\alpha(Q) f_\beta(Q) S_{\alpha\beta}(Q) \quad (5)$$

results from the combination of equations (1) and (3). The averaged structure factor

$$\langle S(Q) \rangle = \sum_{\alpha,\beta} (x_\alpha x_\beta)^{1/2} S_{\alpha\beta}(Q) \quad (6)$$

provides information about the total spatial correlations between all present particles, regardless of their species labels. It represents a true thermodynamic average independent of any optical properties. Any deviation between $S_M(Q)$ and $\langle S(Q) \rangle$ is thus a measure for the perturbation of $\langle S(Q) \rangle$ caused by the scattering amplitudes.

We now want to explore the influence of the scattering amplitudes on the shape of $S_M(Q)$. The aim is to gain a qualitative understanding of generic patterns; so to keep the analysis tractable, only a single representative size distribution is considered. For this purpose, the Schulz–Flory distribution with probability density

$$c(R) = \frac{1}{\Gamma(Z+1)} \left(\frac{Z+1}{\langle R \rangle} \right)^{Z+1} R^Z \exp\left(-\frac{Z+1}{\langle R \rangle} R\right) \quad (7)$$

is chosen. Here, R is the particle radius with mean $\langle R \rangle$ and $\Gamma(x)$ represents the gamma function. The polydispersity p of the system is specified by the shape parameter Z via $p^2 = (\langle R^2 \rangle - \langle R \rangle^2) / \langle R \rangle^2 = 1 / (Z + 1)$. The idea is now to discretize the distribution to a representative n -component mixture. For the Schulz–Flory distribution, an efficient way to achieve this is by exploiting the generalized Gauss–Laguerre quadrature rule, specifically used to calculate integrals with a weighting function like equation (7) (D’Aguanno & Klein, 1992; D’Aguanno, 1993; Olver *et al.*, 2010). The nodes and weights generated by such a procedure are equivalent to the particle radii and number fractions of a discrete mixture which shares the first $2n - 1$ moments $\langle R^n \rangle$ with the original continuous distribution. For each calculated scattering function, we carefully checked that the number of nodes necessary for convergence was reached. The numerical scheme was

further tested against the analytical $S_M(Q)$ for homogeneous spheres provided by Botet *et al.* (2020), where excellent agreement was found.

3. Measurable structure factors of polydisperse systems

3.1. General remarks

Fig. 1 provides a general introductory overview of the influence of polydispersity on $P(Q)$, $S_M(Q)$ and $\langle S(Q) \rangle$, discussed for a dense suspension of homogeneous spheres, serving as a reiteration of well known phenomenology (Botet *et al.*, 2020). Concerning the form factors, only those corresponding to polydispersities of less than 10% appear structured. Familiarly, the characteristic minima in $P(Q)$ become increasingly smeared out for broader size distributions.

Polydispersity also causes a change in the initial slope of $P(Q)$ in the Guinier region. Reflecting the distribution of particle sizes when calculating the Taylor expansion of $P(Q)$, the slope is now given by $-Q^2 \langle R_G^2 \rangle / 3$, where the familiar radius of gyration R_G is substituted by an apparent radius of gyration $\langle R_G^2 \rangle^{1/2}$ (Glatter, 2018; Tomchuk *et al.*, 2014). For homogeneous spheres,

$$\langle R_G^2 \rangle = \frac{3 \langle R^8 \rangle}{5 \langle R^6 \rangle} \quad (8)$$

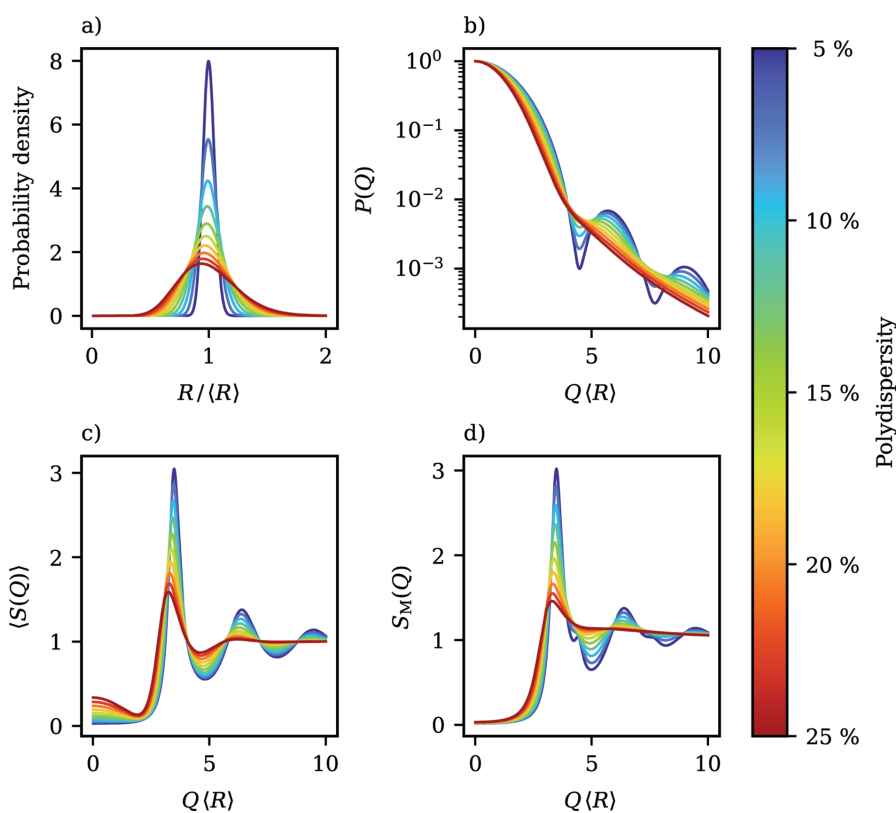


Figure 1 Comparative analysis of scattering functions for an ensemble of optically homogeneous hard spheres with varying degrees of polydispersity. (a) Probability density function illustrating the Schulz–Flory distributed radius R . (b) Form factor $P(Q)$. (c) Average structure factor $\langle S(Q) \rangle$. (d) Measurable structure factor $S_M(Q)$. All evaluated at a total volume fraction of $\phi = 0.5$, spanning polydispersities from 5 to 25%. $\langle R \rangle$ denotes the mean radius of the spheres.

is obtained, which reduces to the well known result of $R_G^2 = (3/5)R^2$ for monodisperse systems.

Similarly to $P(Q)$, both the measurable structure factor $S_M(Q)$ and the average structure factor $\langle S(Q) \rangle$ become increasingly featureless at high polydispersities, which is distinctively noticeable as the principal peak's amplitude decreases and the secondary oscillations gradually disappear. Shifting the focus to direct comparison between the two structure factors $S_M(Q)$ and $\langle S(Q) \rangle$, multiple observations are apparent. While the amplitude of the principal peak is similar for both functions, differences appear at larger wavevectors, where secondary peaks in $S_M(Q)$ appear at roughly the locations of the form-factor minima, as similarly noticed by Ginoza & Yasutomi (1999). With increasing polydispersity, these maxima evolve into broad shoulders that get smeared out eventually. As also noted by Ginoza & Yasutomi (1999), sharp secondary maxima are hard to observe experimentally because a very narrow size distribution in combination with a homogenous distribution of the scattering length density (SLD) inside the particles is required. On the other hand, shoulder-like features in experimentally determined structure factors are well documented [see, as an example, Di Cola *et al.* (2009)]. In the low- Q region, a striking observation is the significant increase of $\langle S(0) \rangle$ at elevated polydispersities in comparison with $S_M(0)$. According to the fluctuation-dissipation theorem from statistical mechanics, the isothermal compressibility κ_T is for monodisperse systems connected to the zero-wavevector limit of $S(Q)$ via $S(0) = \rho k_B T \kappa_T$, where ρ denotes the number density and $k_B T$ is the thermal energy. The extension of this concept to mixtures must however be treated with caution because, for multi-component systems, the connection between structure and thermodynamics is not simply given by the size average $\langle S(0) \rangle$. According to the Kirkwood–Buff theory of solutions, it is instead given by the relation $(\rho k_B T \kappa_T)^{-1} = \sum_{\alpha\beta} x_\alpha x_\beta S_{\alpha\beta}^{-1}(0)$, where $S_{\alpha\beta}^{-1}(Q)$ is the $\alpha\beta$ element of the inverse structure-factor matrix (Hansen & McDonald, 2013).

3.2. Linear contrast gradient

As a prototypical example for particles with inhomogeneous scattering strength, particles with a linear gradient of the SLD are investigated. This is particularly relevant for swellable particles into which the suspension medium can diffuse. This can occur with microgel particles (Karg *et al.*, 2019), for example. Under certain reaction conditions, an inhomogeneous degree of cross-linking arises, which also leads to inhomogeneous scattering properties. Particles with intrinsic material gradients are also plausible, obtained for example by continuously changing the monomer composition in a feed process during synthesis. Then, in principle, a suspension in which the contrast within a particle changes its sign can also be realized. The form of a linear gradient is assumed for the sake of simplicity in order to investigate the phenomenology of continuous contrasts as an example.

The scattering contrast as a function of the distance r from the centre can for a single particle be parametrized as

$$\rho(r) = \begin{cases} \rho_0 + (\rho_R - \rho_0) \frac{r}{R} & \text{if } 0 \leq r \leq R, \\ 0 & \text{otherwise,} \end{cases} \quad (9)$$

where R is the particle radius, ρ_0 is the contrast in the centre and ρ_R is the contrast at the interface to the surrounding medium. Accordingly, the resulting single-particle scattering amplitude is given by

$$f(Q) = 4\pi \left\{ \rho_0 \frac{\sin(QR) - QR \cos(QR)}{Q^3} + \frac{\rho_R - \rho_0}{R} \times \frac{2QR \sin(QR) - [(QR)^2 - 2] \cos(QR) - 2}{Q^4} \right\}, \quad (10)$$

which reduces to

$$f(0) = \pi R^3 \left(\frac{\rho_0}{3} + \rho_R \right) \quad (11)$$

in the forward-scattering limit. A closer look at equation (11) reveals that the forward-scattering contribution disappears if the condition $\rho_R/\rho_0 = -1/3$ is fulfilled. In particular, when the maximum accessible scattering vector is limited, as in the case of light scattering, forward scattering contributes significantly to the total scattering cross section. If the forward scattering is zero, the sample appears almost optically transparent. Refractive-index matching can be achieved for particles with a homogeneous scattering capacity if the SLD of the suspension medium is adapted to that of the particles. If the scattering capacity is inhomogeneous, index matching can only minimize the total scattering cross section, which is often achieved by making the forward scattering almost zero. In the following, the condition when the forward scattering power is minimal is referred to as the index match point.

To gain a systematic understanding of the behaviour of the measurable structure factor $S_M(Q)$ as a function of the contrast ratio ρ_R/ρ_0 , it will prove advantageous to investigate the Guinier region of the form factor. Using the contrast profile from equation (9), for a single particle with radius R ,

$$R_G^2 = \frac{2\rho_0 + 5\rho_R}{5\rho_0 + 3\rho_R} R^2 \quad (12)$$

is obtained for the effective squared radius of gyration, which depends not only on the particle's radius but also on the two contrast parameters ρ_0 and ρ_R . For polydisperse suspensions, a similar expression emerges:

$$\langle R_G^2 \rangle = \frac{2}{5} \frac{\rho_0 + 5\rho_R}{\rho_0 + 3\rho_R} \frac{\langle R^8 \rangle}{\langle R^6 \rangle}. \quad (13)$$

As such, the contrast dependence of the prefactor is not altered by polydispersity and the qualitative discussion can instead be based on monodisperse suspensions. We will thus refer to the prefactor simply as R_G^2/R^2 , even in the polydisperse case.

Inspecting equation (12), several characteristic ratios ρ_R/ρ_0 are apparent: R_G^2 becomes zero for $\rho_R/\rho_0 = -1/5$; exhibits a pole at $\rho_R/\rho_0 = -1/3$, incident with the index match point; and has an asymptotic limit of $R_G^2/R^2 = 2/3$ for $\rho_R/\rho_0 \rightarrow \pm\infty$. Here, it will be shown that the behaviour of the scattering

functions can be divided into three qualitatively distinct classes, and that form factors and measurable structure factors within each domain share unique features. The classification based on the behaviour of R_G^2 , together with form factors $P(Q)$ and measurable structure factors $S_M(Q)$ representative of each region, is visualized in Fig. 2. The regions are characterized as follows:

(I) For $\rho_R/\rho_0 > -1/5$, R_G^2 is positive and the form factors have the familiar decaying shape known from homogeneous spheres. With decreasing contrast ratio, the decay becomes increasingly gradual until $R_G^2 = 0$ is reached for $\rho_R/\rho_0 = -1/5$. Around the principal peak of $S_M(Q)$ and for lower wavevectors, changes in the contrast have a negligible influence on the measurable structure factors. However, at wavevectors beyond the principal peak's location, $S_M(Q)$ is greatly affected by contrast variation. Depending on the specific location of the first form-factor minimum, which shifts to larger wavevectors with lower contrast ratios, the shoulder-like artefact also visible in Fig. 1 moves through $S_M(Q)$ towards larger wavevectors and therein most prominently affects the shape of the first local minimum and the following secondary maximum.

(II) For the contrast ratios $-1/3 < \rho_R/\rho_0 < -1/5$, R_G^2 becomes negative, which implies an imaginary radius of gyration R_G leading to a positive initial slope of $P(Q)$. Form factors in this region therefore initially increase from $P(0) = 1$ until a global maximum is reached at $QR \simeq 4$, after which they decay. The height of the maximum increases as the contrast ratio moves towards the index match point at $\rho_R/\rho_0 = -1/3$. Curiously, the measurable structure factors in this domain are almost indistinguishable, even though the variation of R_G^2 is much more pronounced in comparison with region (I), where the span of R_G^2 is small but $S_M(Q)$ shows a much more diverse behaviour. Also, the distorting artefacts from region (I) disappear almost completely.

(III) Contrast ratios of $\rho_R/\rho_0 < -1/3$ again result in positive R_G^2 and negative initial slopes. Close to the index match point, where R_G^2 is comparatively large, $P(Q)$ exhibits an intriguing shape. At small wavevectors, a pronounced minimum occurs even in very polydisperse suspensions. Beyond the minimum, $P(Q)$ rises to a global maximum reminiscent of region (II). For contrasts in this range, an additional local maximum in $S_M(Q)$ appears at low wavevectors, caused by the presence of the first form-factor minimum. Such secondary maxima are often

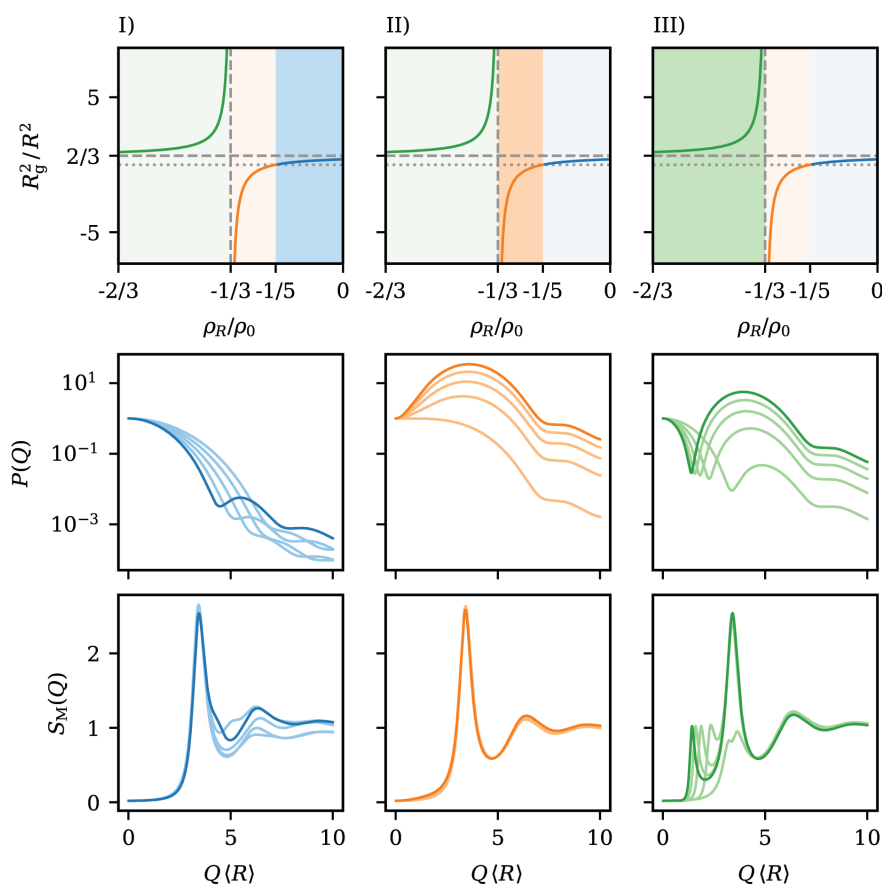


Figure 2

An illustrative breakdown of the classification of the scattering functions of spheres with a linear contrast gradient into the three regimes discussed in the main text, where each column corresponds to a unique region. In the top row, the reduced squared radius of gyration R_G^2/R^2 as a function of the contrast ratio ρ_R/ρ_0 is depicted. The location of the respective regions labelled (I), (II) or (III) is indicated by the darker shaded area. The middle and bottom rows display selected form factors $P(Q)$ and measurable structure factors $S_M(Q)$ that exemplify each region's variability in the shape observed during contrast variation. $\langle R \rangle$ indicates the mean radius of the particles. Note the shared axes of $P(Q)$ and $S_M(Q)$ between rows and columns.

discussed in the literature as an indication of self-organization on length scales beyond the distance of nearest neighbours, *i.e.* the formation of correlated clusters (Sciortino *et al.*, 2004; Liu *et al.*, 2005). The secondary maxima occurring here are exclusively caused by the scattering amplitudes and cannot be attributed to structural properties of the sample. This constitutes a valuable example of a situation where a careless inspection of experimentally determined $S_M(Q)$ can in the worst case lead to unjustified assumptions about the structure of a system. Moving further away from the index match point, the first form-factor minimum moves towards larger wavevectors and gets shallower. At the same time, the following maximum declines and, as such, the shape of $P(Q)$ morphs back into the familiar decaying shape from region (I). Simultaneously, the location of the secondary maximum in $S_M(Q)$ drifts towards higher wavevectors. Fig. 2 also displays a situation where the form-factor minimum exactly coincides with the location where the principal peak of $S_M(Q)$ would normally occur. In this case, the main peak is drastically diminished, which is again not an indicator for a less pronounced short-range order in this particular instance, but can certainly be mistaken as such.

The principal-peak height of a structure factor is an often employed structural order parameter. Scheffold & Mason (2009) noticed in their investigation of highly concentrated nanoemulsions that the peak amplitude in $S_M(Q)$ is deeply affected by polydispersity. As such, the evolution of this height during contrast variation is also of special interest. Fig. 3 compares the peak height of the average structure factor $\langle S(Q_{\max}) \rangle$ with the value of $S_M(Q_{\max})$ at the same wavevector as a function of the contrast ratio ρ_R/ρ_0 and for different degrees of polydispersity. Overall, it is clearly shown that $S_M(Q_{\max})$ is deeply affected by changes in the contrast. There exist two contrast ratios where $S_M(Q_{\max})$ and $\langle S(Q_{\max}) \rangle$ coincide. One of them is to a good approximation given by $\rho_R/\rho_0 \simeq -1/5$, the location where the apparent radius of gyration disappears and $P(Q)$ decays very slowly. The other location is at a positive contrast ratio and drifts towards higher

ρ_R/ρ_0 with increasing polydispersity. Bounded by those two ratios is a regime where $S_M(Q_{\max})$ exceeds $\langle S(Q_{\max}) \rangle$, while for all other contrast ratios, the peak height from $S_M(Q_{\max})$ underestimates the actual height. For comparatively small polydispersities around 5%, the deviation from $\langle S(Q_{\max}) \rangle$ is small and only amounts to a few per cent, as long as the contrast ratio is larger than $\rho_R/\rho_0 \simeq -1/5$. For lower ratios, $S_M(Q_{\max})$ is strongly diminished, most pronouncedly at contrast ratios of $\rho_R/\rho_0 \simeq -1$. For higher polydispersities, the deviations become even more severe, as best visualized in Fig. 3(b), where the relative deviation between $\langle S(Q_{\max}) \rangle$ and $S_M(Q_{\max})$ is depicted. Even in the immediate vicinity of $\langle S(Q_{\max}) \rangle = S_M(Q_{\max})$, already deviations of the order of 5–10% appear for the highest shown polydispersities. This demonstrates that, no matter what the actual degree of polydispersity, $S_M(Q_{\max})$ can only serve as a reliable order parameter for very specific contrast ratios.

3.3. Core–shell particles

Core–shell models are commonly employed to describe particles consisting of different layers of material, *e.g.* nanoparticles with grafted stabilizer shells (Hallett *et al.*, 2020; Diaz Maier & Wagner, 2024) or micellar structures (Szymusiak *et al.*, 2017). As core and shell naturally differ in their material properties, in principle both positive and negative contrast differences with respect to the surrounding medium can occur, similarly to particles with continuous material gradients. For Schulz–Flory-distributed core–shell particles, analytical expressions for the form factor $P(Q)$ exist in the case of a polydisperse core and a shell of constant thickness (Bartlett & Ottewill, 1992), for a polydisperse total diameter and a constant core-to-shell ratio (Wagner, 2004), and for both core radius and shell thickness independently distributed (Wagner, 2012). Moreover, an analytical solution for the problem of correlated hard-sphere core–shell systems was provided by Nayeri *et al.* (2009).

The scattering amplitude of a single core–shell particle,

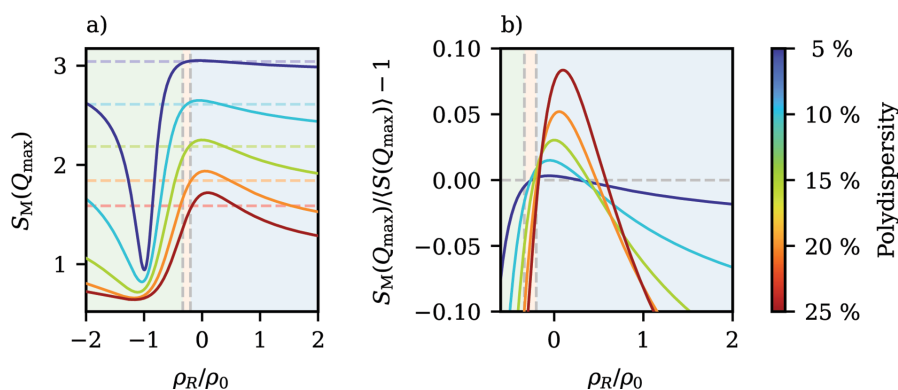


Figure 3

(a) The influence of the contrast ratio ρ_R/ρ_0 on the principal-peak value $S_M(Q_{\max})$ for spheres with a linear contrast gradient, for polydispersities in a range between 5 and 25% at a total volume fraction of $\varphi = 0.5$. The horizontal dashed lines mark, for comparison, the height of the principal peak of the average structure factor $\langle S(Q_{\max}) \rangle$. The distinction between the different introduced contrast regimes from Fig. 2 is indicated by the vertical dashed lines. (b) Relative deviation between $S_M(Q_{\max})$ and $\langle S(Q_{\max}) \rangle$ for an enlarged region.

$$f(Q) = 4\pi \left[(\rho_c - \rho_s) \frac{\sin(QR_c) - QR_c \cos(QR_c)}{Q^3} + \rho_s \frac{\sin(QR) - QR \cos(QR)}{Q^3} \right], \quad (14)$$

is the sum of the amplitudes of a sphere and a spherical shell, weighted by their respective contrasts, ρ_c and ρ_s . R_c and R are the core radius and the total radius of the particle, respectively, and we specifically consider the case where the core radius and the total radius are connected by a constant species-independent size ratio $\delta = R_c/R$.

Similar to the gradient model, the forward-scattering contribution

$$f(0) = \frac{4}{3} \pi R^3 [\delta^3 (\rho_c - \rho_s) + \rho_s] \quad (15)$$

disappears for specific contrast combinations of the ratio of contrasts $\rho_s/\rho_c = \delta^3/(\delta^3 - 1)$, which now additionally depends on the size ratio δ . For the effective radius of gyration of a polydisperse system, an expression with similar structure to equation (13) emerges:

$$\langle R_G^2 \rangle = \frac{3 \delta^5 \rho_c + (1 - \delta^5) \rho_s \langle R^8 \rangle}{5 \delta^3 \rho_c + (1 - \delta^3) \rho_s \langle R^6 \rangle}. \quad (16)$$

That, again, a prefactor containing the contrasts can be decoupled from the size average is a peculiarity of this model with constant size ratio and a key reason why this assumption was made for this investigation.

In Fig. 4, the contrast dependence of R_G^2/R^2 is visualized for different size ratios δ . As in the case of spheres with a linear gradient of the SLD, this results in hyperbola-like curves,

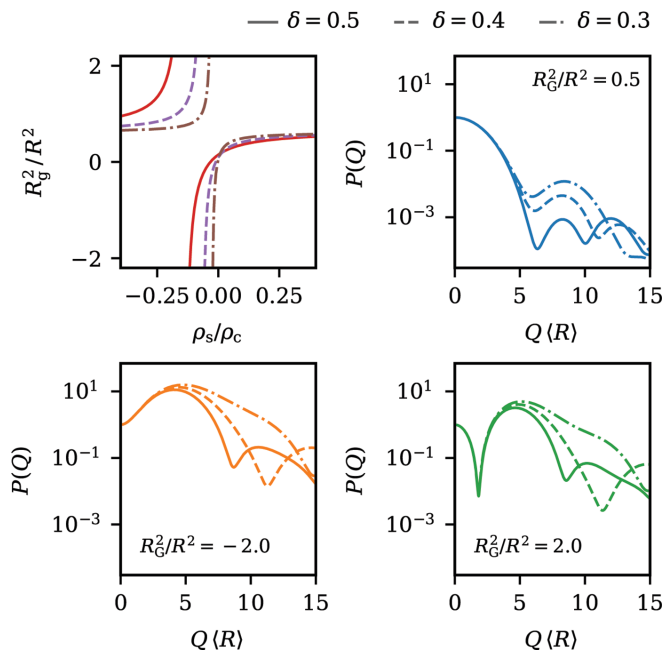


Figure 4 The influence of the contrast ratio ρ_s/ρ_c on the reduced squared radius of gyration R_G^2/R^2 for core-shell particles with different ratios δ between core radius and total radius, along with three representative sets of form factors, each sharing the same radius of gyration for different size ratios.

where the location of the pole is now influenced by δ ; an increasing ratio of core diameter to total diameter shifts the location of the pole to more negative contrast ratios (ρ_s/ρ_c). The contrast ratio where $R_G^2 = 0$ is, in comparison, only slightly altered by δ . This leads to a larger range of contrast ratios with negative R_G^2 as the shell thickness decreases.

This shows that core-shell particles exhibit qualitatively comparable optical characteristics to particles with a linear density gradient. As such, the form factors $P(Q)$ of core-shell systems can likewise be categorized into three classes based on their behaviour at low wavevectors. Example form factors for each class are also visualized in Fig. 4.

Because of these similarities, we focus the remainder of the discussion on aspects that are unique to core-shell particles, *i.e.* how measurable structure factors are influenced by

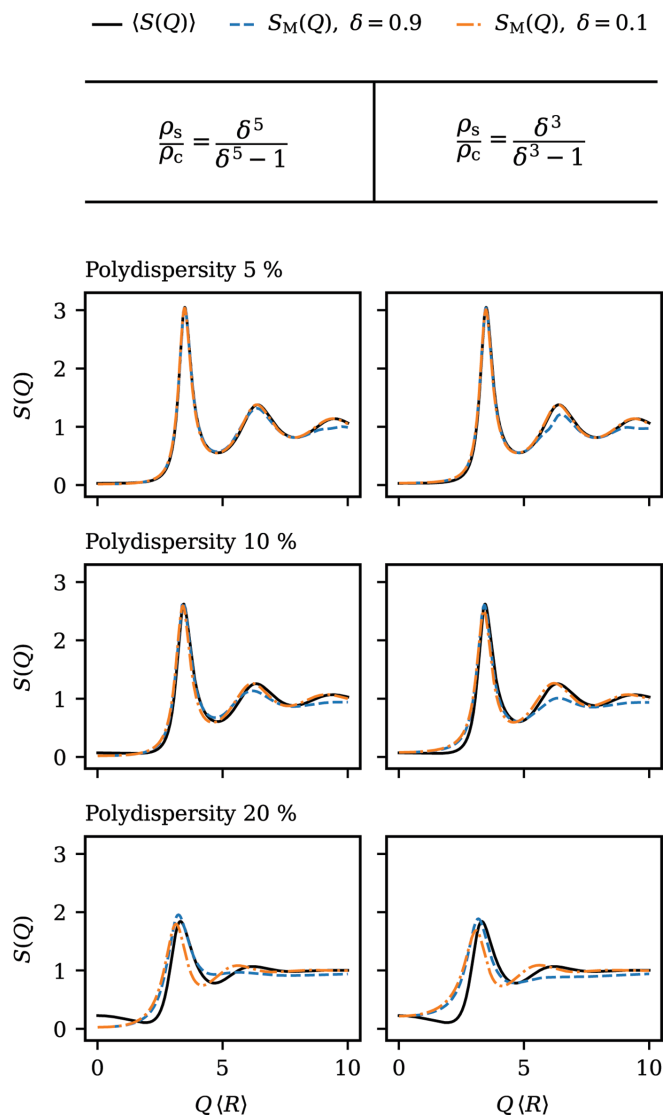


Figure 5 Comparison between measurable structure factor $S_M(Q)$ and size-averaged structure factor $\langle S(Q) \rangle$ of core-shell particles for different core-to-total ratios (δ), contrast ratios (ρ_s/ρ_c) and polydispersities as indicated in the figure. The total volume fraction for all shown structure factors is $\varphi = 0.5$.

different core-to-shell ratios. For this purpose, structure factors corresponding to two important edge cases, particles with a small core and particles with a thin shell, are compared in Fig. 5 for different degrees of polydispersity and chosen contrast ratios ρ_s/ρ_c . Core-shell models with thin shells are often encountered when characterizing particles stabilized by a grafted polymer layer, which are prototypical colloidal model particles displaying hard-sphere behaviour (Royall *et al.*, 2013). The case of hard spheres with a strongly scattering small core and a weakly scattering comparatively large shell is equally of interest. Under these conditions, essentially, the behaviour of highly charged strongly repelling particles whose interparticle distance is several times larger than their diameter is artificially mimicked. For these systems, the measurable structure factor $S_M(Q)$ should in theory to a good approximation coincide with the average structure factor $\langle S(Q) \rangle$. To reasonably compare models with different size ratios (δ), two specific contrast ratios (ρ_s/ρ_c) are depicted: the ratio $\rho_s/\rho_c = \delta^3/(\delta^3 - 1)$ at the index matching point, where forward scattering is minimized; and the ratio $\rho_s/\rho_c = \delta^5/(\delta^5 - 1)$, where $\langle R_G^2 \rangle = 0$ and $P(Q)$ shows the weakest decay. In the case of $\delta \ll 1$, both conditions basically lead to the same result: the shell is virtually hidden with $\rho_s \simeq 0$.

As can be observed in Fig. 5, for moderate polydispersities of 5–10%, the small core-to-total ratio $\delta = 0.1$ indeed yields measurable structure factors $S_M(Q)$ that are indistinguishable from $\langle S(Q) \rangle$ for both depicted contrast ratios. For particles with thin shells ($\delta = 0.9$), $S_M(Q)$ and $\langle S(Q) \rangle$ also agree well in the vicinity of the principal peak. However, differences arise around the secondary maxima, where the peak amplitudes in $S_M(Q)$ are diminished because of the interference of the scattering amplitudes. With increasing polydispersity, this deviation becomes more pronounced. Still, even for particles that are seemingly quite close to homogeneous spheres, artefacts in $S_M(Q)$ can be significantly reduced by careful contrast variation.

Looking at highly polydisperse systems, it is evident that, even for rather small cores with $\delta = 0.1$, $\langle S(Q) \rangle$ cannot be accurately represented by any $S_M(Q)$. Only the height of the principle peak is correctly estimated. This stresses again the importance of an accurate treatment of very broad size distributions, where any kind of approximation must be carefully checked for validity.

4. Conclusions

Colloidal dispersions generally exhibit a particle size distribution, which needs to be taken into account when interpreting results from scattering experiments. The measurable structure factor $S_M(Q)$ is an experimental, comparatively easily accessible measure for the interparticle structure in interacting systems. However, in polydisperse systems, $S_M(Q)$ is, beyond the structural correlations, also decisively affected by the optical properties of the individual particles. To this end, we systematically investigated the influence of different form-factor models on the shape of $S_M(Q)$ of dense dispersions with hard-sphere interactions. The characterization of

measurable structure factors was extended to two classes of spherical particles with inhomogeneous scattering capacity: first, spheres with a linear SLD profile as a general model for particles with continuous contrast gradients and, second, a core-shell system as a prototype for particles with layered structures.

For both models, we find that the structure factors can be categorized into three distinctive classes of shared qualitative features, based on the behaviour of the form factor $P(Q)$ in the Guinier region. $S_M(Q)$ can, for these optically inhomogeneous model particles, be significantly influenced by the variation of the scattering contrasts relative to the surrounding medium. Depending on the specific contrast combination, shoulder-like features emerge, maxima are diminished or split, and even secondary maxima in the low-wavevector region, reminiscent of cluster peaks, can be observed. These effects are solely due to the optical properties of the particles and are not caused by structural changes in the sample. We further showed that the height of the principal peak of $S_M(Q)$ can only be regarded as a representative order parameter in a very restricted range of contrasts, especially for broad size distributions.

These observations emphasize the need to properly address the distribution of particle size (and possibly also other characteristics) in the interpretation of static scattering experiments. Actually, for many applications, deliberately broad size distributions are a desired feature; an academically relevant example is studies of deeply supercooled glass-forming systems (Ninarello *et al.*, 2017), where crystallization needs to be suppressed and where polydispersity effects in any form certainly cannot be neglected (Zaccarelli *et al.*, 2015; Pihlajamaa *et al.*, 2023).

Beyond providing an enhanced qualitative understanding of features that can possibly be encountered when analysing experimentally extracted measurable structure factors, the numerical scheme presented in this contribution in principle provides a means to model the scattered intensity of any polydisperse hard-sphere system, provided a model for the single-particle scattering amplitude and an appropriate size distribution is available. Performing fits with such advanced models directly on experimentally observed intensities gives access to the underlying partial structure factors, enabling a characterization and possible further theoretical analysis on a genuine multi-component foundation, rather than employing effective one-component approaches. The current restriction to hard-sphere interactions is a major incentive to promote advancements in the analytical evaluation of partial structure factors for other interaction potentials, since numerically solving integral equations or employing computer simulations with reasonable statistics are currently only realistically feasible for a restricted number of components, especially in mixtures with large size disparities (Allahyarov *et al.*, 2022).

APPENDIX A

Percus–Yevick structure factors for hard-sphere mixtures

The analytical solution of the Ornstein–Zernike equation for the hard-sphere potential within the Percus–Yevick closure in

terms of the partial structure factors $S_{\alpha\beta}(Q)$, presented by Vrij (1979) and reformulated by Voigtmann (2003), is restated here. In short, an expression for the partial direct correlation functions $c_{\alpha\beta}(r)$ in real space can be found using Baxter's factorization technique (Baxter, 1970). The transformed solution in wavevector space $c_{\alpha\beta}(Q)$ can subsequently be used to obtain the partial structure factors $S_{\alpha\beta}(Q)$.

Let φ be the total volume fraction of all spheres, d_α be the diameter and x_α be the number fraction of the spheres of species α . The total number density ρ of the system is related to the volume fraction by $\varphi = (\pi/6)\rho \sum x_\alpha d_\alpha^3$. With the abbreviations

$$d_{\alpha\beta} = \frac{d_\alpha + d_\beta}{2} \quad (17)$$

and

$$\xi_x = \frac{\pi}{6} \rho \sum_\gamma x_\gamma d_\gamma^x, \quad (18)$$

the set of coefficients

$$a_\alpha = \frac{1 - \xi_3 + 3d_\alpha \xi_2}{(1 - \xi_3)^2}, \quad (19)$$

$$\tilde{a}_2 = \sum_\gamma \rho_\gamma a_\gamma^2, \quad (20)$$

$$\hat{\beta}_0 = \frac{9\xi_2^2 + 3\xi_1(1 - \xi_3)}{(1 - \xi_3)^3}, \quad (21)$$

$$A_{\alpha\beta} = \frac{d_{\alpha\beta}(1 - \xi_3) + \frac{3}{2}d_\alpha d_\beta \xi_2}{(1 - \xi_3)^2}, \quad (22)$$

$$B_{\alpha\beta} = \frac{1}{1 - \xi_3} - \hat{\beta}_0 d_\alpha d_\beta \quad (23)$$

and

$$D_{\alpha\beta} = \frac{6\xi_2 + 12d_{\alpha\beta}[\xi_1 + 3\xi_2^2/(1 - \xi_3)]}{(1 - \xi_3)^2} \quad (24)$$

can be determined. Furthermore, by introducing $S_\alpha = \sin(Qd_\alpha/2)$ and $C_\alpha = \cos(Qd_\alpha/2)$, the terms

$$\mu_A = A_{\alpha\beta} \frac{S_\alpha S_\beta - C_\alpha C_\beta}{Q^2}, \quad (25)$$

$$\mu_B = B_{\alpha\beta} \frac{C_\alpha S_\beta + C_\beta S_\alpha}{Q^3}, \quad (26)$$

$$\mu_D = D_{\alpha\beta} \frac{S_\alpha S_\beta}{Q^4} \quad (27)$$

and

$$\tilde{\mu} = \frac{4\pi}{Q^4} \tilde{a}_2 \left(\frac{C_\alpha C_\beta d_\alpha d_\beta}{4} + \frac{S_\alpha S_\beta}{Q^2} - \frac{C_\alpha S_\beta d_\alpha + C_\beta S_\alpha d_\beta}{2Q} \right) \quad (28)$$

can be calculated, which finally leads to

$$c_{\alpha\beta}(q) = -4\pi(\mu_A + \mu_B + \mu_D + \tilde{\mu}). \quad (29)$$

The partial direct correlation functions form the matrix \mathbf{C} with elements $C_{\alpha\beta} = (x_\alpha x_\beta)^{1/2} c_{\alpha\beta}$, which is related to the matrix of partial structure factors \mathbf{S} by the Ornstein–Zernike relation

$$\mathbf{S} = [\mathbf{1} - \rho \mathbf{C}]^{-1}. \quad (30)$$

The partial structure factors here are defined within the convention $\lim_{Q \rightarrow \infty} S_{\alpha\beta}(Q) = \delta_{\alpha\beta}$, where $\delta_{\alpha\beta}$ is the Kronecker delta.

Acknowledgements

Open access funding enabled and organized by Projekt DEAL.

References

- Allahyarov, E., Löwen, H. & Denton, A. R. (2022). *Phys. Chem. Chem. Phys.* **24**, 15439–15451.
- Anta, J. A. & Madden, P. A. (1999). *J. Phys. Condens. Matter*, **11**, 6099–6111.
- Ballauff, M. (2001). *Curr. Opin. Colloid Interface Sci.* **6**, 132–139.
- Balogh, J., Olsson, U. & Pedersen, J. S. (2007). *J. Phys. Chem. B*, **111**, 682–689.
- Banchio, A. J., Nägele, G. & Ferrante, A. (1998). *J. Colloid Interface Sci.* **208**, 487–499.
- Bartlett, P. & Ottewill, R. H. (1992). *J. Chem. Phys.* **96**, 3306–3318.
- Baxter, R. J. (1970). *J. Chem. Phys.* **52**, 4559–4562.
- Beenakker, C. W. J. & Mazur, P. (1983). *Physica A*, **120**, 388–410.
- Beenakker, C. W. J. & Mazur, P. (1984). *Physica A*, **126**, 349–370.
- Beurten, P. van & Vrij, A. (1981). *J. Chem. Phys.* **74**, 2744–2748.
- Blum, L. & Stell, G. (1979). *J. Chem. Phys.* **71**, 42–46.
- Blum, L. & Stell, G. (1980). *J. Chem. Phys.* **72**, 2212.
- Bohren, C. F. & Huffman, D. R. (2008). *Absorption and Scattering of Light by Small Particles*. New York: John Wiley.
- Botet, R., Kwok, S. & Cabane, B. (2020). *J. Appl. Cryst.* **53**, 1570–1582.
- D'Aguzzo, B. (1993). *Phys. Scr.* **T49A**, 84–88.
- D'Aguzzo, B. & Klein, R. (1992). *Phys. Rev. A*, **46**, 7652–7656.
- Dekker, F., Kuipers, B. W. M., González García, Á., Tuinier, R. & Philipse, A. P. (2020). *J. Colloid Interface Sci.* **571**, 267–274.
- Diaz Maier, J. & Wagner, J. (2024). *Soft Matter*, **20**, 1309–1319.
- Di Cola, E., Moussaïd, A., Sztucki, M., Narayanan, T. & Zaccarelli, E. (2009). *J. Chem. Phys.* **131**, 144903.
- Flory, P. J. (1936). *J. Am. Chem. Soc.* **58**, 1877–1885.
- Frenkel, D., Vos, R. J., de Kruif, C. G. & Vrij, A. (1986). *J. Chem. Phys.* **84**, 4625–4630.
- Genz, U. & Klein, R. (1991). *Physica A*, **171**, 26–42.
- Ginoza, M. & Yasutomi, M. (1999). *J. Phys. Soc. Jpn.* **68**, 2292–2297.
- Glatzer, O. (2018). *Scattering Methods and their Application in Colloid and Interface Science*. Amsterdam: Elsevier.
- Greene, D. G., Ferraro, D. V., Lenhoff, A. M. & Wagner, N. J. (2016). *J. Appl. Cryst.* **49**, 1734–1739.
- Griffith, W. L., Triolo, R. & Compere, A. L. (1987). *Phys. Rev. A*, **35**, 2200–2206.
- Hallett, J. E., Grillo, I. & Smith, G. N. (2020). *Langmuir*, **36**, 2071–2081.
- Hansen, J.-P., Levesque, D. & Zinn-Justin, J. (1991). *Liquids, Freezing and Glass Transition*. Amsterdam: North Holland.
- Hansen, J.-P. & McDonald, I. R. (2013). *Theory of Simple Liquids with Applications to Soft Matter*. Amsterdam: Elsevier.
- Hayter, J. B. & Penfold, J. (1981). *Mol. Phys.* **42**, 109–118.
- Janssen, L. M. C. (2018). *Front. Phys.* **6**, 97.
- Karg, M., Pich, A., Hellweg, T., Hoare, T., Lyon, L. A., Crassous, J. J., Suzuki, D., Gumerov, R. A., Schneider, S., Potemkin, I. I. & Richtering, W. (2019). *Langmuir*, **35**, 6231–6255.

- Kirkwood, J. G. & Boggs, E. M. (1942). *J. Chem. Phys.* **10**, 394–402.
- Kotlarchyk, M. & Chen, S.-H. (1983). *J. Chem. Phys.* **79**, 2461–2469.
- Krause, R., D’Aguanno, B., Mendez-Alcaraz, J. M., Nägele, G., Klein, R. & Weber, R. (1991). *J. Phys. Condens. Matter*, **3**, 4459–4475.
- Li, T., Senesi, A. J. & Lee, B. (2016). *Chem. Rev.* **116**, 11128–11180.
- Liu, Y., Chen, W.-R. & Chen, S.-H. (2005). *J. Chem. Phys.* **122**, 044507.
- Lu, P. J. & Weitz, D. A. (2013). *Annu. Rev. Condens. Matter Phys.* **4**, 217–233.
- Mason, T. G., Graves, S. M., Wilking, J. N. & Lin, M. Y. (2006). *J. Phys. Chem. B*, **110**, 22097–22102.
- Mohanty, P. S., Nöjd, S., van Gruijthuijsen, K., Crassous, J. J., Obiols-Rabasa, M., Schweins, R., Stradner, A. & Schurtenberger, P. (2017). *Sci. Rep.* **7**, 1487.
- Nayeri, M., Zackrisson, M. & Bergenholtz, J. (2009). *J. Phys. Chem. B*, **113**, 8296–8302.
- Ninarello, A., Berthier, L. & Coslovich, D. (2017). *Phys. Rev. X*, **7**, 021039.
- Olver, F. W. J., Lozier, D. W., Boisvert, R. F. & Clark, C. W. (2010). *The NIST Handbook of Mathematical Functions*. Cambridge University Press.
- Pedersen, J. S. (1994). *J. Appl. Cryst.* **27**, 595–608.
- Pedersen, J. S. (1997). *Adv. Colloid Interface Sci.* **70**, 171–210.
- Pedersen, J. S. (2001). *J. Chem. Phys.* **114**, 2839–2846.
- Peláez-Fernández, M., Moncho-Jordá, A. & Callejas-Fernández, J. (2011). *J. Chem. Phys.* **134**, 054905.
- Percus, J. K. & Yevick, G. J. (1958). *Phys. Rev.* **110**, 1–13.
- Phalakornkul, J. K., Gast, A. P., Pecora, R., Nägele, G., Ferrante, A., Mandl-Steininger, B. & Klein, R. (1996). *Phys. Rev. E*, **54**, 661–675.
- Pihlajamaa, I., Laudicina, C. C. L. & Janssen, L. M. C. (2023). *Phys. Rev. Res.* **5**, 033120.
- Pusey, P. N., Fijnaut, H. M. & Vrij, A. (1982). *J. Chem. Phys.* **77**, 4270–4281.
- Robert, A., Wagner, J., Härtl, W., Autenrieth, T. & Grübel, G. (2008). *Eur. Phys. J. E*, **25**, 77–81.
- Royall, C. P., Poon, W. C. K. & Weeks, E. R. (2013). *Soft Matter*, **9**, 17–27.
- Salgi, P. & Rajagopalan, R. (1993). *Adv. Colloid Interface Sci.* **43**, 169–288.
- Scheffold, F. & Mason, T. G. (2009). *J. Phys. Condens. Matter*, **21**, 332102.
- Schulz, G. V. (1939). *Z. Phys. Chem.* **43B**, 25–46.
- Sciortino, F., Mossa, S., Zaccarelli, E. & Tartaglia, P. (2004). *Phys. Rev. Lett.* **93**, 055701.
- Scotti, A. (2021). *Soft Matter*, **17**, 5548–5559.
- Stellbrink, J., Allgaier, J., Richter, D., Moussaid, A., Schofield, A. B., Poon, W. C. K., Pusey, P. N., Lindner, P., Dzubiella, J., Likos, C. N. & Löwen, H. (2002). *Appl. Phys. Mater. Sci. Process.* **74**, s355–s357.
- Stieger, M., Pedersen, J. S., Lindner, P. & Richtering, W. (2004). *Langmuir*, **20**, 7283–7292.
- Stieger, M., Richtering, W., Pedersen, J. S. & Lindner, P. (2004). *J. Chem. Phys.* **120**, 6197–6206.
- Szymusiak, M., Kalkowski, J., Luo, H., Donovan, A. J., Zhang, P., Liu, C., Shang, W., Irving, T., Herrera-Alonso, M. & Liu, Y. (2017). *ACS Macro Lett.*, **6**, 1005–1012.
- Tomchuk, O. V., Bulavin, L. A., Aksenov, V. L., Garamus, V. M., Ivankov, O. I., Vul’, A. Y., Dideikin, A. T. & Avdeev, M. V. (2014). *J. Appl. Cryst.* **47**, 642–653.
- Voigtman, T. (2003). *Mode Coupling Theory of the Glass Transition in Binary Mixtures*, Technische Universität München.
- Vrij, A. (1978). *J. Chem. Phys.* **69**, 1742–1747.
- Vrij, A. (1979). *J. Chem. Phys.* **71**, 3267–3270.
- Wagner, J. (2004). *J. Appl. Cryst.* **37**, 750–756.
- Wagner, J. (2012). *J. Appl. Cryst.* **45**, 513–516.
- Widom, B. (1967). *Science*, **157**, 375–382.
- Zaccarelli, E., Liddle, S. M. & Poon, W. C. K. (2015). *Soft Matter*, **11**, 324–330.
- Zackrisson, M., Stradner, A., Schurtenberger, P. & Bergenholtz, J. (2005). *Langmuir*, **21**, 10835–10845.
- Zhou, B., Gasser, U. & Fernandez-Nieves, A. (2023). *Phys. Rev. E*, **108**, 054604.

Publication IV

Rescaled mode-coupling scheme for the quantitative description of experimentally observed colloid dynamics

J. Diaz Maier and J. Wagner

Phys. Rev. E **109**, 064605 (2024)

<https://doi.org/10.1103/PhysRevE.109.064605>



Reprinted article with permission from J. Diaz Maier and J. Wagner, Phys. Rev. E **109**, 064605 (2024). Copyright (2024) by the American Physical Society.

Contribution:


I conceptualized this work together with J.W. I devised and implemented the rescaled mode-coupling scheme with help of open-source software, analyzed experimental data using the model and wrote the original draft. The manuscript was revised together with J.W.

My approximated contribution to the publication in percent: 90 %

Rescaled mode-coupling scheme for the quantitative description of experimentally observed colloid dynamics

Joel Diaz Maier  and Joachim Wagner *

Institut für Chemie, Universität Rostock, 18051 Rostock, Germany

 (Received 7 March 2024; accepted 14 May 2024; published 7 June 2024)

We describe experimentally observed collective dynamics in colloidal suspensions of model hard-sphere particles using a modified mode coupling theory (MCT). This rescaled MCT is capable of describing quantitatively the wave-vector and time-dependent diffusion in these systems. Intermediate scattering functions of liquidlike structured dispersions are determined by means of static and dynamic light-scattering experiments. The structure and short-time dynamics of the systems can be described quantitatively employing a multicomponent Percus-Yevick ansatz for the partial structure factors and an effective, one-component description of hydrodynamic interactions based on the semianalytical $\delta\gamma$ expansion. Combined with a recently proposed empirical modification of MCT in which memory functions are calculated using effective structure factors at rescaled number densities, the scheme is able to model the collective dynamics over the entire accessible time and wave-vector range and predicts the volume-fraction-dependence of long-time self-diffusion coefficients and the zero-shear viscosity quantitatively. This highlights the potential of MCT as a practical tool for the quantitative analysis and prediction of experimental observations.

DOI: [10.1103/PhysRevE.109.064605](https://doi.org/10.1103/PhysRevE.109.064605)

I. INTRODUCTION

Understanding the intricate connection between a material's macroscopic properties and the microscopic structure and dynamics of its constituents stands as a key endeavor in modern condensed matter physics. The quantitative prediction of a system's dynamics from its structural characteristics holds pivotal importance, serving as a fundamental step toward tailored material design [1].

Mode-coupling theory (MCT) is a widely recognized framework for calculating time-dependent correlation functions solely relying on static, time-independent inputs [2–6]. This theory, based on the Mori-Zwanzig projection-operator formalism [7–10], explains the trapping of strongly interacting particles within nearest-neighbor cages as a vitrification mechanism which causes structural relaxation processes to occur on two distinct timescales: The rapid β relaxation is followed by the gradual α relaxation separated by an intermediate plateau. In strongly correlated fluids, arrested states are formed which are characterized by a diverging α -relaxation time [11]. MCT's significance lies not only in predicting an ideal glass transition but also in offering nontrivial descriptions of the transition between β and α relaxation through characteristic power laws and scaling relations [12,13]. These predictions align well with empirical observations of glass-forming liquids [14–16].

A recognized limitation of MCT is the quantitative disconnect of predicted glass transition temperatures or densities for various systems in comparison to experimental or computational results [17]. MCT effectively reproduces the qualitative

behavior of numerous dynamical observables such as coherent and incoherent density correlation functions [18,19], long-time collective- and self-diffusion coefficients [20–22], or various rheological properties [23–28]. Achieving complete quantitative agreement, however, remains elusive. This discrepancy is attributed to MCT's tendency to overestimate correlations within the memory functions [29,30]. Notable counterexamples in this context are the correct quantitative prediction of the nonergodicity parameter of liquid silica [31] and of hard spheres, either in bulk [32,33] or in confinement [34].

While it is evident that at least one of the underlying approximations of MCT (for a detailed derivation of the equations, see, e.g., Ref. [6]) must be the reason for this exaggeration of correlations, precise insights have long been missing. Only very recently, Pihlajamaa *et al.* [35] were able to dissect the effects of each separate approximation along the derivation of the MCT equations. Based on their findings, they identified routes to systematically improve standard MCT, but also highlighted that many past attempts to extend MCT while upholding its foundational principles have not yielded wholly satisfactory results [36–39].

With the systematic improvement of MCT still being an ongoing effort, in the meantime, developing simplified heuristic schemes for an improved MCT is valuable from a more practical perspective. Several past studies have proposed *ad hoc* solutions to match MCT calculations to experimental or computational outcomes, such as employing effective temperatures or packing fractions [29,30], wave vector cutoffs or shifts [29], or combinations thereof [18,19,40]. Banchio *et al.* [20,21,23,24] found a rescaling of the density dependence of certain transport properties like viscosity or self-diffusion coefficient to be effective. Their approach not only accounts

*joachim.wagner@uni-rostock.de

for MCT's limitations but also for deviations induced by solvent-mediated hydrodynamic interactions (HIs), crucial in colloidal dispersion dynamics [41]. Incorporating HIs directly into the MCT equations, while feasible in certain cases, remains a challenging endeavor [42–44].

Recently, Amokrane *et al.* [45] proposed a scheme in which the MCT equations are solved employing an effective structure factor as static input. By using a structure factor evaluated at lower density, the systematic overestimation of correlations in the memory function can approximately be compensated. Contrary to just using an overall effective temperature or density, this approach explicitly takes into account a possible wave-vector-dependence of the deviations introduced by the MCT approximations, beyond simply scaling the memory function by a factor. This method has been demonstrated to yield excellent agreement between MCT calculations and simulation data for various dynamic properties in uniform and binary hard-sphere fluids [46].

In this paper, we go beyond a comparison with computer simulations and apply this scheme directly to describe the experimentally observed collective dynamics of a model hard-sphere suspension. Direct comparisons between full, wave-vector-dependent MCT calculations and experimental data of density correlation functions have been reported [16,19,21,33] but remain relatively rare compared to investigations involving simulations. Most investigations which interpret experiments in the scope of MCT either exploit universal scaling laws [33,47,48] or rely on schematic, wave-vector-independent models [49], most often for quantities indirectly coupled to density relaxation as for example obtained from quasielastic scattering [50–53], dielectric relaxation [54], or rheological [55–58] experiments.

When working with real colloidal suspensions, both the particle size distribution and the HIs mediated by the surrounding medium need to be taken into account. While the explicit incorporation of continuous size distributions has gained popularity in both theoretical and simulation works [18,39,59–62], an accurate treatment of HIs, especially in polydisperse systems, remains challenging [21,44,63,64].

We have recently demonstrated that the structure and short-time dynamics of dense, model hard-sphere suspensions consisting of silicone-stabilized poly(methyl methacrylate) (PMMA) particles can be modeled quantitatively employing a multicomponent Percus-Yevick ansatz in combination with an effective one-component treatment of HIs within the semi-analytical $\delta\gamma$ scheme [65]. Based on this approach, we show the capability of MCT as a quantitative tool to describe the full, wave-vector- and time-dependent collective dynamics of this system and also test the predictive powers of this method by calculating self-diffusion coefficients and shear viscosities explicitly based on the accurate collective dynamics.

II. RESCALED MODE-COUPLING SCHEME

Static structure factors $S(Q)$ and intermediate scattering functions $S(Q, t)$ (ISFs) of model hard-sphere suspensions consisting of sterically stabilized PMMA particles are determined by means of static and dynamic light scattering experiments for a range of volume fractions in the liquid-like region. For details on the preparation and experimental

procedures, we refer to Ref. [65], where the here-investigated suspensions were extensively characterized by means of static and dynamic light scattering. In this previous work, structure factors and hydrodynamic functions needed as input to describe long-time dynamics are quantitatively analyzed.

The optical properties of the studied particles are well-understood. Their scattering amplitude $b(Q)$ which for light scattering is essentially the Fourier transform of the refractive index distribution within a particle [66] can be described by a core-shell model which also takes into account a slightly inhomogeneous distribution of the refractive index inside the core, induced by the partial penetration of the particles by the surrounding medium. This model of the scattering properties in combination with multicomponent hard-sphere Percus-Yevick theory [67–70] is able to describe quantitatively the scattered intensity of the suspensions over the whole accessible wave vector range.

The suspensions consist of particles with a mean radius $\langle R \rangle \approx 285$ nm which is a size well-suited for light scattering experiments. It was shown that the effective hard-sphere radius of the particles somewhat decreases with increasing number density, most likely caused by changes in the chain conformation of the stabilizer chains when spheres come into close contact. This effect is accounted for during further analysis. The model fits additionally give access to the particle-size distribution, which can be well described by a Schulz-Flory distribution [71,72] with probability density function

$$c(R) = \frac{1}{\Gamma(Z+1)} \left(\frac{Z+1}{\langle R \rangle} \right)^{Z+1} R^Z \exp\left(-\frac{Z+1}{\langle R \rangle} R\right), \quad (1)$$

where the dispersity $(\langle R^2 \rangle - \langle R \rangle^2)^{1/2} / \langle R \rangle = (Z+1)^{-1/2}$ amounts to approximately 7% in our particular case. The different samples were assigned effective hard-sphere volume fractions in a range between $0.24 \leq \varphi \leq 0.52$ based on the fit results from the combined form factor and structure factor model. A volume fraction range still comparatively far from the glass transition at $\varphi \approx 0.58$ [32] constitutes a clean initial test case for the application of the proposed MCT scheme to analyze experimental results. Testing the same procedure in the deeply supercooled region close to the glass transition is the topic of ongoing investigation.

For our theoretical model, we consider a multicomponent system comprising n species of isotropically interacting, spherical particles. Following the method of D'Aguzzo and Klein [73], an n -component system representative for the continuous Schulz-Flory distribution is constructed, where already $n = 5$ yields results which are indistinguishable from finer discretizations. The system is then specified by the radii R_α and number densities ρ_α of each species of identical particles. The total number density $\rho = \sum \rho_\alpha$, the number fractions $x_\alpha = \rho_\alpha / \rho$, and the total volume fraction $\varphi = 4\pi/3 \sum \rho_\alpha R_\alpha^3$ can then be inferred from this information.

Photon correlation spectroscopy probes time-dependent fluctuations of the scattered intensity $I(Q, t)$ from which the normalized, measurable ISF $\phi_M(Q, t) = S_M(Q, t) / S_M(Q)$ is determined [74]. $\phi_M(Q, t)$ is also termed density correlation function (DCF), since it is essentially the autocorrelation function of the Fourier components of the microscopic density

[4]. We employ the descriptor “measurable” to emphasize that observables directly derived from scattering experiments always in some form involve an average over the scattering amplitudes $b(Q)$ and do not constitute simple thermodynamic averages like when accessed for example by computer simulations. The static structure given by the partial structure factors $S_{\alpha\beta}(Q)$, the composition expressed by the number fraction x_α and the scattering amplitudes $b_\alpha(Q)$ of the suspension are considered to be known quantities for our multicomponent system during further analysis. With this in mind, the time dependence of the measurable ISF

$$S_M(Q, t) = \frac{\sum_{\alpha\beta} (x_\alpha x_\beta)^{1/2} b_\alpha(Q) b_\beta(Q) S_{\alpha\beta}(Q, t)}{\sum_{\alpha} x_\alpha b_\alpha^2(Q)}, \quad (2)$$

is given by a weighted average of the elements $S_{\alpha\beta}(Q, t)$ of the matrix of partial ISFs $\mathbf{S}(Q, t)$ [75]. Note that the partial structure factors $S_{\alpha\beta}(Q)$ in our convention follow the property $S_{\alpha\beta}(Q \rightarrow \infty) = \delta_{\alpha\beta}$, with $\delta_{\alpha\beta}$ being the Kronecker symbol.

The problem of calculating $S_M(Q, t)$ is thus shifted to computing $\mathbf{S}(Q, t)$. Within MCT, the time evolution of $\mathbf{S}(Q, t)$ is, neglecting HIs, determined by [44]

$$\begin{aligned} \frac{\partial}{\partial t} \mathbf{S}(Q, t) + Q^2 \mathbf{D} \mathbf{S}^{-1}(Q) \mathbf{S}(Q, t) \\ + \mathbf{D} \int_0^t \mathbf{M}(Q, t-t') \frac{\partial}{\partial t'} \mathbf{S}(Q, t') dt' = 0, \end{aligned} \quad (3)$$

where $\mathbf{M}(Q, t)$ is the matrix of irreducible memory functions with elements

$$\begin{aligned} M_{\alpha\beta}(Q, t) = \frac{1}{16\pi^3 (\rho_\alpha \rho_\beta)^{1/2}} \sum_{\gamma\gamma'\delta\delta'} \int V_{\alpha\gamma\delta}(\mathbf{Q}, \mathbf{k}) \\ \times V_{\beta\gamma'\delta'}(\mathbf{Q}, \mathbf{k}) S_{\gamma\gamma'}(k, t) S_{\delta\delta'}(|\mathbf{Q} - \mathbf{k}|, t) d\mathbf{k}. \end{aligned} \quad (4)$$

The vertices are given by

$$\begin{aligned} V_{\alpha\gamma\delta}(\mathbf{Q}, \mathbf{k}) = \frac{\mathbf{Q} \cdot \mathbf{k}}{Q} \delta_{\alpha\delta} C_{\alpha\gamma}(k) \\ + \frac{\mathbf{Q} \cdot (\mathbf{Q} - \mathbf{k})}{Q} \delta_{\alpha\gamma} C_{\alpha\delta}(|\mathbf{Q} - \mathbf{k}|), \end{aligned} \quad (5)$$

with the dimensionless, weighted partial direct correlation functions $C_{\alpha\beta}(Q) = (\rho_\alpha \rho_\beta)^{1/2} c_{\alpha\beta}(Q) = \delta_{\alpha\beta} - (S^{-1})_{\alpha\beta}(Q)$ which are related to the partial structure factors by the multicomponent Ornstein-Zernike relation [76]. \mathbf{D} is a diagonal matrix of Stokes-Einstein diffusion coefficients of species α .

In a single-component system, hydrodynamic interactions lead to a rescaled short-time diffusion coefficient

$$D_{\text{eff}}(Q) = -\frac{1}{Q^2} \lim_{t \rightarrow 0^+} \frac{\partial}{\partial t} S(Q, t) = H(Q) \frac{D_0}{S(Q)}, \quad (6)$$

where the notation $t \rightarrow 0^+$ indicates a short time limit of structural relaxation times beyond momentum relaxation. The dimensionless scaling factor $H(Q)$ in the resulting extended de Gennes relation is the hydrodynamic function [77]. Based on ideas by Medina-Noyola [78] and Brady [79,80], recently recomplied by Riest *et al.* [81], it is an adequate approximation to assume that HIs in hard-sphere systems mostly influence the short-time behavior of any

relaxation process, which is strengthened by the observation that for many transport properties, it is sufficient to rescale theoretical outcomes of non-HI methods with HI-included short-time/high-frequency contributions to quantitatively match experimental data [20,23]. The hydrodynamic function of hard-sphere dispersions can, in principle, be calculated via computationally expensive accelerated Stokesian dynamics simulations [63,64] or the approximate $\delta\gamma$ scheme introduced by Beenakker and Mazur [82,83]. The latter is restricted to uniform dispersions but offers the advantage of a semianalytical treatment. We used the $\delta\gamma$ approximation to calculate the hydrodynamic function based on the static structure factor [84].

The collective short-time diffusion of the here-presented experimental system was thoroughly investigated in Ref. [65]. Therein, it was discussed that the measurable hydrodynamic function $H_M(Q)$, acquired from quasielastic scattering experiments, can be well described by the effective one-component formulation

$$H_M(Q) = H_s + H_d(Q) = H_s + A H_d^{\delta\gamma}(Q^*), \quad (7)$$

with $Q^* = \alpha(Q - Q_m)$, where Q_m is the wave vector at the principal peak's location. $H_M(Q)$ separates into a wave-vector-independent self part H_s and a wave-vector-dependent distinct part $H_d(Q)$, rescaled by a heuristic factor A . The function $H_d^{\delta\gamma}(Q)$ is the distinct part calculated within the one-component $\delta\gamma$ scheme [82,83], supplied with the size-average of the partial structure factors $\langle S(Q) \rangle$ as static input. The self-part H_s and the empirical parameters A and α are treated as fit parameters to match the experimental data.

To include this effective one-component formulation in the MCT scheme of a multicomponent system, the time dependence of the dynamic structure factor needs to be rescaled by a matrix $\mathbf{H}_{\text{eff}}(Q)$ with effective hydrodynamic functions

$$[\mathbf{H}_{\text{eff}}(Q)]_{\alpha\beta} = \delta_{\alpha\beta} H_s + (x_\alpha x_\beta)^{1/2} H_d(Q) \quad (8)$$

as elements. Herewith, Eq. (3) reads as

$$\begin{aligned} \frac{\partial}{\partial t} \mathbf{S}(Q, t) + Q^2 \mathbf{H}_{\text{eff}}(Q) \mathbf{D} \mathbf{S}^{-1}(Q) \mathbf{S}(Q, t) \\ + \mathbf{H}_{\text{eff}}(Q) \mathbf{D} \int_0^t \mathbf{M}(Q, t-t') \frac{\partial}{\partial t'} \mathbf{S}(Q, t') dt' = 0. \end{aligned} \quad (9)$$

This approximation neglects the influence of the scattering amplitudes $b(Q)$ on $H_M(Q)$ which, however, only causes a very small disturbance of the overall measurable relaxation rate, not noticeable within experimental uncertainty: Since size-dispersity effects were found to mostly influence the potential part of the interparticle interactions in the systems studied here [65], the differences in scattering power of differently sized species are predominantly mediated by the structure factors and not by the hydrodynamic functions. With the scheme constructed in this way, the short-time limit of the resulting measurable ISF $S_M(Q, t)$, calculated via Eq. (2), matches the experimental data from Ref. [65].

The empirical modifications proposed by Amokrane *et al.* [45] can now be incorporated into the memory function [Eq. (4)]. For this, we first define a scaled volume fraction $\varphi^* = \xi \varphi = \varphi - \Delta\varphi$ which is connected to the original volume fraction φ either via a scaling factor ξ or, equivalently,

TABLE I. Hard-sphere volume fractions φ for all suspensions investigated and optimum rescaled volume fractions φ^* used to describe experimental data. The relation between φ and φ^* can be conveniently expressed either via a scaling factor $\xi = \varphi^*/\varphi$ or a shift $\Delta\varphi = \varphi - \varphi^*$.

φ	φ^*	$\xi = (\varphi - \Delta\varphi)/\varphi$	$\Delta\varphi = (1 - \xi)\varphi$
0.52	0.447	0.86	0.073
0.50	0.420	0.84	0.080
0.48	0.393	0.82	0.087
0.47	0.381	0.81	0.089
0.44	0.349	0.79	0.091
0.38	0.292	0.77	0.088
0.33	0.250	0.76	0.080
0.24	0.173	0.72	0.067

via a shift $\Delta\varphi$ and later needs to be determined by matching the MCT outcome to the experimental data. Now, a set of effective partial structure factors $S_{\alpha\beta}^*(Q)$ is calculated with φ^* instead of φ as an input parameter and, subsequently, every occurrence of the weighted partial direct correlation functions $C_{\alpha\beta}(Q)$ in the vertex [Eq. (5)] is replaced by $C_{\alpha\beta}^*(Q) = \delta_{\alpha\beta} - (S^{-1})_{\alpha\beta}^*(Q)$.

III. COLLECTIVE DYNAMICS

The MCT equations for the presented scheme are numerically solved employing common methods [30,85,86]. From the resulting partial ISFs $S_{\alpha\beta}(Q, t)$, the measurable ISF $S_M(Q, t)$ is then calculated according to Eq. (2). The optimum scaled volume fraction φ^* used in the model was evaluated by minimizing deviations between experimental data and theory in the whole accessible time and wave-vector range. Optimum rescaled volume fractions φ^* and actual volume fractions φ are compared in Table I. Interestingly, the deviation $\Delta\varphi$ from the rescaled volume fraction to the actual volume fraction traverses a maximum at $\varphi \approx 0.44$, where the rescaling factors α and A for the hydrodynamic function [Eq. (7)] become approximately one: At a volume fraction where the $\delta\gamma$ approximation is practically correct, the largest deviations of MCT are observed.

Figure 1(a) shows a comparison of the time dependence of experimentally obtained measurable DCFs $\phi_M(Q_m, t)$, evaluated at the wave vector Q_m corresponding to the principal structure-factor peak, and theoretical results according to the rescaled mode-coupling scheme. In conjunction, in Fig. 2, the wave-vector dependence of the same correlation functions is displayed for several delay times. For all investigated volume fractions, the experimental relaxation functions can be described quantitatively by the theory over almost the whole accessible time and wave-vector range. As expected from liquidlike systems relatively far from the glass transition, the relaxation is profoundly stretched for the larger volume fractions, but a separation into two different relaxation regimes is not yet observable. The rescaled theory captures this stretched decay accurately. While some minor deviations are noticeable, these can be well explained by statistical fluctuations of the experimental values, most apparent at long delay times where $\phi_M(Q_m, t) \lesssim 0.2$. The theoretical prediction itself is techni-

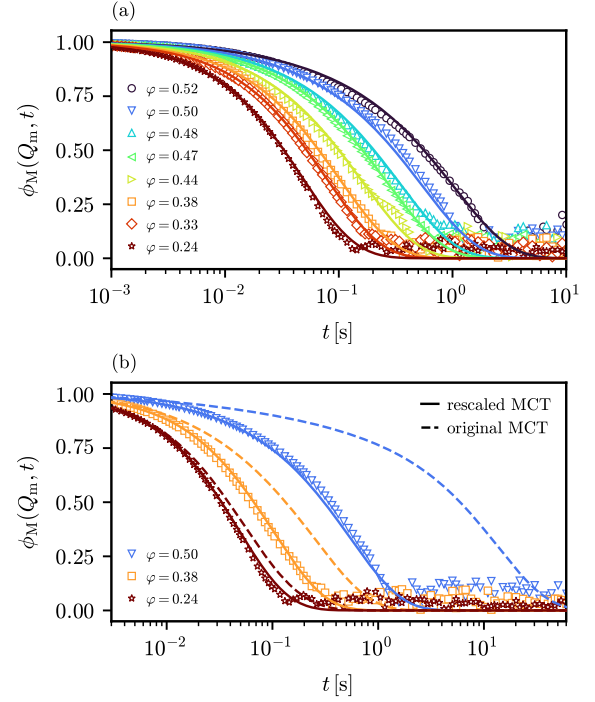


FIG. 1. (a) Time dependence of the measurable density correlation function $\phi_M(Q_m, t)$ at the principal structure factor peak's location Q_m for volume fractions as indicated in the legend. The solid lines are the results of the rescaled mode-coupling scheme described in the text. (b) Comparison between $\phi_M(Q_m, t)$ calculated with rescaled volume fractions and results from the original MCT with an unmodified memory function.

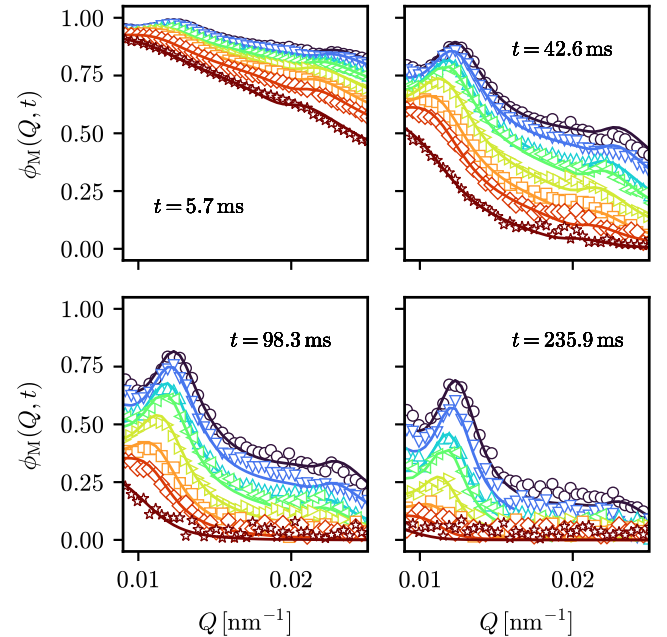


FIG. 2. Wave-vector dependence of the measurable density correlation function $\phi_M(Q, t)$ for chosen delay time as indicated. The symbols are the same as in Fig. 1, with the solid lines being results of the rescaled mode-coupling scheme.

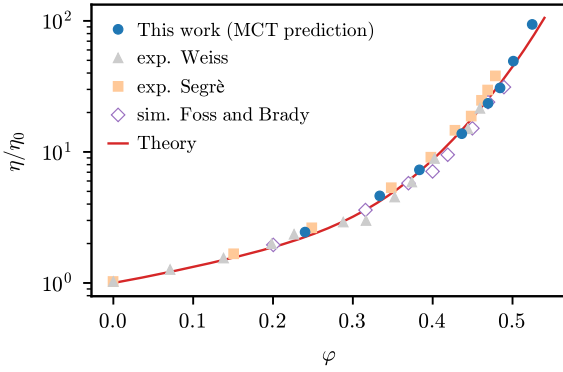


FIG. 3. Reduced zero-shear viscosity η/η_0 , as predicted by the rescaled mode-coupling scheme, compared to experimental data by Segrè *et al.* [87] and Weiss *et al.* [88] and results from Stokesian dynamics simulations by Foss and Brady [89]. Additionally, a theoretical prediction based on a modified scaling expression proposed by Brady (Eq. (56) in Ref. [81]) is given by the solid line.

cally also subjected to uncertainties from the input parameters propagated through the scheme, however, the precise estimation of an uncertainty range is difficult due to the complexity of the model.

Figure 1(b) additionally displays for chosen densities a comparison between the predictions of the MCT scheme with and without scaling factors for the volume fraction. It is evident, especially at larger volume fractions, that standard MCT significantly overestimates the structural relaxation time. Clearly, this emphasizes the considerable improvements enabled by this comparatively simple rescaling approach, especially considering that the experimental values are matched not only for a conveniently chosen wave vector, but for all wave vectors simultaneously.

IV. PREDICTION OF TRANSPORT PROPERTIES

Beyond the successful quantitative description of the experimentally observed collective relaxation, we test if related transport properties can be predicted correctly based on the parameterized scheme without further adjustable parameters.

The shear viscosity η in the limit of small shear rates can be directly calculated within MCT from the partial ISFs and is given by [43]

$$\begin{aligned} \frac{\eta - \eta_\infty}{\eta_0} &= \frac{k_B T}{60\pi^2} \int_0^\infty \int_0^\infty Q^4 \text{Tr} \left[\left(\frac{d\mathbf{C}(Q)}{dQ} \cdot \mathbf{S}(Q, t) \right)^2 \right] dQ dt, \end{aligned} \quad (10)$$

with η_0 being the viscosity of the surrounding medium and η_∞ being the hydrodynamic high-frequency contribution. We use the accurate parametrization given by Eq. (36) in Ref. [81] to calculate η_∞ . The resulting predictions for η/η_0 in dependence on the volume fraction ϕ are displayed in Fig. 3, where they are compared to independent results of experimental [87,88] and simulation studies [89] from the literature along with a theoretical prediction based on a generalized Stokes-

Einstein relation [81]. Strikingly, the values predicted from the collective dynamics fit nicely among these results, which clearly show that if a mode-coupling scheme can correctly describe the collective density relaxation of a realistic suspension, the viscosity calculated via Eq. (10) is consistently also quantitatively correct.

The self-dynamics of the system are also accessible within MCT. This, however, requires the self-consistent solution of a supplementary set of equations. For the self-ISFs $S_\alpha^s(Q, t)$, these are given by [41]

$$\begin{aligned} \frac{\partial}{\partial t} S_\alpha^s(Q, t) + Q^2 H_s D_\alpha^0 S_\alpha^s(Q, t) \\ + H_s D_\alpha^0 \int_0^t M_\alpha^s(Q, t-t') \frac{\partial}{\partial t'} S_\alpha^s(Q, t') dt' = 0, \end{aligned} \quad (11)$$

with the memory kernels

$$\begin{aligned} M_\alpha^s(Q, t-t') = \frac{1}{8\pi^3 \rho_\alpha} \int \left(\frac{\mathbf{Q} \cdot \mathbf{k}}{Q} \right)^2 S_\alpha^s(|\mathbf{Q}-\mathbf{k}|, t) \\ \times \sum_{\delta\delta'} C_{\alpha\delta}(k) C_{\alpha\delta'}(k) S_{\delta\delta'}(k, t) d\mathbf{k}. \end{aligned} \quad (12)$$

The scheme for the self-dynamics relies on the short-time self-diffusion coefficients D_α^s , which in the same spirit of an effective one-component treatment of the HIs are constructed to be $D_\alpha^s = H_s D_\alpha^0$ where H_s is the self-part of the one-component hydrodynamic function [Eq. (7)]. The rescaling procedure from Amokrane *et al.* [45] is again incorporated by calculating the density-weighted partial direct correlation functions $C_{\alpha\beta}(Q)$ with the scaled volume fraction ϕ^* , exactly using the same values as for the collective dynamics. From the self-ISFs, we compute long-time self-diffusion coefficients $D_{L,\alpha}^s$ from the long-time, low-wave-vector limit of Eq. (11), as described, e.g., in Ref. [30]. Figure 4(a) shows the MCT prediction for the average long-time self-diffusion coefficient $\langle D_L^s \rangle_\alpha$ along with outcomes from independent computer simulations [90] and experiments on a similar model system [91,92]. This is in accordance with a theoretical prediction based on the HI rescaling proposed in Medina-Noyola [78]. Again, the values calculated via the mode-coupling scheme are in excellent agreement, both with literature data and theory which demonstrates the applicability of this rescaled MCT ansatz to consistently also describe tagged-particle motion, despite an additional layer of approximations within the theory. Furthermore, this especially emphasizes the intricate link between self-dynamics and cooperative effects.

On a final note, we want to point out a convenient byproduct of the employed scheme: Since the procedure is based on a multicomponent approach, automatically, species-resolved analyses become possible. In Fig. 4(b), this is demonstrated by revealing what is essentially the distribution of long-time self-diffusion coefficients in the disperse suspension. Particularly intriguing is the evolution of the width of this distribution with increasing particle concentration. Compared to the width at $\phi = 0$, which is essentially just a representation of the particle size distribution [Fig. 4(c)] expressed via the Stokes-Einstein relation, the distribution significantly broadens with increasing ϕ , up to a threshold value of $\phi \approx 0.45$, beyond which the relative diffusivities again converge towards the average

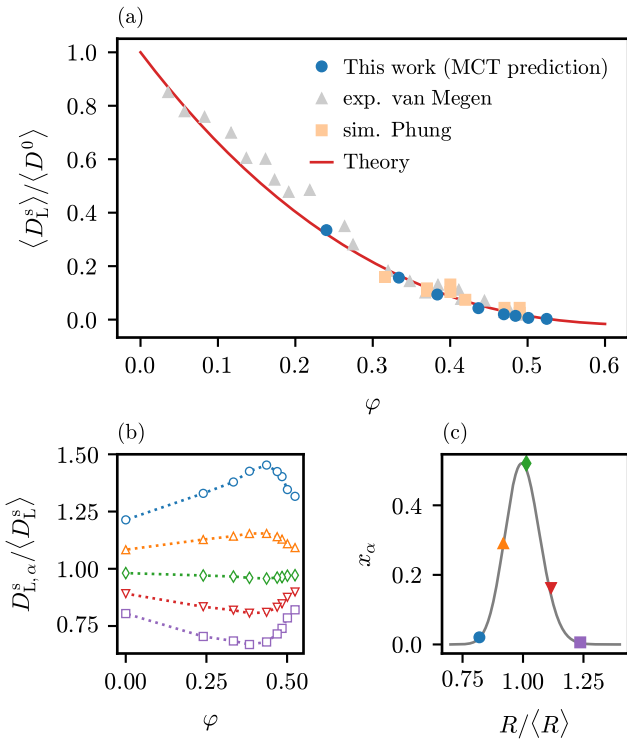


FIG. 4. (a) Average long-time self-diffusion coefficient $\langle D_L^s \rangle$ relative to the average Stokes-Einstein diffusion coefficient $\langle D^0 \rangle$ as predicted by the rescaled mode-coupling scheme compared to direct measurements by van Megen and Underwood [92] on a similar model system and Stokesian dynamics simulations by Phung [90]. Additionally, a theoretical prediction based on parameterized simulation data in conjunction with the factorization approximation by Medina-Noyola [78] (Eq. (45) in Ref. [81]) is given by the solid line. (b) Single-species long-time self-diffusion coefficient $D_{L,\alpha}^s$ relative to the average $\langle D_L^s \rangle$ in dependence on the volume fraction ϕ . The dashed lines are a guide to the eye. (c) Distribution of particle radii in relation to the mean, with each symbol in correspondence to (b). Additionally, the continuous Schulz-Flory distribution, which is approximated by the n -component mixture, is represented by the solid line.

value. The same convergence towards a shared timescale at high volume fractions was similarly observed recently in a quasi-two-dimensional, binary hard sphere fluid [93]. However, the exact mechanisms, especially the initial broadening of the distribution, are still not entirely clear.

V. CONCLUSIONS

In this paper, we described quantitatively experimental collective density correlation functions $\phi_M(Q, t)$ of liquidlike

ordered model hard-sphere suspensions with a multicomponent mode-coupling scheme based on the rescaled structure factor method proposed by Amokrane *et al.* [45]. Hydrodynamic interactions were approximately incorporated using Medina-Noyola's [78] short-time factorization. Based on these results, long-time self-diffusion coefficients and zero-shear viscosities were derived from the collective dynamics without further adjustable parameters. Both quantities excellently agree with independent experiments and established theoretical predictions from the literature. Altogether, this demonstrates mode-coupling theory's capability as a tool for the consistent and quantitatively correct characterization of experimentally observed collective dynamics and transport properties in dense colloidal dispersions.

As an obvious downside, the first-principles character of MCT is lost within our approach due to the introduction of an empirical parameter without real physical significance. However, as already noted by Amokrane and Germain [46], such a treatment is, beyond just being a practical solution for a complicated problem, certainly meaningful. Results such as these emphasize the immense potential of MCT if, eventually, systematic advancements of the theory are indeed realized. A promising roadmap for this challenge was just recently laid out by Pihlajamaa *et al.* [35].

Additional investigations are required to further test the limitations of the here-employed scheme. We restricted ourselves to the analysis of liquidlike or only mildly supercooled suspensions with volume fractions $\phi \leq 0.52$. A natural extension is thus the investigation of the more deeply supercooled and also the glasslike regime which probably requires the use of samples with broader size distributions to prevent an eventual crystallization even over long observation times [60]. If the here-employed multicomponent treatment is generally applicable to such very disperse systems is in itself a question of interest. Equally important is testing the predictions of such schemes for a more extensive set of dynamical observables, e.g., by probing the full, wave-vector-dependent self-dynamics or frequency-dependent viscoelastic properties.

Undoubtedly, also desired is the application to model systems beyond hard spheres in bulk, with just a few examples being particles with long-range repulsive [21] or competing interactions [94], self-propelled particles [95,96], or systems in confinement [34]. From a technical perspective, this involves additional efforts to further develop methods for the fast evaluation of partial structure factors in multicomponent systems, for example, via advanced integral-equation schemes [97], and of partial hydrodynamic functions, where the only reasonably applicable analytic multicomponent framework is based on Rotne-Prager-Yamakawa hydrodynamics, only suitable for dilute systems [98].

The authors have no conflicts to disclose.

- [1] J. van der Gucht, *Front. Phys.* **6**, 87 (2018).
- [2] U. Bengtzelius, W. Gotze, and A. Sjolander, *J. Phys. C: Solid State Phys.* **17**, 5915 (1984).
- [3] G. Szamel and H. Löwen, *Phys. Rev. A* **44**, 8215 (1991).
- [4] L. M. C. Janssen, *Front. Phys.* **6**, 97 (2018).

- [5] G. Szamel, *Prog. Theor. Exp. Phys.* **2013**, 012J01 (2013).
- [6] D. R. Reichman and P. Charbonneau, *J. Stat. Mech.* (2005) P05013.
- [7] R. Zwanzig, *J. Chem. Phys.* **33**, 1338 (1960).
- [8] R. Zwanzig, *Phys. Rev.* **124**, 983 (1961).

- [9] H. Mori, *Prog. Theor. Phys.* **33**, 423 (1965).
- [10] H. Mori, *Prog. Theor. Phys.* **34**, 399 (1965).
- [11] W. Götze, *Z. Phys. B* **56**, 139 (1984).
- [12] W. Götze, *Z. Phys. B* **60**, 195 (1985).
- [13] W. Gotze, *J. Phys.: Condens. Matter* **2**, 8485 (1990).
- [14] W. Kob and H. C. Andersen, *Phys. Rev. E* **52**, 4134 (1995).
- [15] W. Kob and H. C. Andersen, *Phys. Rev. E* **51**, 4626 (1995).
- [16] W. Götze, *J. Phys.: Condens. Matter* **11**, A1 (1999).
- [17] S. P. Das, *Rev. Mod. Phys.* **76**, 785 (2004).
- [18] F. Weysser, A. M. Puertas, M. Fuchs, and Th. Voigtmann, *Phys. Rev. E* **82**, 011504 (2010).
- [19] Th. Voigtmann, *Phys. Rev. E* **68**, 051401 (2003).
- [20] A. J. Banchio, G. Nägele, and J. Bergenholtz, *J. Chem. Phys.* **113**, 3381 (2000).
- [21] A. J. Banchio, M. Heinen, P. Holmqvist, and G. Nägele, *J. Chem. Phys.* **148**, 134902 (2018).
- [22] G. Nägele, A. J. Banchio, M. Kollmann, and R. Pesché, *Mol. Phys.* **100**, 2921 (2002).
- [23] A. J. Banchio, G. Nägele, and J. Bergenholtz, *J. Chem. Phys.* **111**, 8721 (1999).
- [24] A. J. Banchio, J. Bergenholtz, and G. Nägele, *Phys. Rev. Lett.* **82**, 1792 (1999).
- [25] M. Priya and Th. Voigtmann, *J. Rheol.* **58**, 1163 (2014).
- [26] E. Di Cola, A. Moussaïd, M. Sztucki, T. Narayanan, and E. Zaccarelli, *J. Chem. Phys.* **131**, 144903 (2009).
- [27] T. Voigtmann, M. Siebenbürger, C. P. Amann, S. U. Egelhaaf, S. Fritschi, M. Krüger, M. Laurati, K. J. Mutch, and K. H. Samwer, *Colloid Polym. Sci.* **298**, 681 (2020).
- [28] O. Henrich, F. Weysser, M. E. Cates, and M. Fuchs, *Philos. Trans. R. Soc. A* **367**, 5033 (2009).
- [29] M. Nauroth and W. Kob, *Phys. Rev. E* **55**, 657 (1997).
- [30] E. Flenner and G. Szamel, *Phys. Rev. E* **72**, 031508 (2005).
- [31] F. Sciortino and W. Kob, *Phys. Rev. Lett.* **86**, 648 (2001).
- [32] W. van Meegen, S. M. Underwood, and P. N. Pusey, *Phys. Rev. Lett.* **67**, 1586 (1991).
- [33] W. van Meegen and S. M. Underwood, *Phys. Rev. Lett.* **70**, 2766 (1993).
- [34] G. Jung and T. Franosch, *Phys. Rev. E* **107**, 054101 (2023).
- [35] I. Pihlajamaa, V. E. Debets, C. C. L. Laudicina, and L. M. C. Janssen, *SciPost Phys.* **15**, 217 (2023).
- [36] P. Mayer, K. Miyazaki, and D. R. Reichman, *Phys. Rev. Lett.* **97**, 095702 (2006).
- [37] L. M. C. Janssen and D. R. Reichman, *Phys. Rev. Lett.* **115**, 205701 (2015).
- [38] G. Szamel, *Phys. Rev. Lett.* **90**, 228301 (2003).
- [39] C. C. L. Laudicina, C. Luo, K. Miyazaki, and L. M. C. Janssen, *Phys. Rev. E* **106**, 064136 (2022).
- [40] Th. Voigtmann, A. M. Puertas, and M. Fuchs, *Phys. Rev. E* **70**, 061506 (2004).
- [41] G. Nägele and P. Baur, *Physica A* **245**, 297 (1997).
- [42] G. Nägele and J. K. G. Dhont, *J. Chem. Phys.* **108**, 9566 (1998).
- [43] G. Nägele and J. Bergenholtz, *J. Chem. Phys.* **108**, 9893 (1998).
- [44] G. Nägele, J. Bergenholtz, and J. K. G. Dhont, *J. Chem. Phys.* **110**, 7037 (1999).
- [45] S. Amokrane, F. Tchanganwa Nya, and J. M. Ndjaka, *Eur. Phys. J. E* **40**, 17 (2017).
- [46] S. Amokrane and Ph. Germain, *Phys. Rev. E* **99**, 052120 (2019).
- [47] Ch. Beck, W. Härtl, and R. Hempelmann, *J. Chem. Phys.* **111**, 8209 (1999).
- [48] T. G. Mason and D. A. Weitz, *Phys. Rev. Lett.* **75**, 2770 (1995).
- [49] V. Krakoviack and C. Alba-Simionesco, *J. Chem. Phys.* **117**, 2161 (2002).
- [50] T. Franosch, W. Götze, M. R. Mayr, and A. P. Singh, *Phys. Rev. E* **55**, 3183 (1997).
- [51] A. P. Singh, G. Li, W. Götze, M. Fuchs, T. Franosch, and H. Z. Cummins, *J. Non-Cryst. Solids* **235-237**, 66 (1998).
- [52] B. Rufflé, S. Beaufils, B. Toudic, C. Ecolivet, A. Le Sauze, and R. Marchand, *J. Non-Cryst. Solids* **235-237**, 244 (1998).
- [53] B. Rufflé, C. Ecolivet, and B. Toudic, *Europhys. Lett.* **45**, 591 (1999).
- [54] M. Domschke, M. Marsilius, T. Blochowicz, and T. Voigtmann, *Phys. Rev. E* **84**, 031506 (2011).
- [55] J. J. Crassous, M. Siebenbürger, M. Ballauff, M. Drechsler, D. Hajnal, O. Henrich, and M. Fuchs, *J. Chem. Phys.* **128**, 204902 (2008).
- [56] M. Siebenbürger, M. Fuchs, H. Winter, and M. Ballauff, *J. Rheol.* **53**, 707 (2009).
- [57] J. M. Brader, M. Siebenbürger, M. Ballauff, K. Reinheimer, M. Wilhelm, S. J. Frey, F. Weysser, and M. Fuchs, *Phys. Rev. E* **82**, 061401 (2010).
- [58] J. Diaz Maier and J. Wagner, *J. Chem. Phys.* **157**, 114901 (2022).
- [59] E. Zaccarelli, S. M. Liddle, and W. C. K. Poon, *Soft Matter* **11**, 324 (2015).
- [60] A. Ninarello, L. Berthier, and D. Coslovich, *Phys. Rev. X* **7**, 021039 (2017).
- [61] I. Pihlajamaa, C. C. L. Laudicina, and L. M. C. Janssen, *Phys. Rev. Res.* **5**, 033120 (2023).
- [62] C. C. L. Laudicina, I. Pihlajamaa, and L. M. C. Janssen, *Phys. Rev. Res.* **5**, 033121 (2023).
- [63] A. Sierou and J. F. Brady, *J. Fluid Mech.* **448**, 115 (2001).
- [64] A. J. Banchio and J. F. Brady, *J. Chem. Phys.* **118**, 10323 (2003).
- [65] J. Diaz Maier and J. Wagner, *Soft Matter* **20**, 1309 (2024).
- [66] O. Glatter, *Scattering Methods and Their Application in Colloid and Interface Science*, 1st ed. (Elsevier, Amsterdam, 2018).
- [67] A. Vrij, *J. Chem. Phys.* **69**, 1742 (1978).
- [68] A. Vrij, *J. Chem. Phys.* **71**, 3267 (1979).
- [69] L. Blum and G. Stell, *J. Chem. Phys.* **71**, 42 (1979).
- [70] L. Blum and G. Stell, *J. Chem. Phys.* **72**, 2212 (1980).
- [71] G. V. Schulz, *Z. Phys. Chem.* **43B**, 25 (1939).
- [72] P. J. Flory, *J. Am. Chem. Soc.* **58**, 1877 (1936).
- [73] B. D'Aguanno and R. Klein, *Phys. Rev. A* **46**, 7652 (1992).
- [74] B. J. Berne and R. Pecora, *Dynamic Light Scattering: With Applications to Chemistry, Biology and Physics* (Dover Publications, 1976).
- [75] J.-P. Hansen, D. Levesque, and J. Zinn-Justin, *Liquids, Freezing and Glass Transition* (North Holland, Amsterdam, 1991).
- [76] J.-P. Hansen and I. R. McDonald (eds.), *Theory of Simple Liquids* (Academic Press, Oxford, 2013).
- [77] We use here a slightly different notation with $H(Q)$ as a dimensionless scaling factor, whereas in Ref. [44], $H'(Q) = H(Q)D$ with the dimension of a diffusion coefficient is used.
- [78] M. Medina-Noyola, *Phys. Rev. Lett.* **60**, 2705 (1988).
- [79] J. F. Brady, *J. Chem. Phys.* **99**, 567 (1993).
- [80] J. F. Brady, *J. Fluid Mech.* **272**, 109 (1994).
- [81] J. Riest, T. Eckert, W. Richtering, and G. Nägele, *Soft Matter* **11**, 2821 (2015).
- [82] C. W. J. Beenakker and P. Mazur, *Physica A* **120**, 388 (1983).
- [83] C. W. J. Beenakker and P. Mazur, *Physica A* **126**, 349 (1984).

- [84] U. Genz and R. Klein, *Physica A* **171**, 26 (1991).
- [85] M. Fuchs, W. Götze, I. Hofacker, and A. Latz, *J. Phys.: Condens. Matter* **3**, 5047 (1991).
- [86] I. Pihlajamaa, C. C. L. Laudicina, T. Voigtmann, and L. M. C. Janssen, *J. Open Source Softw.* **8**, 5737 (2023).
- [87] P. N. Segrè, S. P. Meeker, P. N. Pusey, and W. C. K. Poon, *Phys. Rev. Lett.* **75**, 958 (1995).
- [88] A. Weiss, N. Dingenouts, M. Ballauff, H. Senff, and W. Richtering, *Langmuir* **14**, 5083 (1998).
- [89] D. R. Foss and J. F. Brady, *J. Fluid Mech.* **407**, 167 (2000).
- [90] T. N. Phung, Ph.D. thesis, California Institute of Technology, 1993.
- [91] W. van Meegen, S. M. Underwood, and I. Snook, *J. Chem. Phys.* **85**, 4065 (1986).
- [92] W. van Meegen and S. M. Underwood, *J. Chem. Phys.* **91**, 552 (1989).
- [93] A. L. Thorneywork, D. G. A. L. Aarts, J. Horbach, and R. P. A. Dullens, *Phys. Rev. E* **95**, 012614 (2017).
- [94] C. L. Klix, C. P. Royall, and H. Tanaka, *Phys. Rev. Lett.* **104**, 165702 (2010).
- [95] J. Reichert, L. F. Granz, and T. Voigtmann, *Eur. Phys. J. E* **44**, 27 (2021).
- [96] V. E. Debets and L. M. C. Janssen, *J. Chem. Phys.* **159**, 014502 (2023).
- [97] Y. V. Kalyuzhnyi, I. Nezbeda, and P. T. Cummings, *Soft Matter* **16**, 3456 (2020).
- [98] M. G. McPhie and G. Nägele, *J. Chem. Phys.* **127**, 034906 (2007).